ISSN 1403-1701 Kärnkraftsäkerhet 5
ISBN 91-7170-441-8
TRITA EKS.Avhandling
ISRN KTH/NPS/Ignalina-9909-SE

# Development, Validation and Application of an RBMK Reactor Physics Capability at KTH

## Engineering Licentiate Thesis

by

**Antanas Romas**

Stockholm
1999

Institutionen for Energiteknik
Avdelning för Kärnkraftsäkerhet
Kungliga Tekniska Högskolan
Stockholm

Department of Energy Technology
Div. of Nuclear Power Safety
The Royal Institute of Technology
Stockholm, Sweden

ISSN 1403-1701 Kärnkraftsäkerhet 5
ISBN 91-7170-441-8
TRITA EKS.Avhandling
ISRN KTH/NPS/Ignalina-9909-SE

# Development, Validation and Application of an RBMK Reactor Physics Capability at KTH

## Engineering Licentiate Thesis

by

**Antanas Romas**

Stockholm
1999

Institutionen for Energiteknik
Avdelning för Kärnkraftsäkerhet
Kungliga Tekniska Högskolan
Stockholm

Department of Energy Technology
Div. of Nuclear Power Safety
The Royal Institute of Technology
Stockholm, Sweden

# Abstract

## Development, Validation and Application of an RBMK Reactor Physics Capability at KTH

**Antanas Romas**

Department of Energy Technology
Division of nuclear Power Safety
The Royal Institute of Technology
S-100 44 Stockholm, Sweden

An RBMK-type reactor has become the object of intense safety analysis studies since the Chernobyl accident. This thesis is aimed at developing, validating and applying a reactor physics capability for analysis of the core transients in a RBMK.

The reactor physics capability is based on the ARROTTA three-dimensional neutron dynamics with thermal hydraulic feedback code [5], developed by Sol Levy Associates under the auspices of the Electric Power Research Institute (EPRI). The ARROTTA code, originally developed for light water reactor (LWR) core transient analysis, was modified and adapted for the RBMK core analysis.

The modifications and adaptations of the ARROTTA code include a) developing and modification processing codes for the construction of the ARROTTA cross section library from CASMO and WIMS-$D_4$ code calculations b) developing processing codes, which would access the Ignalina plant core configuration and database and convert that to the required input file for the ARROTTA code and c) modifying the code to represent the different control rods in an RBMK plant. Full core representation (individual representation of all fuel, control rod and reflector assemblies) and analysis capability was developed. The ARROTTA code original cross-sections model and cross-section data processing system were adapted for Ignalina Nuclear Power Plant (INPP) reactor's analysis.

The ARROTTA code was validated against data obtained in RBMK-type critical facility experiments. Comparisons were made for the effective multiplication factor, neutron flux distribution and control rod worth. Several critical experiments were analyzed and it was found that the ARROTTA results were in excellent agreement with the measurements. For instance, average neutron flux discrepancy at initial core conditions is only 1.0-6.0%.

The INPP is changing over to the Erbium poisoned higher enrichment fuel. Study of the safety parameters for this fuel was performed with the CASMO-4 lattice code. Three fuel types having different enrichment and poison isotopes

concentrations were considered. This study showed that higher fuel enrichment and higher erbium concentration imparts favorable safety characteristics. A negative void reactivity coefficient was observed up to 7.0 MWd/kg fuel burnup. Higher enrichment and erbium concentration (than currently employed) could increase the range of fuel burnup for which the void coefficient remains negative. It is found that positive void reactivity result from the loss of physical absorber (water) and the hardening of the neutron spectrum.

The ARROTTA code was applied to analysis of core transients for INPP. A hypothetical fuel drop event with disabled local control and protection system in the INPP was analyzed. A mechanical-hydraulic model was developed to calculate fuel bundle velocity. The mechanical-hydraulic calculations indicated that fuel assembly is fully inserted in the active core in 4.2sec with the velocity varying between 1.95 and 1.57m/sec. It was found that the fuel temperature safety margins are not exceeded.

We believe that the capability developed, after further validation in particular against plant data from INPP and other RBMK plants, could be routinely applied for relatively realistic analysis of the core transients in an RBMK plant.

**Keywords**
Neutron flux, cross section, code, reactivity, critical facility, effective multiplication factor, detector, copper foil, fission chamber, ARROTTA, CASMO-4, database, INPP, fuel.

# Acknowledgments

I want to express my gratefulness to Professor Bal Raj Sehgal for providing me with a project and assisting me throughout with his extensive experience and expertise.

This research was supported by Swedish International Project (SIP) and I am very thankful for this support.

I especially want to thank my colleges Dr. Cheng Hongwu, Alexey Balygyn and Andrey Kubarev for their patience in discussions and professional advises.

I am grateful for Dr. Evaldas Bubelis for his assistance getting hardly accessible information and databases from the Ignalina Nuclear Power Plant.

I would like to thank the staff of the Division of Nuclear Power Safety at the Royal Institute of Technology in Stockholm, Sweden.

Finally, I want to give my warm thanks to my wife Laima Romienė and daughter Emilija Romaitė for their support and encouragement.

# Table of Contents

**ABSTRACT** ..... **III**

**ACKNOWLEDGMENTS** ..... **V**

**TABLE OF CONTENTS** ..... **VII**

**1 INTRODUCTION** ..... **1**

**2 2. RBMK-1500 REACTOR DESIGN** ..... **3**

2.1 INTRODUCTION ..... 3
2.2 GENERAL CHARACTERISTICS OF RBMK-1500 REACTOR ..... 3
2.3 CORE DESIGN ..... 5
*2.3.1 Core Housing* ..... *5*
*2.3.2 RBMK Fuel* ..... *6*
*2.3.3 Control Rods and Instrumentation of Neutron Flux Measurements* ..... *7*

**3 MODIFICATION OF THE ARROTTA CODE AND DEVELOPMENT OF THE PROCESSING CODES** ..... **9**

3.1 INTRODUCTION ..... 9
3.2 ARROTTA CODE MODELS ..... 10
3.3 ARROTTA CODE CROSS SECTION LIBRARY GENERATION AND THE CASE CONFIGURATION INPUT FILE ..... 13
*3.3.1 CASMO-4 Code and Calculation of Cross Sections* ..... *14*
*3.3.2 Processing of Basic Cross Section Library* ..... *16*
*3.3.3 The INPP Database* ..... *17*
*3.3.4 Database Converter and Reactor Core Data Processing* ..... *18*
*3.3.5 Generation of the ARROTTA Input Deck* ..... *19*
3.4 METHODS FOR COMPARISON OF RESULTS ..... 19

**4 VALIDATION OF ARROTTA AGAINST EXPERIMENTAL RBMK CRITICAL FACILITY DATA** ..... **23**

4.1 INTRODUCTION ..... 23
4.2 CRITICAL FACILITY DESIGN ..... 23
4.3 INSTRUMENTATION OF THE CRITICAL FACILITY ..... 27
4.4 PREPARATION OF CROSS SECTIONS ..... 28
4.5 CRITICAL ASSEMBLY MODEL AND DATA COMPARISON FORMALISM ..... 29
4.6 ANALYSIS OF THE ECF-TYPE EXPERIMENTS ..... 32
*4.6.1 Analysis of the ECF Experiment 1* ..... *32*
*4.6.2 Analysis of the ECF Experiment 2* ..... *34*
*4.6.3 Analysis of the ECF Experiment 3* ..... *36*
*4.6.4 Analysis of the ECF Experiment 4* ..... *38*
*4.6.5 Analysis of the ECF Experiment 5* ..... *39*
4.7 ANALYSIS OF THE EFC TYPE EXPERIMENTS ..... 42
*4.7.1 Analysis of the EFC Experiment 1* ..... *44*
*4.7.2 Analysis of the EFC Experiment 2* ..... *47*

*4.7.3 Analysis of the EFC Experiment 3* ..... *50*
4.8 CONCLUSIONS ..... 53

**5 APPLICATION OF REACTOR PHYSICS CALCULATION CAPABILITIES AT KTH FOR RBMK ANALYSIS ..... 55**

5.1 ANALYSIS OF RBMK-1500 FUEL CHARACTERISTICS BY CASMO-4 CODE AND INVESTIGATION OF POSITIVE VOID REACTIVITY CAUSES ..... 55
*5.1.1 Introduction* ..... *55*
*5.1.2 Model for the CASMO-4 Computations* ..... *55*
*5.1.3 Reactivity Effects and Coefficients* ..... *58*
*5.1.4 Causes of Positive Coolant Void Reactivity* ..... *64*
*5.1.5 Conclusion* ..... *76*
5.2 MODELING OF A HYPOTHETICAL FUEL DROP EVENT ..... 79
*5.2.1 Introduction* ..... *79*
*5.2.2 Refueling Procedure* ..... *79*
*5.2.3 Mechanical-Hydraulic Model of the Fuel Drop Event* ..... *81*
*5.2.4 Results of Mechanical-Hydraulic and Reactor Physic Calculations* ..... *84*
*5.2.5 Conclusions* ..... *87*

**6 SUMMARY AND CONCLUSIONS ..... 89**

**7 NOMENCLATURE ..... 91**

7.1 ABBREVIATIONS ..... 91
7.2 ARABIC ..... 91
7.3 GREEK ..... 92
7.4 SUBSCRIPTS ..... 93

**8 REFERENCES ..... 95**

# 1 Introduction

The increasing interest in improving the safety of RBMK-type reactors has heightened the need for computational tools, which would provide accurate predictions for the steady state, transients, and accident operational conditions for such plants. Of particular interest is the transient behavior of the RBMK core. Clearly, the Chernobyl accident resulted primarily from the exceeding faulty safety characteristics of the core. We believe that unlike an LWR plant, the RBMK plant safety depends heavily on the safety characteristics of its core and the effectiveness of its control actions. Thus the accurate predictions of the reactor core characteristics of the core transient behavior and of the adequacy of the control actions have great importance for the resolution of the safety issues of nuclear power plants operating the RBMK reactors.

After the Chernobyl accident, the fuel in most of the RBMK plants was changed from 2% to 2.4% enrichment and a large number of additional absorbers were added to the core. The INPP has been changing its 2% enriched fuel to 2.4% fuel containing erbium burnable absorber. The INPP is also removing the additional absorbers as the core is progressively loaded with the Erbium-poisoned fuel. The study of the core safety characteristics with erbium fuel has become an important aspect of the INPP safety analysis since 1994 [16].

The RBMK-type reactors have been extensively studied in Russia during many years. Several neutronics codes STEPAN, BARS and SADCO have been developed for RBMK reactor physics computations. Among these, the STEPAN [17] code is used at Kurchatov Institute, and by INPP personnel.

In 1990s, efforts were made to modify two codes developed in the Western countries for the RBMK reactor applications. The first code, CUBOX-QUABOX, was developed and modified at GRS, Germany. The second code, ARROTTA, was developed at EPRI and modified for RBMK at PSI, Switzerland [20]. Both of these codes employed the cross section library that was developed in Russia with the WIMS-$D_4$ code for the STEPAN, and the SADCO codes.

It is of interest to compare the predictions made by the Russian codes for the INPP core steady state, transient and accident behavior against those obtained with the Western codes employing two group cross sections calculated with the CASMO code using the latest ENDF/B data files. These codes to code comparisons will certainly provide a check on the safety analysis results in the INPP SAR, which were obtained with the Russian codes.

The aim of this study first of all is to modify and adapt the ARROTTA code for the INPP safety studies and to perform validation of that code against experiments conducted in RBMK critical facility. The ARROTTA code, originally developed for

light water reactor (LWR) core transient analysis, was modified and adapted for the RBMK core analysis. The modifications and adaptations of the ARROTTA code includes a) developing and modification processing codes for the constructing the ARROTTA cross section library from CASMO code calculations b) developing processing codes, which would access the Ignalina plant core configuration and database, and convert that to the required input file for the ARROTTA code and c) modifying the code to represent the different control rods in an RBMK plant. Full core representation (individual representation of all fuel, control rod and reflector assemblies) and analysis capability was developed. The ARROTTA code original cross-sections model and cross-section data processing system were adapted for Ignalina Nuclear Power Plant (INPP) reactor's analysis.

The ARROTTA code was applied for analysis of core transients for INPP. A hypothetical fuel drop event with disabled local control and protection system in the INPP was analyzed. A mechanical-hydraulic model was developed to calculate fuel bundle velocity.

The second chapter of this thesis describes the general characteristics and construction futures of RBMK-1500 reactor.

The third chapter describes codes adapted and developed for the RBMK analysis at the Nuclear Power Safety Division of KTH. This chapter briefly describes models used in the ARROTTA code and the process of cross section library generation. In addition, two post-processing codes, developed for the ARROTTA result comparison with the measurements in the INPP, are presented.

The fourth chapter is dedicated to description of the RBMK experimental critical facility and the experiments performed. Several critical experiments were simulated by the ARROTTA code and results obtained were compared with measurements.

The fifth chapter is concentrated on RBMK fuel analysis by CASMO-4 lattice code. The safety characteristics calculated for three fuel types are presented. This chapter attempts to explain the causes, which determine the variation of positive coolant void reactivity. The chapter also includes studies of the hypothetical fuel drop event in the INPP.

The last chapter provides a summary of the work performed and the results obtained. This chapter also provides the conclusions of this thesis.

# 2 2. RBMK-1500 Reactor Design

## 2.1 Introduction

The RBMK-type reactors (Russian acronym for “Channeled Large Power Reactor”) were built exclusively within the land area of the former Soviet Union. Totally there are 17 nuclear units, and 15 are currently in operation. Eleven of these operating units are in Russia, two in Ukraine and two in Lithuania.

The Ignalina Nuclear Power Plant (INPP) contains two RBMK-1500 type reactors, and is located in the northeast part of Lithuania. The INPP was constructed while Lithuania was part of the Soviet Union. The first unit started to operate in December 1983 and the second unit in August 1987. The designed lifetime of these units is up to the year 2010 or possibly 2015.

The RBMK-1500 reactor models are built only in the INPP. This model is the most advanced version of the RBMK reactor and this reactor is more powerful in comparison to the Chernobyl NPP nuclear units. The RBMK-1500 reactor is capable of producing 1500 MWe (currently limited to 1300 MWe), while RBMK-1000 plants produce 1000 MWe. In addition, the RBMK-1500 is provided with an improved accident confinement system, which is used for steam condensation and localization. The accident confinement system functions as a containment would for a BWR reactor, however, the designed pressure capability of the system is relatively small (≤1 bar overpressure). The other characteristics are similar between RBMK-1500 and RBMK-1000 reactor models.

Until August 1991, the INPP was under the jurisdiction of the Soviet Union. The Ignalina NPP came under the authority of the Lithuania Republic after the collapse of the Soviet Union in August 1991. The INPP nuclear units are important for the economy of Lithuania, since this plant produces up to 87% of the total electrical power used in Lithuania. However, this plant is also of great concern to the West since it is of the same type as Chernobyl. Therefore, many efforts have been pursued by Lithuania and the Western countries to improve the safety of the INPP.

## 2.2 General Characteristics of RBMK-1500 Reactor

The RBMK reactor is a channel-type, graphite-moderated reactor. Fuel assemblies are loaded in fuel channels, which are separated from each other by graphite stacks. The graphite is used as a moderator for neutrons slowing down to the thermal energy range. The RBMK-type reactors are refueled on-line with the fuel employed, which used to be 2.0% enriched fuel, however, presently in the INPP, it is the 2.4% enriched fuel with Erbium poison.

The RBMK reactor contains two separate cooling loops designed for cooling of each half of the reactor core. The main characteristics of the RBMK-1500 are presented in Table 2.1.

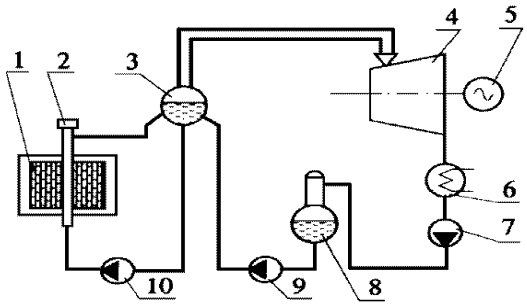


1-reactor, 2-fuel assembly, 3-separator drum, 4- turbine, 5-generator, 6-condenser, 7-condensate pump, 8-deaerator, 9-feedwater pump, 10-main circulation pump (MCP)

**Fig.2.1** RBMK heat cycle diagram [1]

The design of the steam-water system is similar to that in a Boiling Water Reactor (BWR) as shown in Fig.2.1. With the steam being produced in the reactor core (2), the steam-water mixture first passes through the separator drum where steam is separated from water, then is lead to the turbines (4). The condensate, which appears in the turbines after steam expansion and condensation in the condenser (6), is pumped to the deaerator (8). The feedwater (already cleaned in the deaerator) is

| | |
|---|---|
| **Coolant** | **water (steam-water mixture)** |
| **Heat cycle configuration** | **single circuit** |
| **Power, MW:** | |
| thermal (design) | **4800** |
| thermal (actual) | **4200** |
| electrical (design) | **1500** |
| **Core dimensions, m:** | |
| height | **7** |
| diameter | **11,8** |
| **Thickness of reactor's graphite reflector, m:** | |
| end | **0,5** |
| side | **0,88** |
| **Lattice pitch, m** | **0.25 x 0.25** |
| **Number of channels:** | |
| fuel | **1661** |
| control and shutdown system | **235** |
| reflector-cooling | **156** |
| **Fuel** | **uranium dioxide** |
| **Initial fuel enrichment for $^{235}$U, %** | **2.0 and 2.4 with Erbium** |
| **Nuclear fuel burnup, MWdays/kg** | **21.6*** |
| **Number of main circulation pumps** | **8** |
| **Capacity of main circulation pumps, $m^3/s$ ($m^3/h$)** | **1.805 - 2.22 (6500 - 8000)** |
| **Temperatures, $^oC$:** | |
| maximum acceptable temperature at center of fuel pellet | **2600** |
| maximum acceptable graphite stack temperature | **760** |
| maximum acceptable fuel cladding temperature | **700** |
| maximum acceptable fuel channel temperature | **650** |
| coolant temperature at fuel channel inlet ** | **260 - 266** |
| feedwater temperature ** | **177 - 190** |

*At fuel enrichment for $^{235}$U 2%.
**At 4200 MW (th).

**Table 2.1** Main Characteristics of the RBMK-1500 reactor [1]

| Parameter | BWR * | RBMK |
|---|---|---|
| Thermal power, MW | 3800 | 4800 |
| Core diameter, m | 5.01 | 11.8 |
| Core height, m | 3.81 | 7 |
| Core volume, $m^3$ | 75 | 824 |
| Mean specific power per core volume, $MW/m^3$ | 51 | 5.82 |
| Mean specific power per fuel quantity, MW/t | 24.6 | 25.4 |
| Mean power per fuel element length, kW/m | 19 | 15 |

* General Electric design

**Table 2.2** Comparison of BWR and RBMK-1500 reactor parameters [1]

forced by the feedwater pump (9) to the separator drum, and is mixed with the water separated from the steam-water mixture. The separator drum water is taken by Main Circulation Pumps (10) (MCP), and distributed in the fuel channels in the core.

Table 2.2 compares general core design characteristics for BWR and RBMK reactors. It indicates that specific fuel power is similar for the both reactor types, but the volumetric core power differs considerably. The volumetric core power differs because the RBMK core occupies 11 times larger volume than that of a BWR.

## 2.3 Core design

### 2.3.1 Core Housing

The core housing of an RBMK-1500 reactor is shown in Fig.2.2. As shown there, the reactor core is housed in a 25m deep, 21×21m concrete vault. The upper part of the core is occupied by the top metal structure filled with serpentinite (2), and the top cover (1), which is the removable floor of the central hall.

The periphery of the core is surrounded by a reactor vessel (7) and biological-shield tank filled with water (5). The tank is surrounded by the sand cylinder (4) and concrete vault (3). All these design components form biological shielding and core support.

The major volume of the reactor core is stacked with graphite bricks that are supported by the metal structure (8) at bottom. The graphite blocks are rectangular parallelepipeds with cylindrical openings of 0.114m diameter. The size of graphite bricks is 0.25×0.25m and heights are 0.2, 0.3, 0.5, and 0.6m. The blocks are placed one on another, and form 2488 columns that fill the reactor cavity. The holes in the blocks form vertical openings where fuel and special-purpose

channels are positioned. There are totally 2044 channels, which are used for loading of fuel assemblies, additional absorbers, control rods and several types of instruments. The rest of the graphite columns are located in the periphery of the core and filled with graphite rods. These stacks function as the radial reflector.

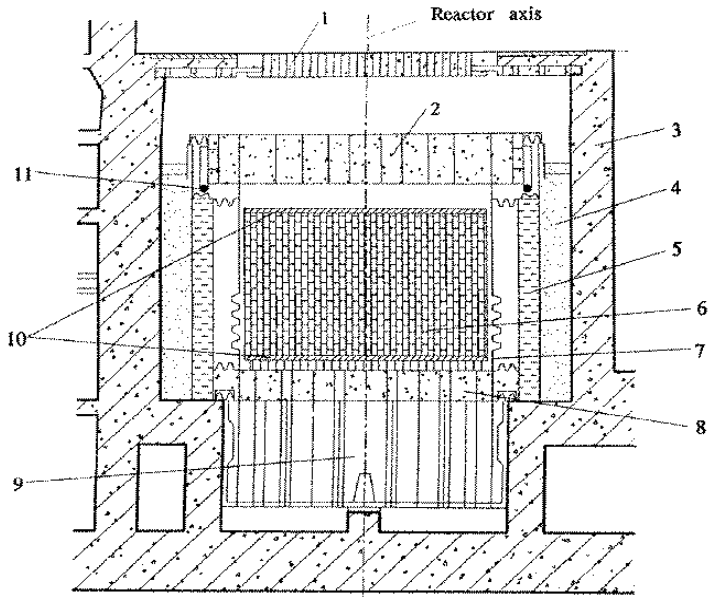


1-top cover, removable floor of the central hall, 2-top metal structure filled with serpentinite, 3-concrete vault, 4-sand cylinder, 5-annular water tank, 6-graphite stack, 7-reactor vessel, 8-bottom metal structure, 9-reactor support plates, 10-steel blocks, 11-roller supports

**Fig.2.2** Cross view of the reactor vault [1]

### 2.3.2 RBMK Fuel

The fuel channel tube is made of zirconium and niobium alloy, and located in the cylindrical openings of graphite stacks (see Fig. 2.3). The RBMK reactor core contains 1661 of such fuel channels, which are 88mm outer diameter while the diameter of graphite opening is 114mm. The space between the graphite and the fuel channel is occupied by graphite rings. The fuel assemblies are of cluster type, and contain two sections 3.4m long each in the axial direction.

The cluster bundle is comprised of 18 fuel rods of 13.6mm outer diameter. The claddings of these rods are made of zirconium-niobium alloy. The pellets are 11.5mm in diameter with 2mm diameter openings in the center.

The fuel that is enriched by 2.0% was originally used in the Ignalina NPP. This fuel type induced a large positive void coefficient with higher fuel burnup.

Recently, the 2.4% enriched fuel with the burnable poison 0.41w/% $Er_2O_3$ was introduced.

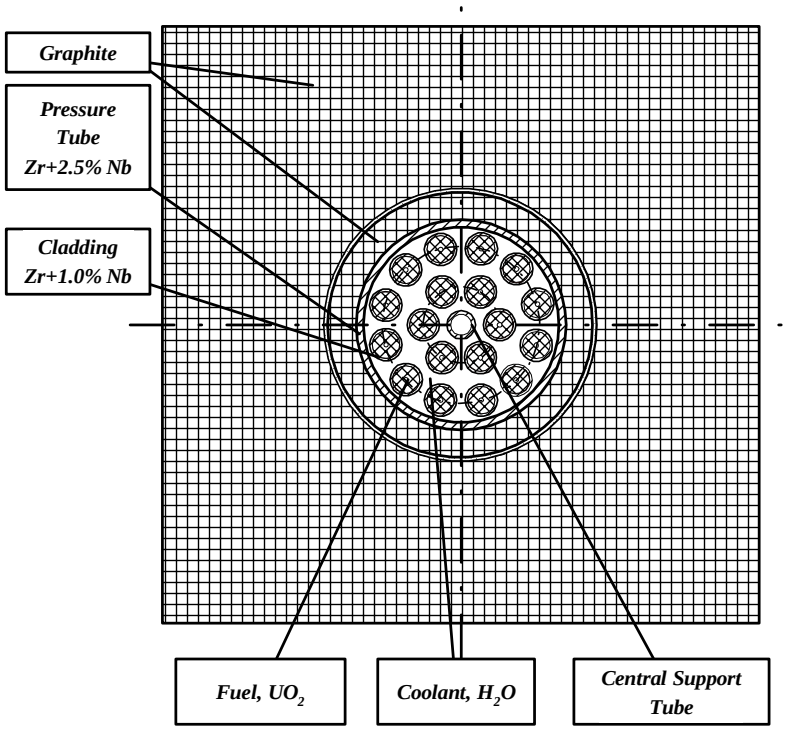


**Fig.2.3** Cross view of fuel cluster, which is loaded in the vertical opening of graphite block

### 2.3.3 Control Rods and Instrumentation of Neutron Flux Measurements

The RBMK reactor core power is controlled by $B_4C$ cylindrical control rods that are located in Control Protection System (CPS) channels. These channels are cooled by the CPS cooling system that is separate from Main Circulation Circuit (MCC) loop, which cools the fuel channels. The CPS coolant temperature is 40-90$^0$ C.

The INPP reactors contain three types of control rods, namely, Manual Control Rods (MCR), Short Control Rods (SCR), and Fast Acting scram Rods (FASR). There are a total of 211 control rods in this core [1]. All these control rods are driven by the electrical driver mechanisms, which are located on the top of the reactor core. The MCR and FASR control rods are inserted from the top of the reactor while the SCR control rods are inserted from the bottom of the core.

Recently, the MCR control rods has been re-designed in order to eliminate water column, which was present in original design.

The design of absorber part is similar for all types of control rods. The absorber is manufactured as boron carbide cylinder of 66mm outer diameter and 50mm inner diameter (34.5mm outer and 25.0mm inner diameter for FASR). However, the length of the absorber part is different for the different type of control rods [1].

The design of the MCR and SCR includes a graphite displacer that removes water in the CPS channels. However, the MCR and SCR design can not fully expel the water column between absorber and displacer. Therefore, the MCR was modified by adding a “skirt” to the absorber part and increasing the length of displacer.

The FASR-type control rod does not contain the graphite displacer. These control rods are designed to scram the core in 2.5sec. The FASR channels are cooled with water film and nitrogen.

For power monitoring the neutron flux is measured by two methods. In the first method, the neutron flux is measured by a high precision detector system, located outside of the core, which uses: four fission chambers, eight ionization chambers during reactor startup, and sixteen ionization chambers during normal reactor operation.

In the second method, the neutron flux is measured by in-core detectors. For the radial power distribution measurements, there are 127 non-inertial sensors with hafnium oxide (PDMS-R1) and 125 inertial sensors with silver (PDMS-R2) [1]. They are loaded in the center of fuel assemblies.

The axial neutron flux distribution is measured by 160 in-core power detectors of axial monitoring system (PDMS-A). The PDMS-A gamma detectors are located in twelve CPS channels, which are evenly distributed within the reactor core, and in eight channels, which are located at the periphery of the core. Each PDMS-A channel contains eight detectors distributed axially along the length of channel.

# 3 Modification of the ARROTTA Code and Development of the Processing Codes

## 3.1 Introduction

Several codes, e.g., STEPAN, BARS and SADCO, developed in Russia, have been employed for performing global-core neutronic calculations for the RBMK-type reactors. These computer programs are specially designed to perform static and dynamic calculations for the RBMK reactors, as for example, for determination of reactivity coefficients, for optimization of fuel reloading pattern and for transient analyses.

Recently, some Western codes such as CUBOX-QUABOX and ARROTTA, have also been modified and adapted for the RBMK safety research, since they were originally developed for LWR analyses. The CUBOX-QUABOX program was developed in 1970s and recently modified at GRS, Germany. The other code, ARROTTA, was developed by Sol Levy Associates for EPRI. In 1994, this code was modified for the RBMK safety studies at PSI, Switzerland in cooperation with S. Levy, Inc. A cross section library created by Russian experts using WIMS-$D_4$ lattice code was employed by these two codes for the RBMK analyses.

In 1998, the ARROTTA code was modified and adapted for analyses of the INPP at the Division of Nuclear Power Safety (NPS) of the Royal Institute of Technology (KTH). A set of processing codes employed for generating the two group regional cross sections for the ARROTTA code from the series of lattice calculations performed with the CASMO code were also adapted so that appropriate two group cross sections may be generated for the fuel regions of the RBMK core.

In addition, the ARROTTA code was modified to model the INPP control rods and their movements in response to the various signals that are generated during core steady state and transient operations. This work was done by other personnel at NPS/KTH.

Finally, a set of preprocessing codes were developed through which the core configuration database generated by the plant personnel every day could be transformed into the input for the ARROTTA code. Through these codes each assembly of the INPP core with their respective burnup and other characteristics are represented in the CASMO lattice and in the ARROTTA whole core calculations.

In the following sections details of adapted and developed codes are described.

## 3.2 ARROTTA Code Models

The ARROTTA (Advanced Rapid Reactor Operational TransienT Analysis) computer program is a three-dimensional space-time kinetics and thermal-hydraulics code designed for LWR's static and transient analysis, where spatial effects are significant and thermal-hydraulic feedbacks are important [6]. The ARROTTA code can be employed to solve for steady-state reactivity changes, and describe the xenon and samarium, and kinetics transients such as loss of coolant or rod ejection accident.

The neutronics model of the ARROTTA code is based on the Analytic Nodalization Method (ANM) by employing the transverse integration procedure. The transient neutron balance equations (see Eq.3.1 and 3.2 [6]) are solved and the solution of a system of equations is determined if a node is considered as homogeneous entity and the shape of transverse leakage is approximated in a quadratic form.

$$\mathrm{v}_1^{-1}(\mathbf{r})\frac{\partial \Phi_1}{\partial t}(\mathbf{r},t) = -\nabla\cdot\mathbf{J}_1(\mathbf{r},t) - \Sigma_{t_1}(\mathbf{r},t)\Phi_1(\mathbf{r},t) + (1-\overline{\beta}(\mathbf{r}))\sum_{g=1}^{2}\nu_g\cdot\Sigma_{f_g}(\mathbf{r},t)\Phi_g(\mathbf{r},t) + \sum_{d=1}^{D}\lambda_d C_d(\mathbf{r},t) \qquad \textbf{Eq. 3.1}$$

$$\mathrm{v}_2^{-1}(\mathbf{r})\frac{\partial \Phi_2}{\partial t}(\mathbf{r},t) = -\nabla\cdot\mathbf{J}_2(\mathbf{r},t) - \Sigma_{t_2}(\mathbf{r},t)\Phi_2(\mathbf{r},t) + \Sigma_R(\mathbf{r},t)\Phi_1(\mathbf{r},t) \qquad \textbf{Eq. 3.2}$$

Here, **r** is three dimensional position vector and *t* stands for time. The neutron group energy is indicated by *g*. Fast neutron group is marked as 1 and thermal neutron group as 2. D is the total number of delay neutron groups. $\Phi_g(\mathbf{r}, t)$ is the neutron flux and $\mathbf{J}_g(\mathbf{r}, t)$ is the net current vector in group g. $C_d(\mathbf{r}, t)$ represents the delay neutron precursors for delay neutron group d. $\Sigma_{tg}(\mathbf{r}, t)$ is the total macroscopic absorption cross section plus removal cross section in group g. $\Sigma_{fg}(\mathbf{r}, t)$ stands for fission macroscopic cross section in group g. $\Sigma_R(\mathbf{r}, t)$ is the macroscopic scattering removal cross section for the group 1 to 2 transfer. $\nu_g$ represents mean number of neutrons emitted per fission in group g. $\lambda_d$ is decay constant for precursor in group d. $\overline{\beta}_d(\mathbf{r})$ is the effective fraction of fission neutrons emitted from delay precursor group d. $\mathrm{v}_g$ stands for averaged neutron speed in group g and is assumed to be time independent.

The balance equations for the precursor concentrations are written as Eq.3.3.

$$\frac{\partial C_d(\mathbf{r},t)}{\partial t} = \overline{\beta}_d(\mathbf{r})\sum_{g=1}^{2}\nu\Sigma_{f_g}(\mathbf{r},t)\Phi_g(\mathbf{r},t) - \lambda_d C_d(\mathbf{r},t) \qquad d = 1,\ldots,D \qquad \textbf{Eq. 3.3}$$

The initial concentrations of precursors are determined by solving equation 3.4.

$$C_d(\mathbf{r},0) = \frac{\overline{\beta}_d(\mathbf{r})}{\lambda_d}\sum_{g=1}^{2}\nu\Sigma_{f_g}(\mathbf{r},0)\Phi_g(\mathbf{r},0) \quad d = 1,\ldots,D \qquad \textbf{Eq. 3.4}$$

Neutron cross sections used in the diffusion equations are calculated according to a cross section model that accounts for thermal-hydraulic feedbacks and poison isotopes. This model includes variation of macroscopic cross sections due to changes in coolant density or void, control rod presence, moderator and fuel temperature, and inventory of poison isotopes such as $B^{10}$, $Xe^{135}$, $I^{153}$, $Sm^{149}$, and $Pm^{149}$. The model is represented by Eq.3.5.

$$\begin{aligned}\Sigma = {} & R\cdot(A + B\cdot(x-x') + C\cdot(x-x')^2) + (1-R)\cdot(A' + B'\cdot(x-x') + \\ & C'\cdot(x-x')^2) + \frac{\partial\Sigma}{\partial T_M}\cdot(T_M - T_M') + \frac{\partial\Sigma}{\partial\sqrt{T_F}}\cdot(\sqrt{T_F} - \sqrt{T_F'}) \\ & + F(N_{B^{10}}, N_{Xe^{135}}, N_{I^{135}}, N_{Sm^{149}}, N_{Pm^{149}})\end{aligned} \qquad \textbf{Eq. 3.5}$$

Here

$x = \alpha$ , for BWR

$x = \dfrac{\gamma}{\gamma_{\mathrm{Re}\,f}} - 1$ , for PWR

The first and second terms in the right hand of the equation above represent the quadratic dependence of cross sections on coolant density or void. $x$ stands for nodal void fraction $\alpha$ for BWRs, or the normalized difference between the instantaneous nodal moderator density $\gamma$ and reference nodal density $\gamma_{Ref}$ for PWRs. This equation includes two distinct sets of quadratic coefficients for the rodded ($A'$, $B'$, $C'$) and unrodded ($A$, $B$, $C$) portions of node, respectively. $R$ is a monotonically increasing function of the nodal control fraction and that accounts for cusping effect of control rod.

The moderator temperature feedback is assumed to be linearly dependent on the moderator temperature $T_M$ and is represented by the third term in the right hand of the Eq.3.5. The Doppler effect was also assumed to be linearly dependent on the square root of the absolute fuel temperature $T_F$. Furthermore, the Doppler and moderator feedback mechanisms are assumed to be independent of the existence of control rods in a given composition.

The last term in the right hand of the Eq.3.5 accounts for changes of cross sections due to poisoning by fission products. This term is used in xenon transient analysis and xenon equilibrium initialization. However, the equilibrium concentration of xenon and samarium is assumed to be invariant throughout other transients.

Thus, to model variation of cross sections in ARROTTA, 54 parameters are needed to describe the functional behavior the x-variation of the moderator – six for each of nine cross section types listed by Table 3.1. Another nine coefficients are needed for moderator temperature feedback, and the variation of fuel temperature adds five more coefficients.

In addition to the coefficients indicated in the Table 3.1, the reference temperatures of fuel and moderator, and the reference value of the x-variable are required as well. The ARROTTA input also includes assembly discontinuity factors (ADF), kinetic parameters, and microscopic absorption cross sections of poison isotopes.

| ***Cross Section*** | ***Energy Group*** | ***Notation*** | ***Coolant Density*** | ***Moderator Temperature*** | ***Fuel Temperature*** |
|---|---|---|---|---|---|
| ***1. Diffusion*** | ***1*** | $D_1$ | ***6*** | ***1*** | ***1*** |
| ***2. Diffusion*** | ***2*** | $D_2$ | ***6*** | ***1*** | **-** |
| ***3. Absorption*** | ***1*** | $\Sigma_{a1}$ | ***6*** | ***1*** | ***1*** |
| ***4. Absorption*** | ***2*** | $\Sigma_{a1}$ | ***6*** | ***1*** | **-** |
| ***5. Removal (Scattering)*** | ***1->2*** | $\Sigma_{s1->2}$ | ***6*** | ***1*** | ***1*** |
| ***6. Fission Neutrons*** | ***1*** | $\nu\Sigma_{f1}$ | ***6*** | ***1*** | ***1*** |
| ***7. Fission Neutrons*** | ***2*** | $\nu\Sigma_{f2}$ | ***6*** | ***1*** | **-** |
| ***8. Fission Energy*** | ***1*** | $\kappa\Sigma_{f1}$ | ***6*** | ***1*** | ***1*** |
| ***9. Fission Energy*** | ***2*** | $\kappa\Sigma_{f2}$ | ***6*** | ***1*** | **-** |

**Table 3.1** List of coefficients required by the ARROTTA cross section model

The temperatures and coolant density or void, used in the cross section model, is calculated by a thermal-hydraulic model that includes a fluid dynamics model and a heat transfer model. The fluid dynamics is described by an inhomogeneous, non-equilibrium, two-phase flow that is based on energy splitting between the phases. This model is based on one-dimensional conservation equations for multiple parallel flow channels by taking into account five possible flow regimes. The heat conduction model includes heat conduction in a fuel pellet, in a gap between the pellet and the cladding, and in the cladding. The conductivity is calculated as a function of average temperatures in all sub-regions of the fuel pin.

The ARROTTA input file also requires the specification of core layout and axial composition for each assembly type, dimensions of each node, and control rod pattern.

## 3.3 ARROTTA Code Cross Section Library Generation and the Case Configuration Input File

As mentioned earlier, the ARROTTA code has been adapted to perform RBMK-1500 steady state and transient calculations with a cross-section generation model developed by the code developers. The generation of cross section library is based on EPRI/ARMP-02 sequence of codes that is used for PWRs.

The whole process for cross section generation is shown in Fig.3.1. There are two branches of data flow in this figure. The first branch, which consists of CASMO-4, CAXCON, NORGEP and NTPREP codes, is used to process Basic Cross Section Library (BCSL). The BCSL, which is indicated as the TAPE21 file in the Fig.3.1, contains cross section data that are sorted according to assembly type, fuel burnup, fuel and coolant temperature, historical and instantaneous coolant density. The second branch, which includes the INPP database, DBC and CORESIM codes, deal with data transfer from the database files to the NEWTAP0 file. The NEWTAP0 file contains data that are used to construct the ARROTTA input file. The NEWTAP0 includes reactor core configuration, burnup distribution and coolant density history for each node.

The REBLEND code (see Fig.3.1) generates input deck for the ARROTTA run. The REBLEND code takes the data from NEWTAP0 file to interpolate the cross sections supplied by the TAPE21.

The ARROTTA input file is formed by taking the output from the REBLEND code, and adding some data manually. The information on inlet coolant flow distribution and initial positions of control rods is obtained from the database by using the DBC code.

The ARROTTA calculated results are processed for comparison with the INPP data by two computer programs that are designed for validation of the ARROTTA code. The first code 3DPW (see Fig.3.1) accesses the three-dimensional power distribution calculated by the ARROTTA and compares it with the corresponding three-dimensional power distribution data from the INPP database. However, the 3D-power distribution from the INPP database is actually reconstructed on basis of measured data from a set of detectors placed at several locations in the core. Another code, PDMS, was developed to simulate this procedure.

The PDMS code takes ARROTTA results and makes comparisons with the measured data. The power and neutron fluxes measured in the reactor are stored in the database. The PDMS code identifies location of detectors in the core and their signals by exploring the database and estimates the discrepancies between the measured data and the results calculated by the ARROTTA code.

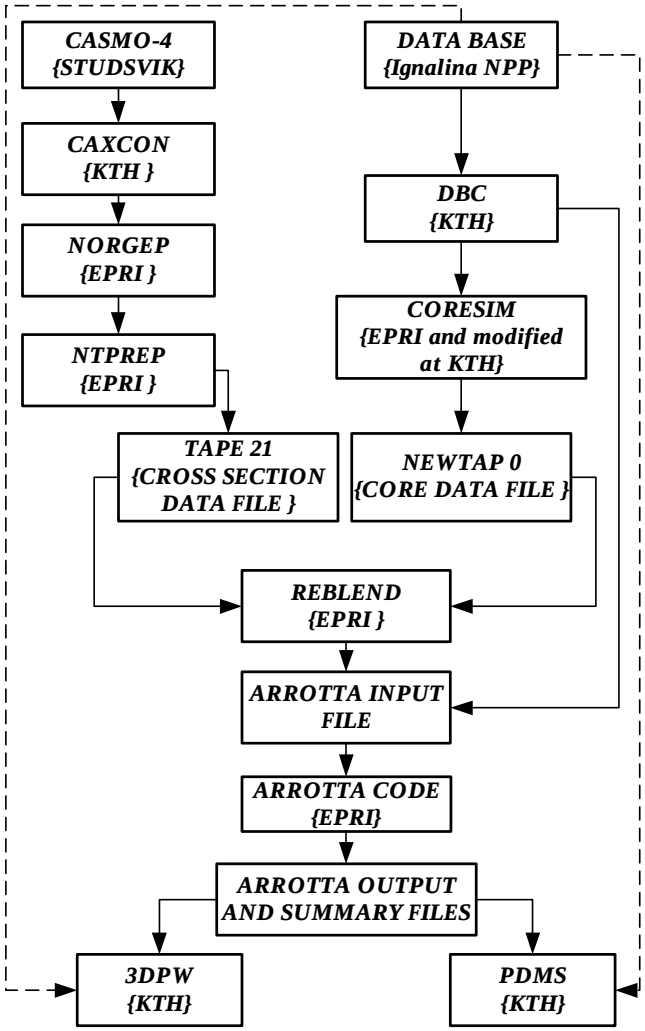


**Fig.3.1** Data flow for ARROTTA input file generation and analysis of simulation results

### 3.3.1 CASMO-4 Code and Calculation of Cross Sections

CASMO is a multigroup two-dimensional transport-theory lattice code for burnup calculations on BWR and PWR assemblies or simple pin cells. The code handles

geometry consisting of cylindrical fuel rods of varying composition in a square pitch array with allowance for fuel rods loaded with gadolinium a burnable absorber. Calculations by this code may also include cluster control rods, in-core instrument channels, water gaps, boron steel curtains, and cruciform control rods in the regions separating fuel assemblies [5].

The new futures of CASMO-4 included the microscopic depletion of burnable absorbers, such as Gadolinium and Erbium [5]. In addition, CASMO-4 is able to perform calculations for RBMK-type fuel assemblies of cluster geometry shown in Fig.2.3.

Some general characteristics of CASMO-4 are listed below [5]:

- ✓ Nuclear data are collected in a library based on Evaluated Nuclear Data Files /B (ENDF/B) and containing microscopic cross sections in 70 energy groups. Neutron energies cover the range 0 to 10 MeV. A library containing data in 40 energy groups is also available and is normally used in production runs.

- ✓ CASMO can accommodate non-symmetric fuel bundle containing 25×25 pins.

- ✓ The microscopic depletion is calculated in each fuel and burnable absorber pin.

CASMO has a simple user-oriented input. Default values are available for many input quantities and nuclear data are automatically read from the library. The user may specify the energy group structures and regions for which output is desired [5]. The boundary for the thermal energy group was defined as 4eV, and fast energy group is from 4eV to 10MeV in this study. The boundary for the thermal energy group was selected to be 4 eV in order to avoid up-scattering of the thermal neutrons to the fast group.

As indicated in Fig.3.1, CASMO-4 was employed for cross section generation for all types of fuel assemblies used in the INPP. As many as five fuel types may be employed for reloading in the core. They have the same geometry, but the composition of fuel pellet and the content of central instrumentation rod are different. Table 3.1 gives a general description of fuel enrichment for these five fuel types whose cross sections will be calculated.

The cross-sections are generated as a function of burnup, coolant void, and fuel temperature. The graphite temperature is assumed to be 750K, which is usually a nominal temperature at full reactor power, and is constant through the CASMO calculations. The ARROTTA code does not incorporate a model for graphite temperature calculations.

| Number | Lattice Name | Comments |
|---|---|---|
| 1 | Fuel 1 | 2.4 % enr. fuel mixed with $Er_2O_3$ oxide |
| 2 | Fuel 2 | 2.4 % enr. fuel mixed with $Er_2O_3$ oxide and gadolinium absorber |
| 3 | Fuel 3 | 2.0 % enr. Fuel |
| 4 | Fuel 4 | 2.0 % enr. with gadolinium absorber in the central rod |
| 5 | Fuel 5 | 2.06 % enr. regenerated fuel with $U^{236}$ 0.5196% weight mass of uranium |
| 6 | MCR and SAR | Includes boron carbide absorber, graphite displacer, and water column |
| 7 | Re-designed MCR | Includes boron carbide absorber, graphite displacer, and 'skirt' |
| 8 | FASR | Includes boron carbide absorber and empty channel |
| 9 | Reflector | Graphite block filled with graphite rods |
| 10 | Instrumentation | Channels with axial (PDMS-A) detectors and channels with fission chambers |

**Table 3.2** List of RBMK-1500 core assemblies

In the CASMO calculations, the fuel burnup was varied from zero to 25MWd/kg. The coolant void was considered to be 0, 35 and 90%, and two fuel temperatures (557 and 1000K) were considered to account for Doppler effect during the burnup calculations.

CASMO is not suitable for generation of cross sections for non-fuel assemblies, since it can not model 3×3 multi-assembly geometry. Therefore, the cross sections for non-fuel assemblies obtained with WIMS-$D_4$ code at the Kurchatov Institute were implemented into the ARROTTA cross section library used at KTH. They were calculated at nominal operation conditions.

### 3.3.2 Processing of Basic Cross Section Library

The nuclear cross sections are stored in separate output files generated by CASMO-4 and WIMS-$D_4$. The CAXCON program was designed for the linking of the lattice codes and NORGEP processing code. The CAXCON is programmed to select required information from the outputs of the CASMO-4 and WIMS-$D_4$ and store it in separate files in the format required by the NORGEP code.

Next, NORGEP processes raw nuclear data provided by CAXCON and saves in files for further computations. NORGEP is used for sorting data of each fuel type and defining fuel identification number for them. The NTPREP uses that information and generates a binary file TAPE21. This file is named Basic Cross Section Library (BCSL) accumulating cross-section data for two energy groups, kinetic parameters and ADF for all assembly-types.

### 3.3.3 The INPP Database

The INPP is equipped with a system, which collects signals from neutron flux detectors. The collected raw data are processed and passed into the Information Computing System (ICS). The processed information including radial and axial power distribution and deviation from power set points is displayed and used for automatic power control in a reactor. In addition, the ICS generates database (DB) files.

The database files include measured and calculated data of reactor core and external equipment. They are normally recorded in 166 files. Furthermore, the ICS produces a smaller database containing 19 files with the data required for three-dimensional neutronic code calculations. These data are core layout, radial and axial position of control rods, fuel burnup, coolant flow rate, records of neutron flux measurements by PDMS-R and PDMS-A detectors. This database is used as input for STEPAN code calculations in the INPP.

The axial fuel burnup distribution is calculated by the ICS, fitted into three coefficients for each individual channel, and saved in the database. The axial fuel burnup is analytically reconstructed by sinus function

$$B(z) = \sum_{i=1}^{3} N_i \cdot \sin\left(\frac{i \cdot \pi \cdot (z + \Delta h)}{H + 2 \cdot \Delta h}\right) \qquad \textbf{Eq. 3.6}$$

Here, the *B(z)* is a function of axial fuel burnup rate (MWd/m) profile and is reproduced in neutronics calculations by three coefficients $N_i$ that are saved in the database. Index *i* stands for interpolation coefficient sequence number (*i*=1, 2, 3). The origin of axial coordinate *z* is the bottom of the active core, and the maximum value of *z* is 7m, i.e. the active core height. *H* is core height (7m) and $\Delta h$ is the interpolated length (0.3m).

The Information Computing System also contains an algorithm for reconstructing the core power distribution. The power recovery is based on an interpolation of signals from radial (PDMS-R) and axial (PDMS-A) detectors. The axial power profile of each fuel channel is appraised and coded by four fitting coefficients by ICS, as done for burnup, which is fitted by three coefficients. In addition, one

more file is generated that includes the fitted axially integrated radial power distribution in the reactor core.

### 3.3.4 Database Converter and Reactor Core Data Processing

The database distributed by INPP is linked to the cross-section library processing system by use of Database Converter (DBC) code as it is indicated in Fig.3.1. The function of the DBC code is to select data from the database, convert, and save it in intermediate files and provide the information required by CORSIM, as well as that needed in the ARROTTA.

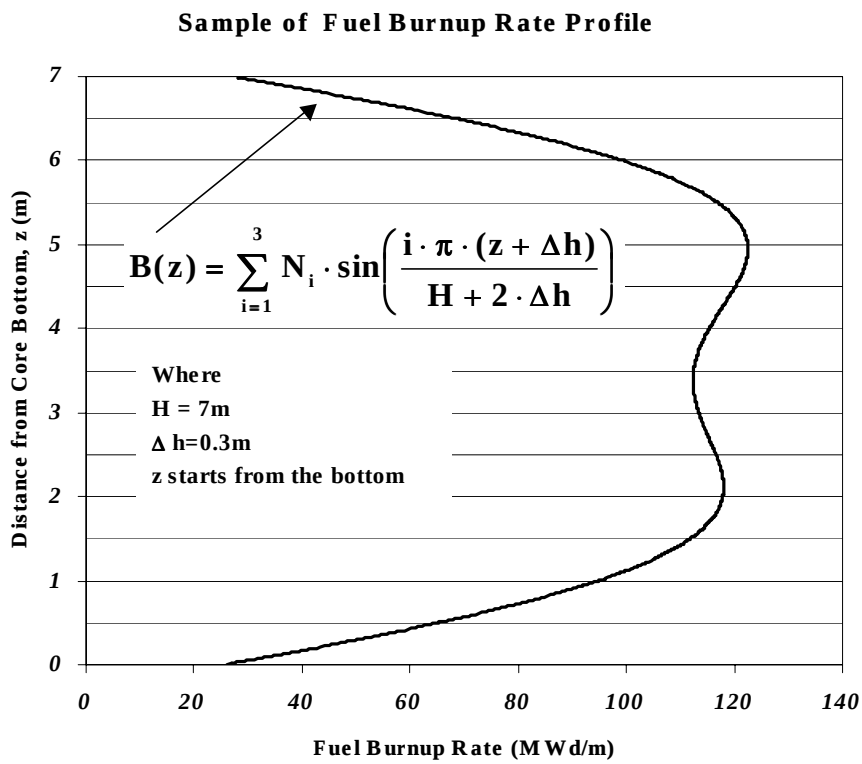


**Fig. 3.2** Typical axial fuel burnup rate profile recovered by the DBC code

The data required for cross section generation are core configuration, axial fuel burnup for each fuel channel, and axial coolant density. These data are further processed by CORSIM code and a binary file NEWTAP0 is generated. The information of radial and axial position of control rods and coolant flow rate in each channel is provided by DBC directly to the ARROTTA code. All the data from the database are converted considering coordinates and units used in the ARROTTA.

The Eq.3.6 has been implemented in the DBC program to calculate the axial burnup distribution for each fuel channel by using coefficients available in the database. As an example, the typical retrieved profile is shown in Fig.3.2. The Eq.3.6 is integrated with respect to the *z* in the boundaries of each node in order to calculate discrete burnup for each calculation node as required by the CORSIM code.

### 3.3.5 Generation of the ARROTTA Input Deck

The REBLEND code is executed after the binary files TAPE21 and NEWTAP0 are produced. TAPE21 contains all possible sets of cross sections for each assembly-type, and the NEWTAP0 file includes reactor core data. REBLEND is developed to reduce the number of compositions in the core according to the principle that the nodes of the same assembly type having similar burnup and historical coolant density belong to an identical composition.

For each node remaining after initial stack reduction, REBLEND interpolates nuclear cross sections and kinetics data as a function of assembly type, fuel burnup, fuel temperature, and moderator density history. The cross sections used for interpolation are taken from the TAPE21, and the interpolation reference points are provided by the NEWTAP0 file. The REBLEND code generates the ARROTTA input deck, which includes core layout, axial definition of each assembly, coefficients required in the cross section model and ADF.

The ARROTTA input file is completed by adding thermal-hydraulic data, which are calculated by the DBC code. In addition, the control data are processed by the DBC code in the format required by the ARROTTA code.

## 3.4 Methods for Comparison of Results

The power distribution retrieved by the ICS is regarded as the reference measurements for the evaluation of the ARROTTA results. Therefore, the INPP database is not only used to generate the ARROTTA input, but also to make comparison of the calculation results and the measurements. Since the format of the data from ICS is different from that of the corresponding ARROTTA results, the 3DPW code was developed to perform these comparisons.

The 3DPW code takes advantage of sets of four fitting coefficients for each fuel channel stored in the database, and calculates the axial power distribution for each fuel channel. The reconstruction of power profiles is based on integration of Eq.3.6 within the boundaries of each axial node defined by ARROTTA. The resulting profiles are then compared with the results calculated by ARROTTA.

It should be noted that the power distribution estimated by ICS is not really measured, but reconstructed by a computer code. Therefore, PDMS code was developed to perform automatic comparison of the calculated power and neutron fluxes with the ones measured by the PDMS-R and PDMS-A in-core detectors.

The signals of PDMS-A and PDMS-R detectors are recorded in the database and these records are employed for assessment of ARROTTA. PDMS identifies coordinates of radial and axial detectors, and extracts the signals measured by them from the database. Then, power and neutron flux calculated by ARROTTA at the location of detectors, are compared to the measured values.

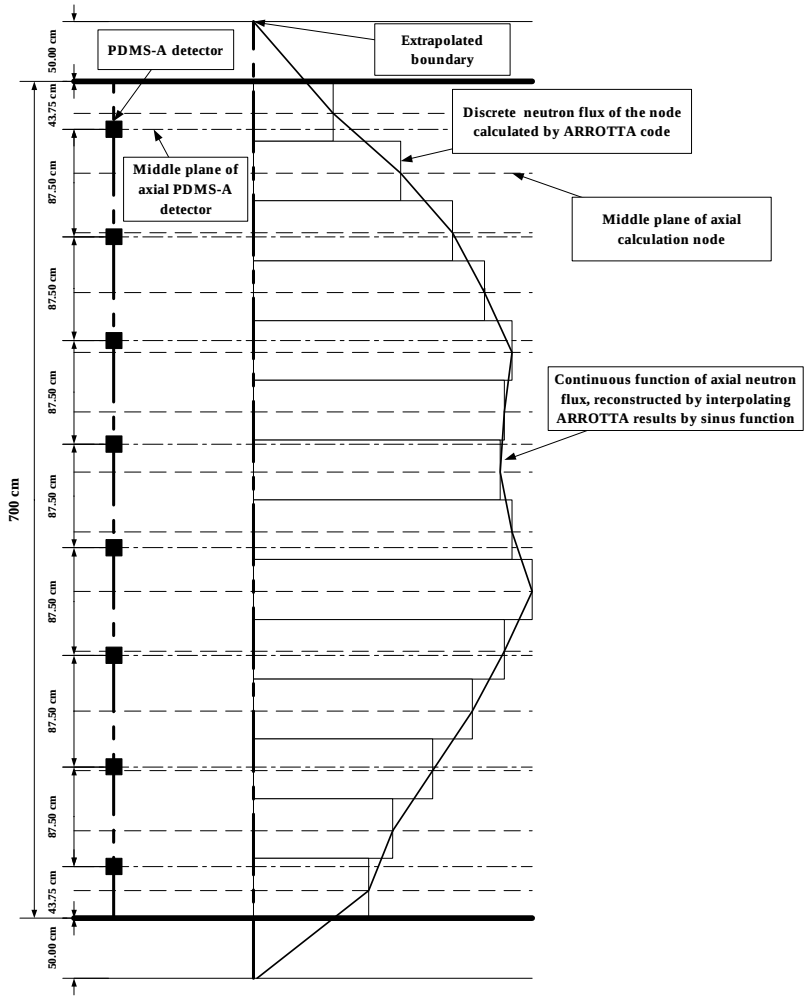


**Fig. 3.3** Schematics of comparison of calculated neutron flux against measured by PDMS-A detectors

The comparison of the radial power is straightforward, since signals of PDMS-R detectors are proportional to the integral power in the fuel channel, and are converted to power units by ICS. Thus, these data allow immediate comparison of measured integral power in fuel channel with corresponding power calculated by ARROTTA.

The comparison of measured and calculated axial neutron fluxes is more complex. A schematic of that process is shown in Fig.3.3. This figure visualizes axial location of neutron detectors and calculation nodes. As it is seen, ARROTTA provides discrete and discontinuous neutron flux for each node of 50cm height.

However, neutron flux is a continuos function in reality, and the PDMS code reconstructs that function from the data provided by ARROTTA output. This procedure involves an assumption that neutron flux by ARROTTA is valid only in the middle plane of each node (see Fig.3.3). The neutron flux is interpolated in between the middle planes of nodes by a sinus function and seven fitting coefficients are generated. Then, Eq.3.5 is used to calculate continuos neutron flux profile by employing the fitting coefficients. Finally, PDMS selects the calculated neutron flux at the location of neutron detectors and compares it with the corresponding measured neutron flux.

# 4 Validation of ARROTTA against Experimental RBMK Critical Facility Data

## 4.1 Introduction

All computer codes developed to simulate complex physical processes are based on some assumptions and approximations. Neutron static and space-time kinetics codes are no exception. It is extremely important that every code should be extensively validated and verified against experimental results or/and reference solutions, which are valid for comparison. To this respect sealing issues are very important, otherwise the conclusions of the validation effort may not hold. It is important that only properly validated codes should be employed for prediction of prototypical process at prototypical scale. There is doubly important for those codes, which are used in analyzing the safety of nuclear power plants.

Since 1980s, the ARROTTA code has been subjected to significant validation efforts for LWRs. Recently, ARROTTA has been employed for the RBMK core safety research, but its validation for RBMK-type reactors has not been carried out as comprehensively as for LWRs. The objective of the work presented in this chapter is to validate the ARROTTA code against data obtained in experiments performed in a RBMK-type zero-power critical assemblies that were constructed in a Critical Facility (CF) built in the Kurchatov Institute (KI).

The critical facility is comprised of various types of channels, whose contents can be changed as needed. The objective was that a flexible facility would be available in which to have performed a number of experiments with different core configurations could be constructed. The data measured in the experiments performed included (1) number of fuel bundles and positions of control rods to achieve criticality, (2) neutron fluxes and (3) control rod reactivity worths also during rod-withdrawal and rod-drop transients.

For the ARROTTA validation, eight representative critical experiments were analyzed with the ARROTTA code. The results calculated by ARROTTA were compared to the measured data. The comparisons involve effective multiplication factors (or eigenvalue), radial and axial neutron distributions, and control rod reactivity worth.

## 4.2 Critical Facility Design

The RBMK Critical Facility was designed at the Kurchatov Institute. This facility was aimed at obtaining experimental data on neutron flux distribution and investigating core reactivity changes caused by movement of control rods, by the filling of fuel and additional absorber channels with water.

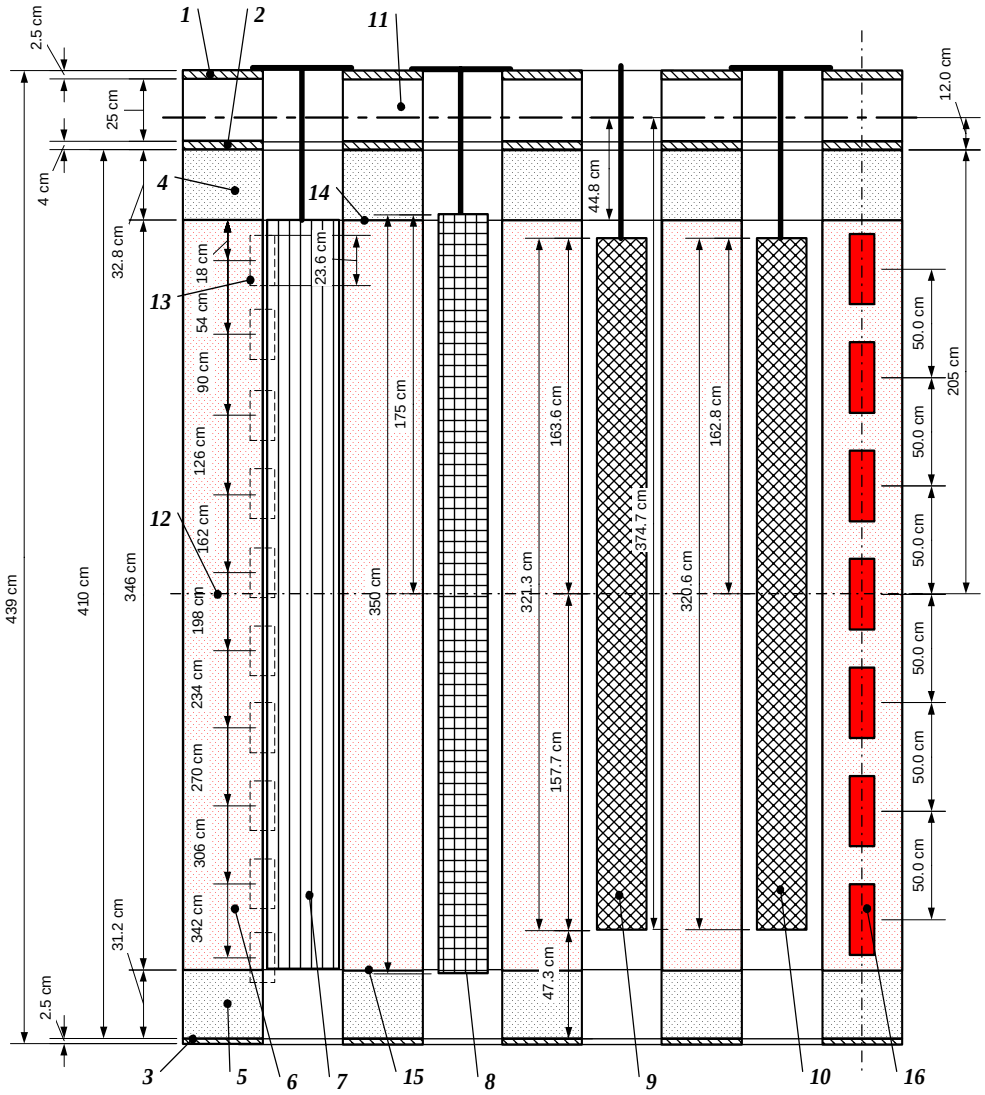


***1- boron-polythene plate, 2-aluminium plate, 3-steel plate, 4-top graphite reflector, 5-bottom graphite reflector, 6-graphite that is in active core, 7-fuel assembly (fuel pellets stack), 8-additional absorber (AA), 9-fully inserted control rod (CR.), 10-control rod imitator (CRY), 11-reference point of control rod position indicator (PI), 12-central line of graphite stack13-position of copper foils for neutron flux measurements, 14-top of the active core, 15-bottom of the active core, 16-axial position of KNK-5 fission chambers***

**Fig.4.1** Schematic of Critical Facility (CF), Kurchatov Institute, Moscow

The design of the critical facility was based on the prototype of an RBMK power reactor. The size of the whole critical facility is 450×450cm in base dimension, and 410cm high. Axially, it comprises of bottom graphite reflector of 31.2cm thickness, active core 346cm high, and top graphite reflector 32.8cm thick (see fig 4.1). The critical facility consists of 18×18 graphite stacks. These graphite stacks are assembled with rectangular 25×25cm graphite blocks having 11.4cm diameter cylindrical openings in the center. The graphite blocks are supported by 2.5cm thick steel plate. A 4cm thick aluminum plate is positioned in contact with the top of graphite stacks. In addition, a 2.5cm thick boron-polythene (2.7% boron by weight) plate is placed 25cm above the aluminum plate for biological shielding. A thin natural cadmium layer is attached to the boundary of the core.

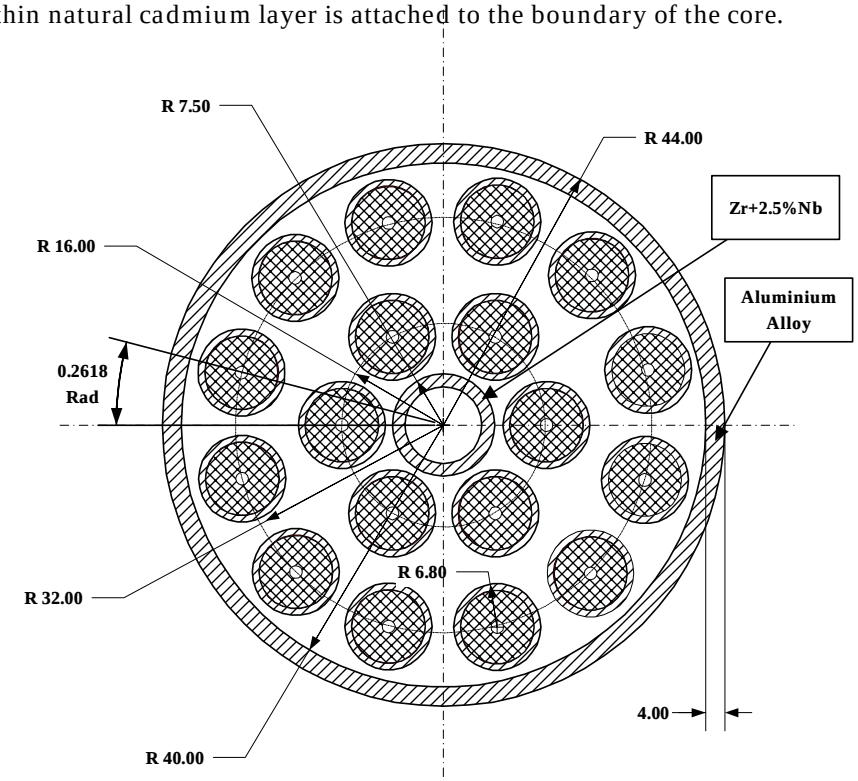


**Fig.4.2** Fuel cluster in the fuel channel

The channel tubes are placed vertically in the openings of graphite stacks, and separated from the graphite blocks by the graphite rings. The outer diameter of the graphite rings is 11.4cm and the inner is 8.9cm. The outer diameter of channel tubes is 8.8cm and the inner 8.0cm. The dimensions of the channel tube are the same as those of an RBMK-type reactor channel. However, the material of the channel tube in the critical facility is different from that in a RBMK power reactor. Aluminum alloy is used as the material of the critical facility channel tube while zirconium-niobium alloy is employed as the channel tube material in a RBMK reactor.

Fuel assemblies, additional absorbers, control rods and control rod simulators are loaded inside the aluminum channels. The fuel assemblies used in the critical facility experiments are of the same design as the fuel assemblies in the RBMK reactor core; the fuel cluster geometry loaded in the channel is shown in Fig.4.2. The only difference is that only the lower section of the RBMK fuel assembly is used in most cases, and length of that section is 365cm. In some experiments an upper section of the RBMK-1500-type reactor fuel assembly is also introduced. This fuel assembly segment contains more steel than in lower segment.

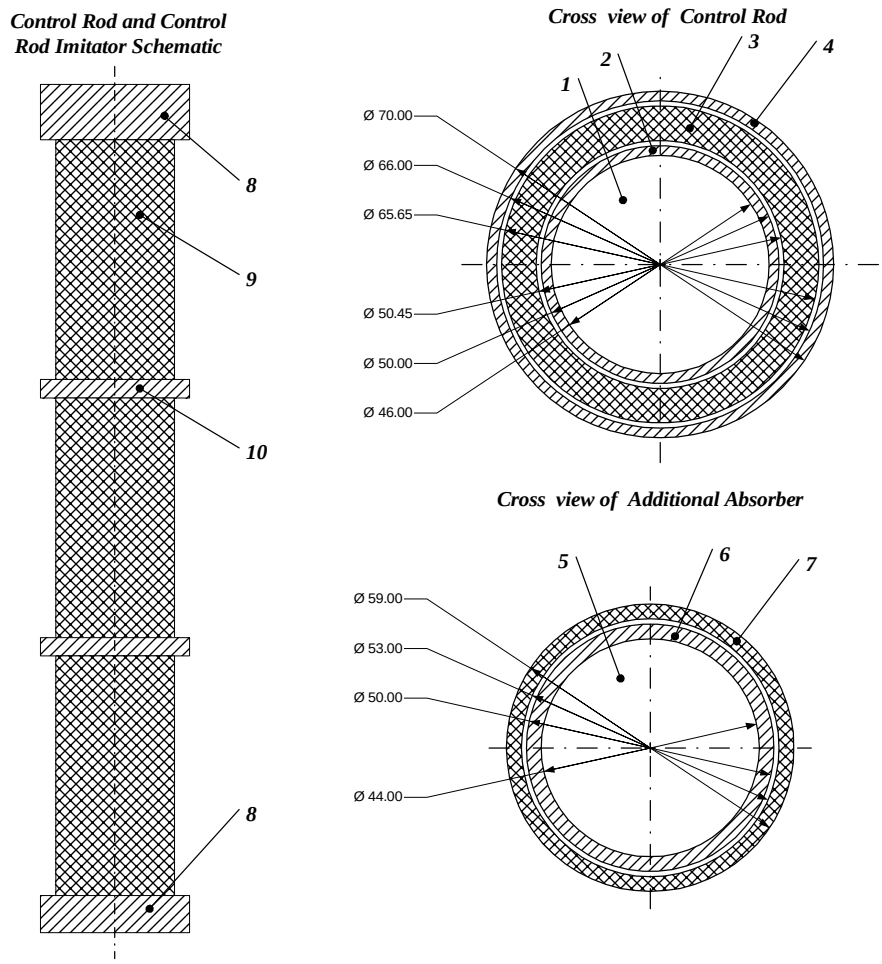


***1-inner cavity that is filled with air (for CRI might be water), 2-inner aluminium tube, 3-absorber ($B_4C$), 4-outer aluminium tube, 5-hermetically sealed inner cavity filled with air, 6-carrying stainless steel tube, 7- boron-steel (2.0% boron) absorber, 8-plugs, 9-absorber parts, 10-junctions***

**Fig.4.3** Control rod and additional absorber

Most of the fuel assemblies are enriched to 2.0%, and some are to 2.4%. The fuel channels, optionally, can be filled with water or be without water depending on the purpose of experiment.

Additional absorbers are used in some experiments. In the design of additional absorbers, as shown in Fig. 4.3, there is a stainless steel tube for supporting a boron-steel absorber tube. The stainless steel tube is sealed on both ends. The boron-steal absorber tube is 350 cm long, and contains 2.0% boron by weight. The additional absorber is symmetrically positioned with respect to the mid-plane of the graphite stack (205 cm under the top of the graphite stack). In some experiments, water may be surrounding the absorber tube.

A control rod (CRD) in the critical facility contains three cylindrical sections of the same size and of the same material. They are joined together by aluminum rings. Each cylindrical section includes two concentric aluminum tubes, the space between which is filled with natural $B_4C$ (see Fig. 4.3). The length of each section is 96.2 cm, and the entire length of the control rod is 321.3 cm including the space between the sections. The top of the control rod is 163.6 cm above the mid-plane of the graphite stack if the control rod is fully inserted in the core. The bottom of the control rod, fully withdrawn, is 12 cm away from the top of the graphite stack. The control rod channels are not filled with water for all the experiments performed. Position Indicator (PI) indicates an axial position of a control rod in the core. A starting point of the indicator is 12 cm above the top of graphite stack, i.e., the position indicator reads zero if the bottom of the control rod absorber is located 12 cm above the graphite stack. As a result, the bottom of the control rod absorber coincides with the top of the active core when the position indicator shows 44.8 cm. The tolerance of the position indicator is ±2.5 cm.

Generally, control rod imitators are of similar design as are the control rods. However, they are not movable in the core like additional absorbers. They are also about one centimeter shorter than normal control rod. The top of CRI stays 162.8cm above the mid-plane of graphite stack (see Fig.4.1 and Fig.4.3). The CRI channels may be filled with water in some experiments.

## 4.3 Instrumentation of the Critical Facility

For measuring neutron fluxes, induced activities of copper foils are measured in the first five experiments, called “Experiments using Copper Foils” (ECF) for convenience. The copper foils are 23.6×1.5×0.03cm in size, and are placed in the periphery of the fuel cluster during the experiments. The axial location of these foils is shown in Fig.4.1. The accuracy of this method varies between 1.5% and 7% [19].

In the other three experiments, KNK-5-type fission chambers are introduced for neutron flux measuring, and these are named “Experiments using Fission

Chambers" (EFC). There are 54 fission chambers evenly distributed in the mid-plane of the core. In two channels, there are seven detectors placed every 0.5m interval in the axial direction, as shown in Fig.4.1. In total 68 sensors are placed in special channels located in the corners of graphite locks.

Reactivity is determined by employing a PIR-4 reactimeter. The reactimeter accumulates signals from four ionization chambers distributed in the core, and performs reactivity calculations based on Inverse Point Kinetics theory. The accuracy of reactimeter (not considering errors due to neglect of the space effects, but only taking instrumentation error into account) is 1-2% in the case of a small reactivity change (less than 0.25$) and 5-6% for larger reactivity changes [19].

More detailed description of the critical facility is provided in reference 19. This reference also contains information on the materials used in the critical facility and describes the experimental results not considered in this thesis.

## 4.4 Preparation of Cross Sections

For generation of cross sections, two well-known lattice physics codes, namely, CASMO-4 and WIMS-$D_4$ were employed. The CASMO-4 code was used to calculate cross sections for fuel assemblies. Since this code is not capable of performing 3×3 multi-assembly calculations, the WIMS-$D_4$ code was employed for cross section generation for non-fuel assemblies such as graphite reflector, control rod and additional absorber.

The neutron cross sections of fuel assemblies were calculated by CASMO-4. During cross section calculations it was assumed that all compositions of the critical facility remain at the constant temperature of 300K. The boundary between thermal and fast energy was defined as 4 eV. The "mirror" boundary conditions were used for single assembly calculations.

The fuel composition includes $U^{235}$, 2.0% in U, $U^{238}$, $U^{234}$ (0.02 w% of metallic uranium) and $U^{236}$ (0.1 w/% of metallic uranium). The fuel is assumed to be fresh and does not contain fission products, such as $Xe^{135}$ and $Sm^{149}$, since the facility is operated at cold zero power and only for short time periods.

The graphite used as moderator in the critical facility contains some isotopes having large absorption, e.g., natural cadmium ($15\times10^{-5}$ w/%) and boron ($15\times10^{-5}$ w%). The exact mass fractions for these additional isotopes are not available, but the range of their variations in concentration is provided in reference 19. Their mass fractions are 25 ± 3% of the maximum concentrations as suggested by measurements performed on a number of samples.

The neutron cross sections for non-fuel assemblies are calculated by employing the WIMS-$D_4$ code, since this code is capable of performing multi-assembly calculations. In the multi-assembly model, a non-fuel assembly is surrounded by eight fuel assemblies. The mirror boundary condition was employed again. This condition is sufficiently valid since the critical assembly consists of as many as 192 fuel assemblies. However, this is not a good assumption when the critical assembly consists of only 18-22 fuel assemblies. That is caused, probably, by the fact that, on average, the control rods are one graphite assembly away from fuel assemblies, as shown in Fig.4.8, 4.9 and 4.11. As a result, the actual neutron flux spectrum is more moderated (the neutron spectrum is shifted to the lower energy region) than it is in the multi-assembly geometry where a non-fuel assembly is surrounded by eight fuel assemblies.

So, the multi-assembly model was modified generate cross sections for non-fuel assemblies in the critical assembly consisting of 18-22 fuel assemblies. The modification consisted of increasing the amount of graphite between a non-fuel assembly and the outermost neutron source. In addition, the zero-flux boundary condition was employed in this case.

## 4.5 Critical Assembly Model and Data Comparison Formalism

As mentioned earlier, eight experiments have been analyzed with the ARROTTA code, and the calculated results are compared with the measured. Of these, five experiments (ECF) are analyzed with steady static calculations, and the other three experiments (EFC) are analyzed with time dependent calculations.

In the ARROTTA computational model of the critical facility, the whole core is divided into 18×18×21 rectangular nodes. One assembly stands for one node, and 21 nodes are used to represent the entire axial height. The first and last axial nodes are the top and bottom reflectors, respectively.

The zero-flux boundary condition is employed for all six boundaries of the critical facility. Since the power generated in the experiments is negligibly small, fuel and moderator temperature feedbacks are not taken into account. Six delayed neutron groups are used in this model.

The comparison of results involves three aspects. One aspect is devoted to the comparison of effective multiplication factor. Since the assembly is made critical by maneuvering control rods during the early stage of the experiments, the calculated effective multiplication factor is expected to be close to unity.

The second aspect is to deal with the comparison of neutron flux distribution between that calculated by ARROTTA and that measured in the experiments. During the ECF-type experiments, the relative neutron flux distributions are

derived from the measurements of the activity of the copper foils irradiated in the core.

For comparison, the activity of the copper foils is also calculated from the ARROTTA calculated 2 group flux distributions, since the activity of the copper foils is induced by both fast neutrons and thermal neutrons. Therefore, in order to calculate the activity of copper foils, a program, named FLAN, was developed. The FLAN program processes the three-dimensional two-energy neutron fluxes calculated by ARROTTA, to obtain the 2 group fluxes for the positions where copper foils are positioned in the experiments. The activity of the copper foils is determined by the relative absorption reaction rate in the copper foils, as shown in the equation below:

$$A_\alpha = \Phi_1 \cdot \sigma_{a_1} + \Phi_2 \cdot \sigma_{a_2} \qquad \text{Eq. 4.1}$$

where $A_a$ is the relative activity of the copper foil, and $\Phi_1$ and $\Phi_2$ are neutron fluxes in fast and thermal energy groups, respectively. $\sigma_{a1}$ and $\sigma_{a2}$ stand for copper integrated microscopic absorption cross sections in first and second energy groups, respectively. The cross sections of copper were calculated by CASMO-4. In this calculation, a few copper cells are arranged in the periphery of fuel cluster like fuel pin cells. According to these calculations, the copper two-group microscopic absorption cross sections are $\sigma_{a1}$=0.261238 and $\sigma_{a2}$=2.62935 barns, respectively. Finally, the calculated relative copper foil activities are normalized, and compared with the measured values.

Another program REAC was developed to compare the calculated results with the measured data from the EFC-type experiments. For EFC-type studies, only calculated thermal neutron fluxes are compared with the measured by fission chambers since fast neutrons produce very few fission reactions compared to those produced by the thermal neutrons. The REAC code reads the results produced by the ARROTTA code, calculating thermal neutron fluxes for the positions where fission chambers are placed in the experiments by averaging the thermal fluxes of four surrounding nodes. The averaged thermal fluxes are normalized, and compared to the normalized measured fluxes.

The third aspect is concerned with comparison of reactivity induced due to withdrawal or insertion of control rods. The reactivity calculation is based on the inverse point kinetics theory, taking advantage of the signals from different detectors, as shown in Eq.4.2 [17]:

$$\rho(t) = 1 + \frac{L}{\beta}\frac{d\ln T(t)}{dt} - \frac{1}{T(t)}\sum_{i=1}^{6}\frac{\beta_i}{\beta}e^{-\lambda_i t}\left(T_0 + \lambda_i\int_0^t T(t')e^{\lambda_i t'}dt'\right) \qquad \text{Eq. 4.2}$$

where $T(t)$ is the amplitude of the signal detected during the transient, and $T_0$ stands for the amplitude of the signal detected at the steady-state initial condition. $L/\beta$ is taken as 0.2 from the reference [18]. The decay constants $\lambda_i$ and effective delay neutron fractions $\beta_i$ are taken from the reference [12].

Similarly, the above equation is also implemented into the REAC program so as to calculate the reactivity using the results generated by ARROTTA. In this program, the terms $\boldsymbol{T(t)}$ and $\boldsymbol{T_0}$ are determined as follows:

$$T(t) = \frac{\Phi_D(t)}{\overline{\Phi}_C(0)} \qquad T_0 = \frac{\Phi_D(0)}{\overline{\Phi}_C(0)} \qquad \text{Eq. 4.3}$$

where $\Phi_D(t)$ is the calculated neutron flux for the location of detectors during the transients, $\Phi_D(0)$ stands for the neutron flux at steady state, and $\overline{\Phi}_C(0)$ is average core neutron flux calculated at steady state.

## 4.6 Analysis of the ECF-Type Experiments

### 4.6.1 Analysis of the ECF Experiment 1

The configuration of the first experiment is indicated in Fig.4.4 where there are 192 fuel assemblies. Twenty of them contain additional stainless steel spacers with the same amount of steel as in the upper RBMK-1500 fuel bundle. The fuel and additional absorber

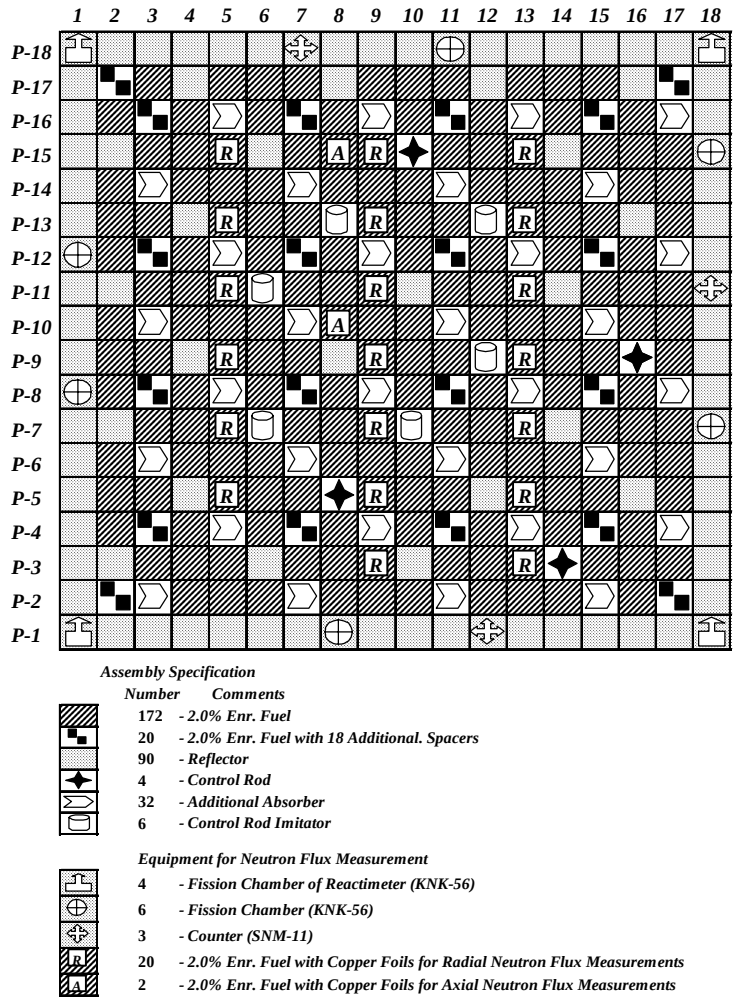


**Fig. 4.4** Configuration of ECF Experiment 1

channels are both filled with water at 300 K. The system pressure is 1 bar. This core also includes four control rods, three of which, namely, P15-10, P9-16 and P3-14, are fully inserted, and another of which, named as P5-8, is inserted 150 cm in the core.

Radial neutron fluxes were measured by irradiating copper foils and measuring their activities. The copper foils are placed 162 cm below the top of the active core as Fig.4.1 shows. The radial positions of copper foils are indicated in Fig.4.4. The results of comparison of the calculated results to the measured are presented in Table 4.1. The average discrepancy in copper activity is only 4.05%, and the maximum error is ≅8.3%.

| | | | | | | | | |
|---|---|---|---|---|---|---|---|---|
| | 75.7 | 53.8 | 64.3 | | 91.4 | 118.7 | 128.5 | - Measured |
| P-15 | 79.6 | 50.6 | 63.2 | P-7 | 95.4 | 117.0 | 127.1 | - Calculated |
| | 5.1% | -6.0% | -1.7% | | 4.4% | -1.4% | -1.1% | - Discrepancy |
| | 90.8 | 76.9 | 77.2 | | 104.9 | 133.0 | 123.1 | |
| P-13 | 95.9 | 75.1 | 73.6 | P-5 | 109.6 | 137.0 | 121.9 | |
| | 5.7% | -2.3% | -4.7% | | 4.5% | 3.0% | -1.0% | |
| | 87.3 | 139.0 | 112.2 | | | 90.9 | 59.2 | |
| P-11 | 89.1 | 136.7 | 109.1 | P-3 | | 98.4 | 59.3 | |
| | 2.0% | -1.6% | -2.8% | | | 8.3% | 0.2% | |
| | 116.5 | 153.0 | 103.1 | | 5 | 9 | 13 | |
| P-9 | 117.0 | 149.6 | 94.8 | | | | | |
| | 0.5% | -2.2% | -8.1% | | | | | |
| | 5 | 9 | 13 | | | | | |

**Table 4.1** Comparison of radial neutron flux distribution with measured, ECF Experiment 1

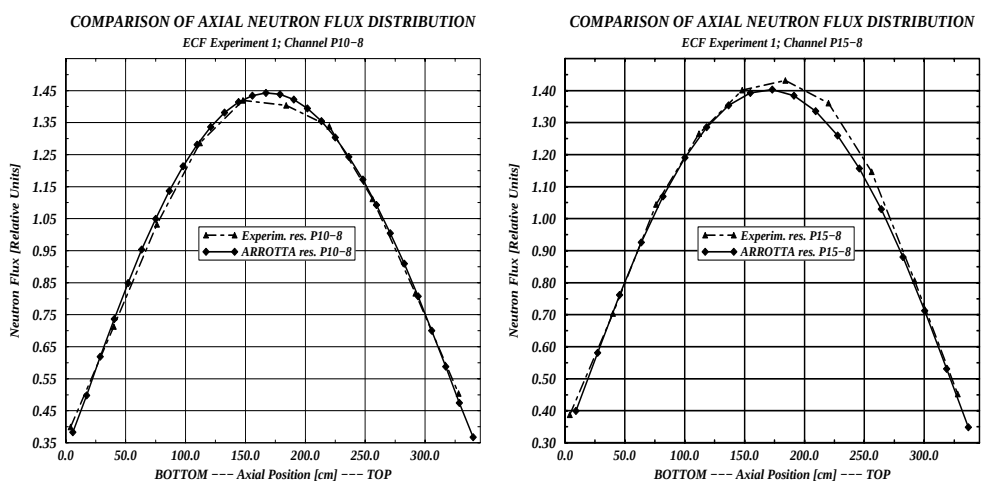


**Fig. 4.5** Comparison of axial neutron flux profiles, ECF Experiment 1. Channel P10-08 (left) and channel P15-08 (right)

The axial neutron flux distribution was measured in the channels P10-8 and P15-8 where the axial location of copper foils is indicated in Fig. 4.1. The axial neutron flux was also calculated by ARROTTA, and compared to the measured as shown in Fig. 4.5.

The effective multiplication factor calculated by modeling criticality conditions is 1.00410.

### 4.6.2 Analysis of the ECF Experiment 2

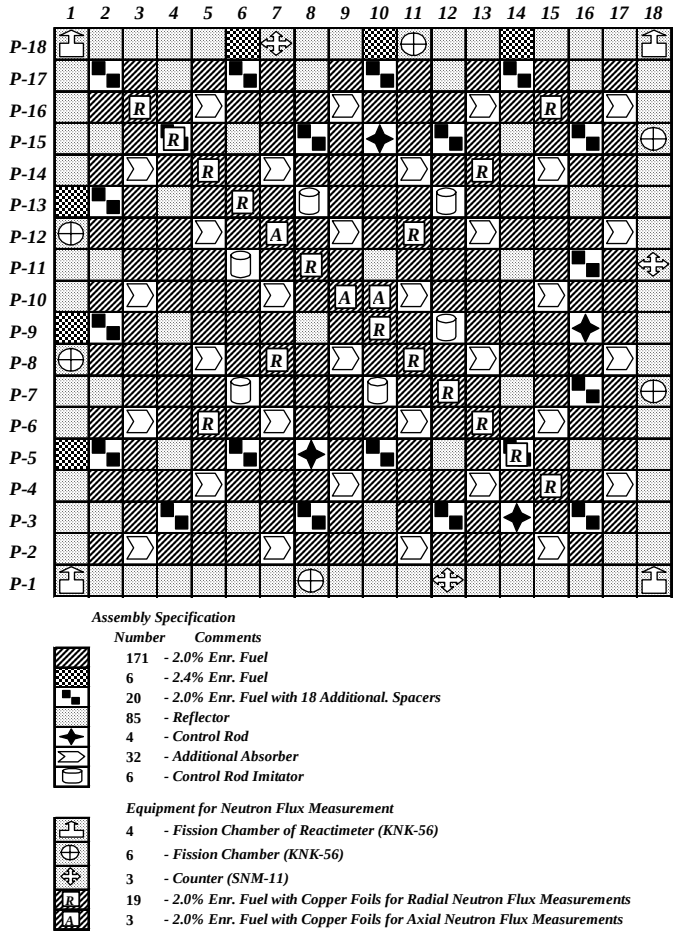


**Fig. 4.6** Configuration of ECF Experiment 2

Configuration of the second ECF experiment is shown in fig 4.6. This configuration includes 6 fuel assemblies 2.4% enrichment in addition to the 191 fuel assemblies of 2.0% enrichment. Fuel and additional absorber channels are filled with water.

| *Coordinate* | *Measured Flux (RU)* | *Calculated Flux (RU)* | *Discrep. [%]* | *Coordinate* | *Measured Flux (RU)* | *Calculated Flux (RU)* | *Discrep. [%]* |
|---|---|---|---|---|---|---|---|
| *P16-03* | 49.0 | *53.1* | *8.27%* | *P16-15* | 60.0 | *58.7* | *-2.16%* |
| *P15-04* | 79.0 | *82.7* | *4.68%* | *P06-05* | 73.0 | *78.3* | *7.23%* |
| *P14-05* | 105.0 | *109.9* | *4.67%* | *P08-07* | 111.0 | *111.1* | *0.12%* |
| *P13-06* | 104.0 | *103.7* | *-0.33%* | *P09-10* | 126.0 | *124.9* | *-0.87%* |
| *P12-07* | 102.0 | *97.6* | *-4.33%* | *P08-11* | 103.0 | *98.0* | *-4.84%* |
| *P11-08* | 127.0 | *125.0* | *-1.60%* | *P07-12* | 103.0 | *105.5* | *2.39%* |
| *P10-09* | 152.0 | *149.6* | *-1.56%* | *P06-13* | 106.0 | *113.3* | *6.89%* |
| *P10-10* | 139.0 | *139.5* | *0.37%* | *P05-14* | 80.0 | *85.7* | *7.15%* |
| *P12-11* | 129.0 | *118.8* | *-7.89%* | *P04-15* | 52.0 | *54.9* | *5.49%* |
| *P14-13* | 99.0 | *89.8* | *-9.29%* | | | | |

**Table 4.2** Comparison of calculated radial neutrino flux distribution with measured, ECF Experiment 2.

I.

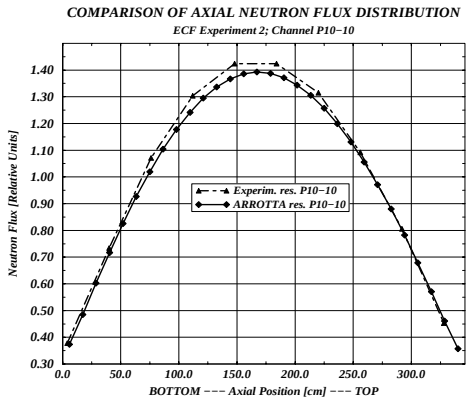


II.

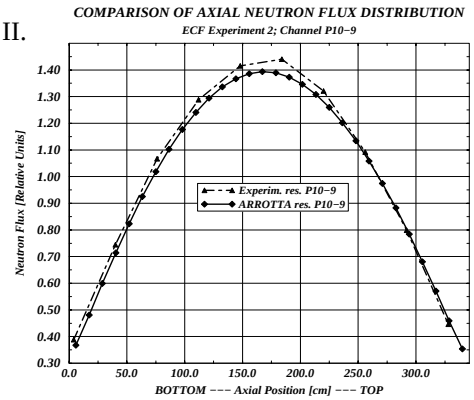


III.

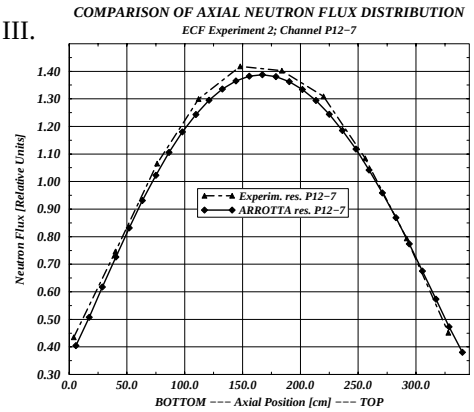


**Fig. 4.7** Comparison of axial neutron flux profiles; ECF Experiment 2, Channel P10-10 (I), P10-09 (II) and P12-07 (III)

The control rods P5-8, P9-16, and P3-14, are fully inserted, and P15-10 is inserted 205 cm according to position indicator.

The effective multiplication factor calculated by modeling criticality conditions is 1.00293.

The measurements of radial neutron flux were performed in 19 fuel channels (see Fig.4.6) at 162 cm below the top of active core. ARROTTA results are compared against measurements and presented in Table 4.2. The comparison indicates that average discrepancy is about 5.4% and maximum reaches 9.2%.

The axial neutron flux was measured in channels P10-9, P10-10, and P12-7. The measured results were normalized by the average neutron flux in the channel P12-7. The same was done with ARROTTA results and graphically compared in fig.4.7.

### 4.6.3 Analysis of the ECF Experiment 3

The third experiment contains only 14 fuel assemblies. The fuel has 2.4% enrichment and the fuel channels are filled with water. Other channels were dry.

The effective multiplication factor calculated by modeling criticality conditions is 1.00623.

Measurements of radial neutron flux were performed in all of the fourteen fuel channels at three axial positions, namely 90 cm, 162 cm and 270 cm from the top of active core. The neutron fluxes, averaged axially at three points, were normalized with respect to the average neutron flux in the core. The measurements of radial neutron flux were performed at critical core condition when control rods P6-7, P6-13, P12-7 and P12-13 were inserted 210 cm according to position indicator.

The same conditions were modeled by the ARROTTA code and results compared with measured data are shown in Table 4.3. The comparison of radial neutron flux showed that average discrepancy is 0.8% and maximum is only 2.5%.

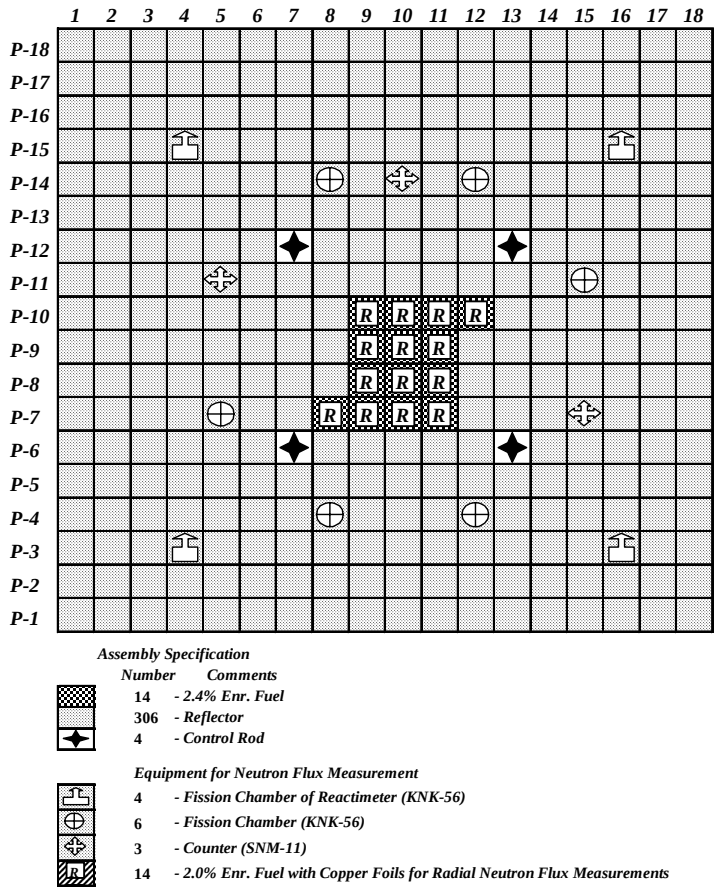


**Fig.4.8** Configuration of ECF Experiment 3

| | 8 | 9 | 10 | 11 | 12 | |
|---|---|---|---|---|---|---|
| P-10 | | 88.0 | 102.0 | 95.0 | 71.0 | - Measured |
| | | 89.6 | 102.0 | 93.5 | 70.8 | - Calculated |
| | | 1.8% | 0.0% | -1.6% | -0.3% | - Discrepancy |
| P-9 | | 111.0 | 126.0 | 113.0 | | |
| | | 110.4 | 124.7 | 112.6 | | |
| | | -0.5% | -1.0% | -0.3% | | |
| P-8 | | 112.0 | 124.0 | 110.0 | | |
| | | 111.9 | 124.3 | 110.2 | | |
| | | -0.1% | 0.2% | 0.1% | | |
| P-7 | 70.0 | 91.0 | 100.0 | 87.0 | | |
| | 68.2 | 92.1 | 101.0 | 88.6 | | |
| | -2.5% | 1.2% | 1.0% | 1.8% | | |

**Table 4.3** Comparison of radial neutron flux distribution with measured, ECF Experiment 3

### 4.6.4 Analysis of the ECF Experiment 4

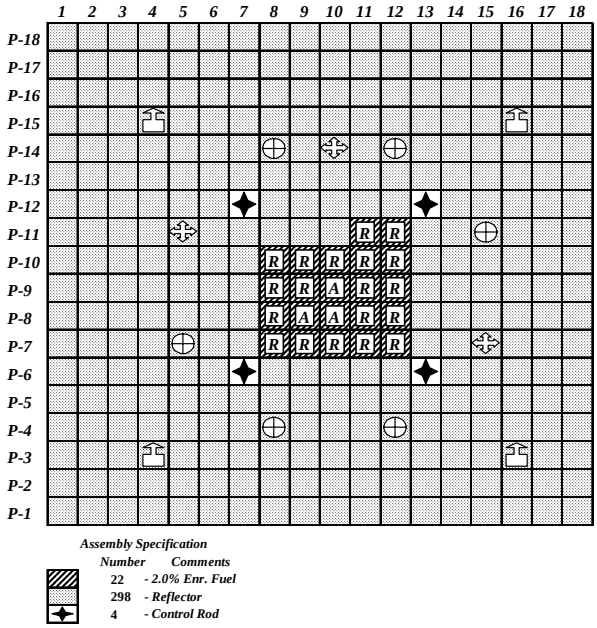


**Fig.4.9** Configuration of ECF Experiment 4

| | | | | | |
|---|---|---|---|---|---|
| | | | Measured - | 87.0 | 73.0 |
| P-11 | | | Calculated - | 86.5 | 71.2 |
| | | | Discrepancy - | -0.6% | -2.4% |
| | 83.0 | 103.0 | 114.0 | 106.0 | 91.0 |
| P-10 | 83.9 | 104.0 | 114.4 | 106.9 | 90.5 |
| | 1.0% | 1.0% | 0.4% | 0.8% | -0.6% |
| | 95.0 | 113.0 | 125.0 | 118.0 | 101.0 |
| P-9 | 93.8 | 114.7 | 125.7 | 119.2 | 100.7 |
| | -1.2% | 1.5% | 0.5% | 1.0% | -0.3% |
| | 92.0 | 112.0 | 120.0 | 113.0 | 97.0 |
| P-8 | 91.6 | 111.7 | 121.6 | 114.4 | 95.9 |
| | -0.5% | -0.3% | 1.4% | 1.3% | -1.1% |
| | 80.0 | 96.0 | 104.0 | 98.0 | 82.0 |
| P-7 | 77.3 | 95.5 | 103.8 | 97.1 | 79.8 |
| | -3.4% | -0.6% | -0.2% | -0.9% | -2.7% |
| | 8 | 9 | 10 | 11 | 12 |

**Table 4.4** Comparison of radial neutron flux distribution with measured, ECF Experiment 4

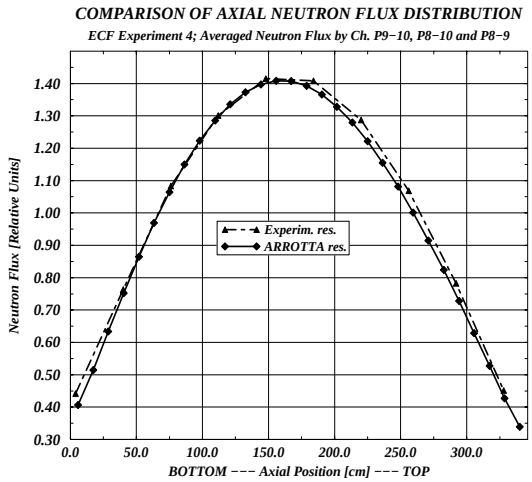


**Fig. 4.10** Comparison of axial neutron flux profiles, ECF Experiment 4. Neutron flux profile is averaged by channel P09-10, P08-10 and P08-09

The configuration of fourth critical assembly is shown in Fig. 4.9. There are 22 dry fuel bundles enriched to 2.0%. Criticality was achieved by inserting control rods P6-7 and P6-13 185cm, and P12-7 and P12-13 180cm according to position indicator.

The effective multiplication factor calculated by modeling criticality conditions is 1.00478.

The radial neutron flux was measured at three axial planes, namely 90, 162 and 270cm below the top of the active core. The neutron fluxes were averaged at three axial points and normalized with respect to the average radial neutron flux. The ARROTTA code was used to model the same conditions and results processed in the same way as were the measured. They are compared in Table 4.4. The comparison indicates that average radial neutron flux discrepancy is about 1% and maximum error is 3.4%.

The measurements of axial neutron flux also were conducted. Before measurements, positions of control rods were changed and all four were inserted 185cm according to position indicator. The copper foils were placed in the channels P9-10, P8-10 and P8-9. The measured axial neutron flux was averaged between these three channels and normalized. ARROTTA results are averaged and normalized in the same way and the graphical comparison is shown in fig 4.10.

### 4.6.5 Analysis of the ECF Experiment 5

The last experiment included 18 fuel bundles enriched to 2.0%. The configuration of this critical assembly is shown in fig.4.11. The fuel channels are filled with water. The control rod and reflector channels are dry. The criticality was reached at following positions of control rods: P6-7 was inserted 235cm, P6-13 and P12-13 were inserted 240cm, and P12-7 was positioned 230cm according to the position indicator.

The effective multiplication factor calculated by modeling criticality conditions is 1.00019.

The radial neutron flux was measured in the same way as in the ECF-4 critical assembly. The copper foils were placed in 18 channels at three axial positions, namely 90, 162 and 270cm below the top of active core. The averaged values at three axial points were also normalized by the average neutron flux. The ARROTTA code results were averaged and normalized as well and are shown in Table 4.6. The analysis indicates that average radial discrepancy is 1.6% and the maximum error is ≅4.2%.

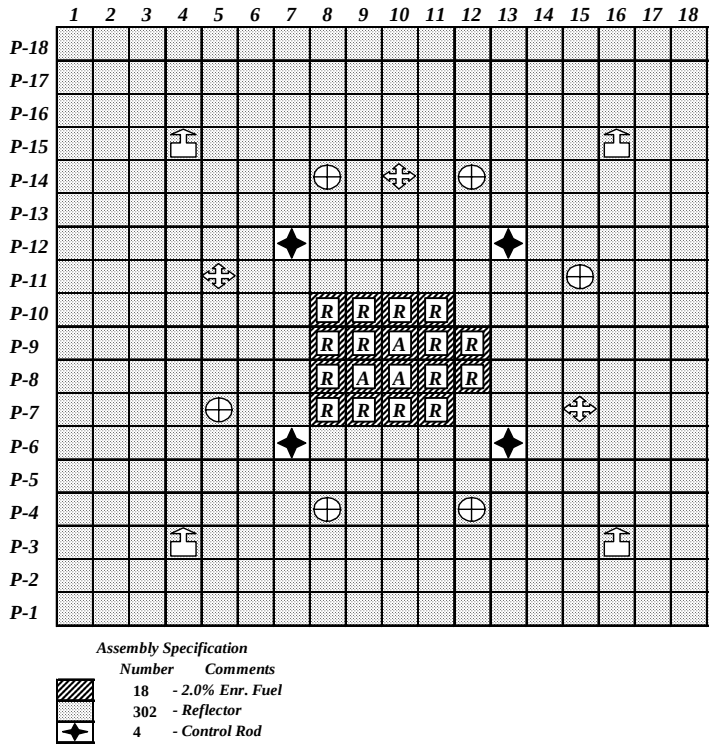


**Fig.4.11** Configuration of ECF Experiment 5

| | | | | | |
|---|---|---|---|---|---|
| | 80.0 | 100.0 | 104.0 | 92.0 | - Measured |
| *P-10* | *77.5* | *97.9* | *103.3* | *91.6* | *- Calculated* |
| | *-3.1%* | *-2.1%* | *-0.7%* | *-0.5%* | *- Discrepancy* |
| | 95.0 | 123.0 | 129.0 | 112.0 | 82.0 |
| *P-9* | *94.2* | *120.0* | *127.1* | *111.8* | *83.2* |
| | *-0.8%* | *-2.5%* | *-1.5%* | *-0.2%* | *1.5%* |
| | 93.0 | 121.0 | 127.0 | 111.0 | 79.0 |
| *P-8* | *93.0* | *119.2* | *126.5* | *111.2* | *82.3* |
| | *0.0%* | *-1.5%* | *-0.4%* | *0.1%* | *4.2%* |
| | 74.0 | 90.0 | 98.0 | 90.0 | |
| *P-7* | *73.7* | *95.8* | *101.8* | *89.9* | |
| | *-0.4%* | *6.5%* | *3.9%* | *-0.1%* | |
| | *8* | *9* | *10* | *11* | *12* |

**Table 4.5** Comparison of radial neutron flux distribution with measured, ECF Experiment 5

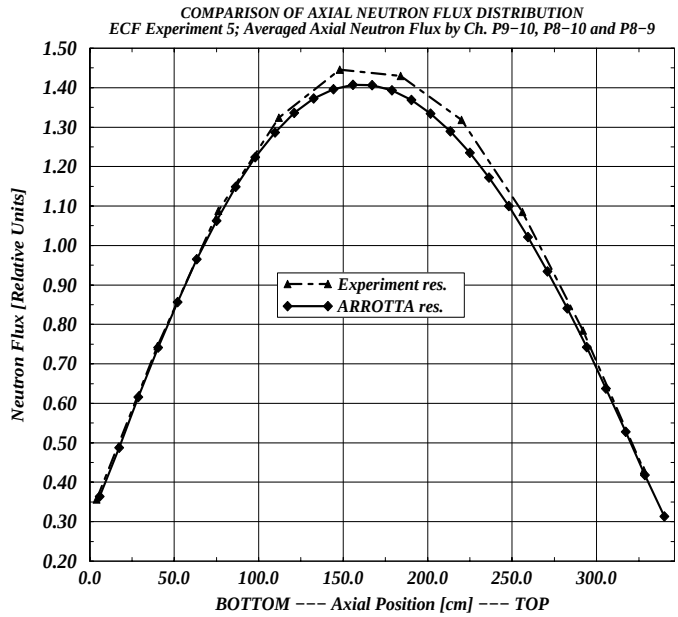


**Fig. 4.12** Comparison of axial neutron flux profiles, ECF Experiment 5. Considering channel P09-10, P08-10 and P08-09 the neutron flux profile was averaged

The axial neutron flux measurements were performed in the fuel channels located at P9-10, P8-10 and P8-9. Before the measurements, all control rods were inserted 215cm according to the position indicator. The results were also averaged by three channels and normalized. The comparison of the calculated axial neutron flux against the measured one is presented in fig.4.12.

## 4.7 Analysis of the EFC Type Experiments

The last three experiments considered were performed in the configuration of the critical facility shown in fig.4.13. This core consists of 192 fuel assemblies with 2.0% enrichment, 172 of which do not contain additional spacers, but 20 of which do. The core also contains 32 additional absorbers and six control rod imitators. In this configuration, there are 22 control rods, named AZ, KO and MR. However, only MR and KO are activated during the experiments. So, only 15 control rods were moved, and 7 AZ rods were maintained at the fully withdrawn positions. The AZ channels function as graphite blocks with aluminum tubes.

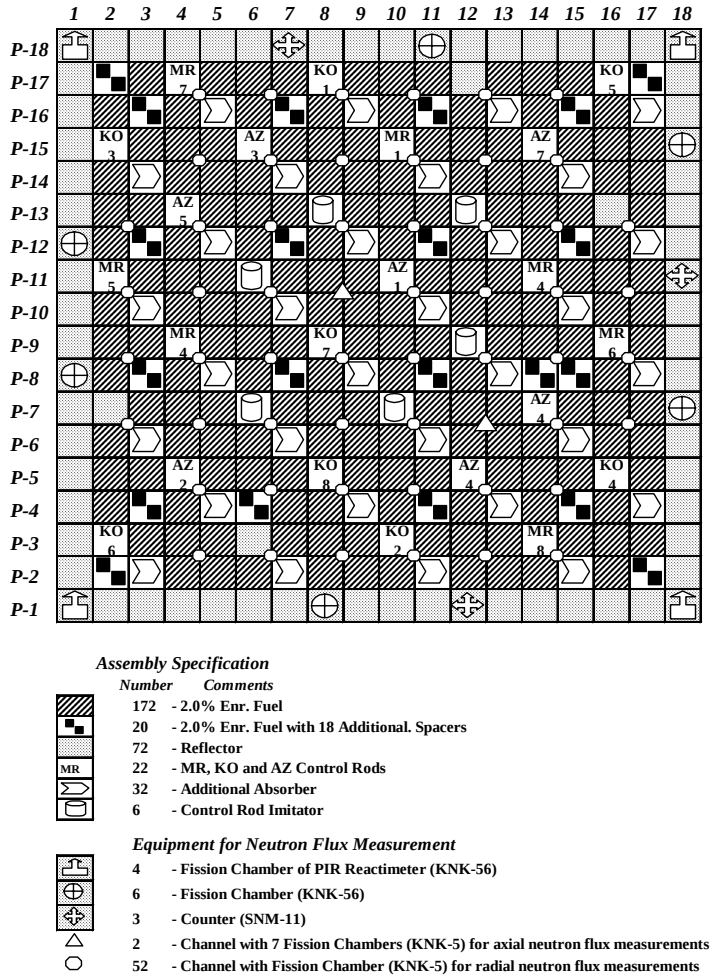


**Fig.4.13** Critical Facility Configuration that is employed during EFC type experiments

The channels containing fuel assemblies and additional absorbers are filled with water. The other channels are dry.

The neutron flux was measured by employing KNK-5 fission chambers, and these experiments are distinguished as Experiments with Fission Chambers (EFC). The chambers were located in the vertexes of graphite blocks in the special openings. Two chains of seven chambers were used for measuring axial flux distributions, and 54 chambers were located in the mid-plane of the core for measuring the radial power distributions as seen in Figs. 4.1 and 4.13.

The reactivity was determined by employing a reactimeter, which uses sum of the signals from four KNK-56 ionization chambers. The KNK-56 detectors are located in the corners of the critical facility as shown in Fig.4.13. Axially, they were fixed in the mid-plane of the core. For some cases, the reactivity was determined by sum of signals from all 68 KNK-5 fission chambers.

| Experiment | Number of activated rods during experiment | List of activated rods | Control rod transient | Fully inserted control rods at critical CF condition | Fully withdrawn control rods at critical CF condition | Partially inserted control rods at critical CF condition [cm] |
|---|---|---|---|---|---|---|
| EFC-1 | 4 | KO-3, MR-4, MR-5, MR-7 | Rod Drop | MR-1,6,8 | MR-3,4,5,7<br>KO-1,2,3,4,5,6,7 | KO-8 (195) |
| EFC-2 | 1 | KO-8 | Withdraw | MR-1,6,8<br>KO-4 | MR-3,4,5,7<br>KO-1,2,3,5,6,7 | KO-8 (155) |
| EFC-3 | 15 | MR-1,3,4,5,6,7,8<br>KO-1,2,3,4,5,6,7,8 | Rod Drop | - | KO-7, MR-1 | MR-4,5,6,7,8 (200)<br>KO-1,2,3,4,5,6,8 (200)<br>MR-3 (175) |

**Table 4.6** Initial position of control rods and scenarios of transients during the EFC type experiments

The EFC-type experiments incorporate three transients induced by control rod movements. The general description is presented in Table 4.6. The first experiment, named EFC-1, deals with dropping of four control rods with a velocity of 180 cm/sec. The radial and axial neutron fluxes were also measured at critical core conditions at 3 and 15 seconds after initiation of control rod drop. The axial positions of control rods at critical core conditions are given in three last columns of Table 4.6.

In the second experiment, during the first 18 seconds, the KO-8 control rod, with an initial depth of 155 cm, was continuously withdrawn at a velocity of 8.5 cm/sec; then, all KO and MR control rods were dropped at a velocity of 180 cm/sec. The neutron fluxes were also measured at critical conditions, at 21 and 33 sec after initiation of the withdrawal of KO-8.

Generally, the scenario of the third EFC experiment is similar to that of the first one, but there is a difference in that before the rod drop event 13 control rods were inserted to half depth of the core. All 15 control rods were dropped during the experiment. The drop velocity was also 180 cm/sec. The neutron flux measurements were also performed at critical core conditions, at 3 and 15 sec after initiation of the transient.

### 4.7.1 Analysis of the EFC Experiment 1

The first EFC experiment deals with dropping of four control rods. Simulation of this experiment is performed by the ARROTTA code and comparisons of radial and axial neutron fluxes are made. The calculated and measured results are shown in Tables 4.7, 4.8, 4.9 and Figs. 4.14, 4.15, and 4.16.

CRITICAL CONDITION TIME=0 SEC

| | 2 | 4 | 6 | 8 | 10 | 12 | 14 | 16 |
|---|---|---|---|---|---|---|---|---|
| 16 | | 52<br>56<br>7.6% | 62<br>62<br>0.2% | 50<br>50<br>-0.6% | 42<br>40<br>-3.6% | 46<br>47<br>3.3% | 46<br>47<br>3.0% | |
| 14 | | 98<br>101<br>2.8% | 104<br>101<br>-3.3% | 81<br>75<br>-7.6% | 62<br>63<br>1.2% | 82<br>78<br>-4.6% | 83<br>84<br>1.3% | |
| 12 | 79<br>79<br>-0.4% | 117<br>116<br>-0.5% | 113<br>105<br>-7.1% | 94<br>100<br>6.5% | 126<br>118<br>-6.0% | 89<br>96<br>7.7% | 110<br>108<br>-1.6% | 68<br>67<br>-1.9% |
| 10 | 82<br>83<br>1.1% | 122<br>120<br>-1.7% | 109<br>117<br>7.3% | 168<br>169<br>0.5% | 175<br>163<br>-6.9% | 136<br>131<br>-3.5% | 124<br>119<br>-3.8% | 58<br>57<br>-1.4% |
| 8 | 88<br>87<br>-0.8% | 135<br>132<br>-1.9% | 152<br>147<br>-3.0% | 170<br>174<br>2.5% | 145<br>139<br>-4.3% | 105<br>114<br>8.5% | 120<br>113<br>-5.6% | 44<br>47<br>7.6% |
| 6 | 76<br>79<br>4.0% | 117<br>115<br>-1.5% | 102<br>114<br>11.5% | 148<br>142<br>-3.9% | 111<br>122<br>9.6% | 149<br>153<br>2.9% | 133<br>130<br>-1.9% | 63<br>66<br>4.2% |
| 4 | | 107<br>110<br>2.7% | 121<br>126<br>4.3% | 124<br>136<br>9.4% | 145<br>143<br>-1.0% | 144<br>137<br>-4.5% | 98<br>95<br>-3.4% | |
| 2 | | 61<br>64<br>5.0% | 84<br>82<br>-1.9% | 86<br>86<br>-0.2% | 90<br>90<br>0.5% | 69<br>65<br>-5.3% | 32<br>35<br>10.5% | - Measured<br>- Calculated<br>- Discrepancy |

**Table 4.7** Comparison of radial neutron flux distribution with measured, EFC Experiment 1. Critical Condition *T=0* sec

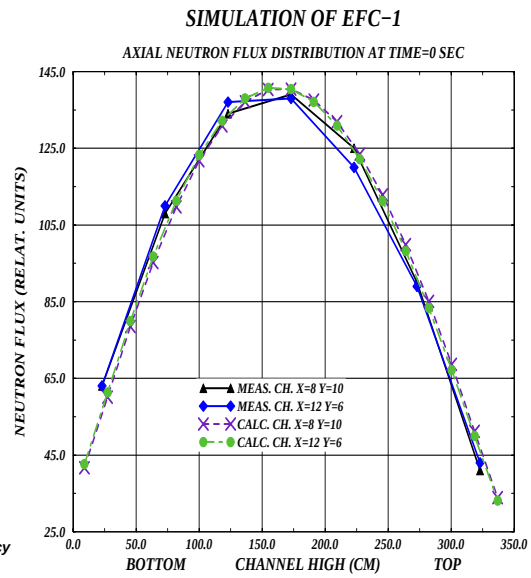


**Fig. 4.14** Comparison of axial neutron flux profiles with measured, EFC Experiment 1. Critical Condition *T=0* sec

The effective multiplication factor calculated by modeling criticality conditions is 1.0029.

The Table 4.7 and Fig. 4.14 show comparisons of calculated and measured neutron flux distribution at critical core condition. It was estimated that calculated neutron flux discrepancy with respect to the measured is 3.9% and this discrepancy increases to 5.5% at third second of transient (Table 4.8 and Fig.4.15).

*TIME=3 SEC*

| | 2 | 4 | 6 | 8 | 10 | 12 | 14 | 16 |
|---|---|---|---|---|---|---|---|---|
| 16 | | 29<br>29<br>1.3% | 53<br>49<br>-7.4% | 48<br>46<br>-5.1% | 45<br>44<br>-2.9% | 53<br>55<br>4.0% | 56<br>57<br>1.6% | |
| 14 | | 75<br>68<br>-9.2% | 89<br>81<br>-9.2% | 78<br>71<br>-8.6% | 69<br>68<br>-1.3% | 97<br>91<br>-5.8% | 103<br>101<br>-1.9% | |
| 12 | 45<br>41<br>-9.6% | 86<br>77<br>-10.3% | 104<br>88<br>-15.6% | 94<br>100<br>6.5% | 141<br>129<br>-8.3% | 106<br>112<br>5.2% | 131<br>130<br>-0.6% | 80<br>81<br>1.5% |
| 10 | 34<br>32<br>-6.2% | 77<br>68<br>-11.9% | 96<br>100<br>3.7% | 171<br>171<br>0.2% | 190<br>178<br>-6.3% | 155<br>153<br>-1.3% | 144<br>144<br>-0.3% | 69<br>70<br>1.0% |
| 8 | 44<br>42<br>-4.7% | 66<br>68<br>2.3% | 134<br>129<br>-4.1% | 175<br>177<br>1.3% | 160<br>154<br>-3.9% | 118<br>135<br>14.1% | 138<br>137<br>-0.4% | 53<br>58<br>9.6% |
| 6 | 54<br>55<br>2.7% | 95<br>91<br>-3.7% | 99<br>109<br>10.0% | 156<br>151<br>-3.5% | 122<br>139<br>14.2% | 174<br>184<br>5.5% | 155<br>159<br>2.7% | 74<br>81<br>9.6% |
| 4 | | 95<br>102<br>6.9% | 120<br>128<br>6.9% | 137<br>149<br>8.5% | 167<br>167<br>-0.2% | 170<br>165<br>-3.0% | 118<br>116<br>-1.7% | |
| 2 | | 59<br>63<br>6.7% | 81<br>86<br>6.3% | 92<br>96<br>3.9% | 103<br>105<br>2.3% | 85<br>78<br>-7.9% | 37<br>43<br>17.2% | |

- Measured
- Calculated
- Discrepancy

**Table 4.8** Comparison of radial neutron flux distribution with measured, EFC Experiment 1. Transient *T=3* sec

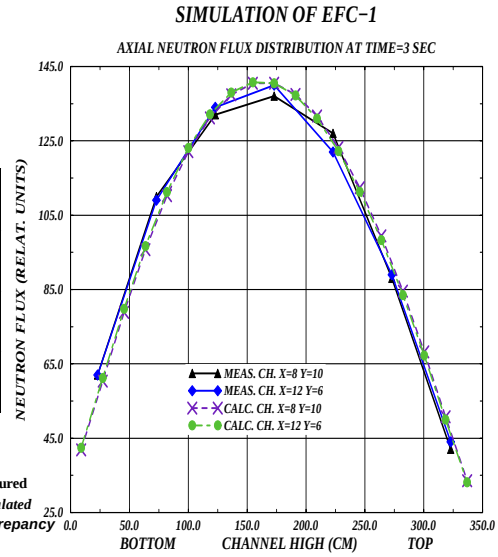


**Fig. 4.15** Comparison of axial neutron flux profiles with measured, EFC Experiment 1. Transient *T=3* sec

*TIME=15 SEC*

| | 2 | 4 | 6 | 8 | 10 | 12 | 14 | 16 |
|---|---|---|---|---|---|---|---|---|
| 16 | | 28<br>28<br>1.0% | 54<br>48<br>-11.6% | 48<br>45<br>-6.6% | 45<br>44<br>-2.8% | 52<br>56<br>7.0% | 55<br>58<br>4.9% | |
| 14 | | 72<br>66<br>-8.9% | 84<br>79<br>-6.3% | 76<br>70<br>-7.3% | 71<br>68<br>-3.9% | 94<br>92<br>-1.8% | 103<br>102<br>-0.5% | |
| 12 | 44<br>39<br>-11.7% | 82<br>74<br>-9.2% | 96<br>86<br>-10.4% | 96<br>99<br>3.6% | 141<br>130<br>-8.1% | 105<br>113<br>7.2% | 130<br>132<br>1.5% | 80<br>82<br>3.0% |
| 10 | 30<br>31<br>1.9% | 76<br>66<br>-13.5% | 92<br>98<br>6.8% | 169<br>171<br>1.0% | 194<br>178<br>-8.0% | 159<br>155<br>-2.8% | 145<br>146<br>0.4% | 69<br>71<br>2.6% |
| 8 | 46<br>40<br>-12.0% | 67<br>66<br>-1.5% | 136<br>127<br>-6.5% | 173<br>177<br>2.2% | 159<br>154<br>-2.9% | 120<br>136<br>13.4% | 142<br>139<br>-1.8% | 55<br>59<br>7.3% |
| 6 | 55<br>54<br>-1.6% | 94<br>90<br>-4.4% | 103<br>108<br>5.0% | 158<br>150<br>-4.8% | 131<br>140<br>7.1% | 172<br>186<br>8.0% | 157<br>162<br>2.9% | 82<br>82<br>0.5% |
| 4 | | 98<br>100<br>2.3% | 123<br>128<br>3.8% | 135<br>149<br>10.2% | 159<br>168<br>5.6% | 165<br>167<br>1.1% | 117<br>118<br>0.7% | |
| 2 | | 59<br>62<br>5.6% | 86<br>86<br>-0.3% | 94<br>96<br>1.9% | 99<br>106<br>7.3% | 82<br>79<br>-3.4% | 41<br>44<br>7.4% | |

- Measured
- Calculated
- Discrepancy

**Table 4.9** Comparison of radial neutron flux distribution with measured, EFC Experiment 1; Transient *T=15* sec

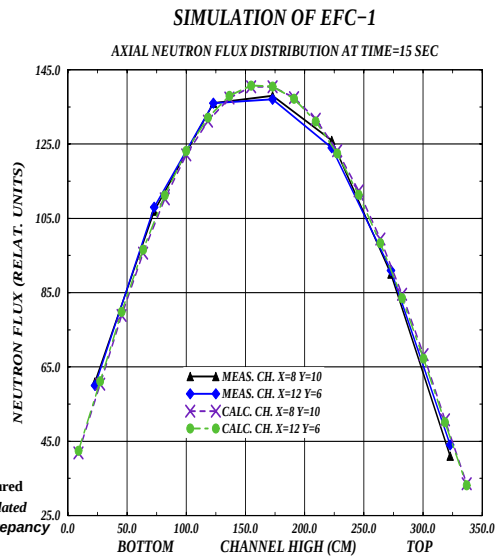


**Fig. 4.16** Comparison of axial nuetron flux profiles with measured, EFC Experiment 1; Transient T=15 sec

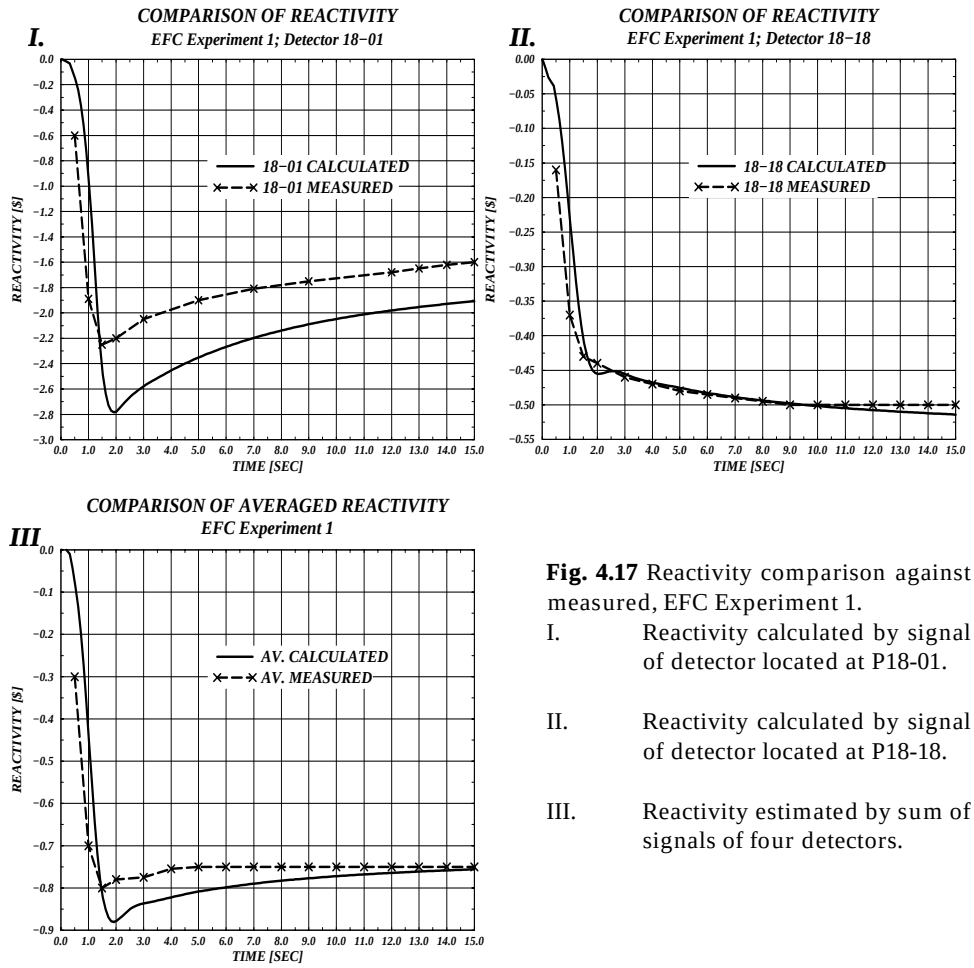


**Fig. 4.17** Reactivity comparison against measured, EFC Experiment 1.

I. Reactivity calculated by signal of detector located at P18-01.

II. Reactivity calculated by signal of detector located at P18-18.

III. Reactivity estimated by sum of signals of four detectors.

15 seconds later, the calculated average discrepancy was 5.1% and comparisons for separate channels are shown in Table 4.9 and Fig. 4.16.

The reactivity was estimated by sum of signals from KNK-56 ionization chambers during the EFC-1 experiment. In addition, the reactivity variations calculated using signals from different chambers was recorded and presented [18] for the comparison against ARROTTA result. However, the ARROTTA code is not equipped with models for transient reactivity calculations. Therefore, signal conversion to the reactivity was modeled by employing REAC code. The REAC uses neutron flux calculated by the ARROTTA code during the control rod transient and estimates reactivity by employing Inverse Point Kinetics theory.

The comparison of calculated and measured reactivity is presented in Fig.4.17. Fig.4.17-I and II show the reactivity comparison for two separate chambers located

in P18-01 and P18-18 channels (see Fig.4.13). The figure indicates good agreement between calculated and measured reactivity in the location of chamber P18-18. The discrepancy is larger for detector P18-01. The reactivity calculated by sum of signals is close to measured as shown in Fig.4.17-III. This figure indicates that the measured reactivity is –0.76$\beta$ while the calculated one is about –0.78$\beta$.

It should be noted that accuracy of reactivity calculation depends strongly on the number and position of detectors in the core. As indicated in Fig. 4.17-I and II, reactivity differs in amplitude and shape for different chambers by analyzing signals from individual chambers. Sum of signals at least from four chambers should be used for the reactivity estimation during a transient.

### 4.7.2 Analysis of the EFC Experiment 2

The second EFC experiment first measured the neutron flux in the critical facility at critical conditions. Comparisons of the calculated and measured neutron flux distributions are shown in Table 4.10 and Fig. 4.18. The average radial neutron flux distribution discrepancy is 4.1% at critical conditions.

The effective multiplication factor calculated by modeling criticality conditions is 1.00306.

Withdrawing of KO-8 control rod at 8.5cm/sec velocity followed the measurements at critical conditions. Eighteen seconds later, 15 control rods were dropped at the velocity of 180cm/sec. The neutron flux measured at 21 and 33 sec from the beginning of the KO-8 transient. The comparisons of calculated radial and axial neutron fluxes at 21 sec are shown in Table 4.11 and Fig. 4.19, and those at 33 sec in Table 4.12 and Fig. 4.20. Analysis of last two tables indicates that average discrepancy increases to 7.3 and 11.5% at 21 and 33 second, respectively.

The reactivity induced by movement of control rods was estimated by sum of signals from 68 KNK-5 fission chambers. The modeling of reactimeter by the REAC code also includes sum of 68 signals calculated by ARROTTA at the positions of the detectors. The comparison of the calculated reactivity against the measured one is shown in Fig.4.21. The measured reactivity caused by KO-8 withdrawal is +0.25$\beta$ [18] and that agrees perfectly with the calculated value. However, the calculated reactivity is more negative (–4.75$\beta$) than the measured (–4.30$\beta$), when all 15 control rods are dropped.

CRITICAL CONDITION TIME=0 SEC

| | 2 | 4 | 6 | 8 | 10 | 12 | 14 | 16 |
|---|---|---|---|---|---|---|---|---|
| 16 | | 53<br>57<br>7.0% | 63<br>63<br>-0.5% | 51<br>50<br>-2.5% | 41<br>40<br>-3.1% | 45<br>46<br>2.0% | 45<br>45<br>0.8% | |
| 14 | | 100<br>102<br>2.4% | 106<br>102<br>-4.0% | 81<br>75<br>-7.5% | 61<br>62<br>1.2% | 80<br>75<br>-5.7% | 79<br>80<br>1.5% | |
| 12 | 81<br>81<br>-0.2% | 121<br>119<br>-1.5% | 115<br>107<br>-7.2% | 93<br>100<br>8.0% | 125<br>117<br>-6.5% | 86<br>92<br>7.1% | 105<br>102<br>-2.6% | 63<br>63<br>-0.6% |
| 10 | 86<br>86<br>0.2% | 127<br>125<br>-1.9% | 112<br>120<br>7.5% | 171<br>171<br>0.0% | 174<br>161<br>-7.3% | 130<br>125<br>-3.8% | 117<br>111<br>-5.3% | 54<br>52<br>-3.1% |
| 8 | 94<br>92<br>-1.8% | 142<br>140<br>-1.5% | 159<br>155<br>-2.5% | 174<br>180<br>3.6% | 143<br>138<br>-3.7% | 99<br>106<br>7.0% | 104<br>99<br>-4.4% | 37<br>39<br>5.3% |
| 6 | 82<br>85<br>3.9% | 128<br>126<br>-1.9% | 111<br>127<br>14.1% | 161<br>158<br>-2.0% | 112<br>123<br>9.5% | 137<br>140<br>2.0% | 113<br>106<br>-6.5% | 43<br>42<br>-1.8% |
| 4 | | 119<br>123<br>3.0% | 138<br>147<br>6.8% | 143<br>161<br>12.5% | 149<br>147<br>-1.2% | 134<br>126<br>-5.7% | 75<br>68<br>-8.9% | |
| 2 | | 69<br>72<br>4.2% | 94<br>94<br>0.3% | 95<br>96<br>0.9% | 93<br>93<br>0.3% | 65<br>61<br>-5.6% | 25<br>26<br>6.0% | - Measured<br>- Calculated<br>- Discrepancy |

**Table 4.10** Comparison of radial neutron flux distribution with measured, EFC Experiment 2. Critical Condition *T=0* sec

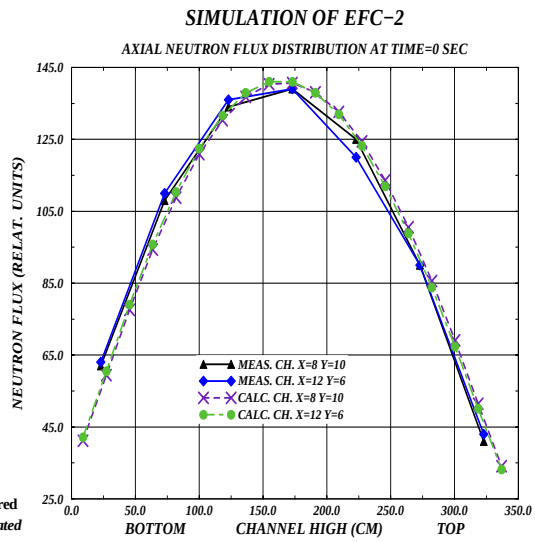


**Fig. 4.18** Comparison of axial neutron flux profiles with measured, EFC Experiment 2. Critical Condition *T=0* sec

TIME=21 SEC

| | 2 | 4 | 6 | 8 | 10 | 12 | 14 | 16 |
|---|---|---|---|---|---|---|---|---|
| 16 | | 46<br>48<br>4.2% | 65<br>66<br>1.6% | 42<br>46<br>9.4% | 56<br>51<br>-8.5% | 56<br>61<br>8.6% | 59<br>54<br>-9.0% | |
| 14 | | 111<br>113<br>1.7% | 130<br>120<br>-7.5% | 98<br>93<br>-5.4% | 84<br>80<br>-4.6% | 104<br>97<br>-7.1% | 104<br>97<br>-6.8% | |
| 12 | 84<br>71<br>-16.0% | 129<br>124<br>-3.7% | 132<br>121<br>-8.4% | 100<br>117<br>16.9% | 159<br>142<br>-10.7% | 102<br>102<br>0.4% | 106<br>100<br>-5.7% | 73<br>68<br>-7.4% |
| 10 | 56<br>52<br>-6.4% | 106<br>98<br>-7.8% | 104<br>106<br>2.1% | 167<br>159<br>-4.6% | 192<br>179<br>-6.7% | 140<br>129<br>-7.5% | 82<br>86<br>5.1% | 58<br>55<br>-4.9% |
| 8 | 63<br>65<br>3.6% | 86<br>88<br>2.3% | 129<br>116<br>-10.0% | 106<br>123<br>15.9% | 163<br>150<br>-8.1% | 117<br>130<br>11.3% | 129<br>125<br>-3.2% | 48<br>51<br>6.2% |
| 6 | 75<br>80<br>6.9% | 115<br>120<br>4.6% | 94<br>108<br>15.2% | 136<br>127<br>-6.3% | 111<br>134<br>21.1% | 173<br>184<br>6.5% | 148<br>148<br>0.0% | 61<br>61<br>0.8% |
| 4 | | 117<br>127<br>8.9% | 125<br>126<br>1.1% | 82<br>102<br>24.0% | 148<br>140<br>-5.6% | 157<br>156<br>-0.3% | 100<br>97<br>-2.9% | |
| 2 | | 67<br>76<br>14.1% | 90<br>90<br>0.0% | 69<br>72<br>3.9% | 54<br>60<br>12.0% | 61<br>69<br>12.6% | 33<br>36<br>10.5% | - Measured<br>- Calculated<br>- Discrepancy |

**Table 4.11** Comparison of radial neutron flux distribution with measured, EFC Experiment 2. Transient of control rods *T=21* sec

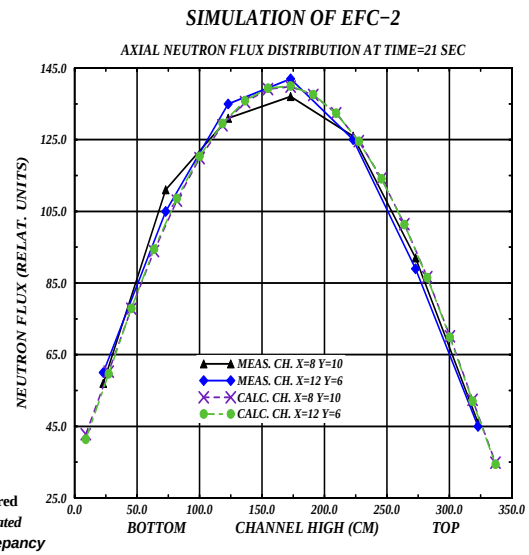


**Fig. 4.19** Comparison of axial neutron flux profiles with measured, EFC Experiment 2. Transient of control rods *T=21* sec

TIME=33 SEC

| | | | | | | | | |
|---|---|---|---|---|---|---|---|---|
| 16 | | 43<br>48<br>12.6% | 74<br>67<br>-9.6% | 49<br>47<br>-4.7% | 55<br>52<br>-4.7% | 61<br>62<br>2.2% | 68<br>55<br>-19.1% | |
| 14 | | 104<br>114<br>9.4% | 123<br>122<br>-1.2% | 104<br>94<br>-9.6% | 92<br>82<br>-11.3% | 111<br>99<br>-11.0% | 80<br>99<br>24.0% | |
| 12 | 92<br>71<br>-23.3% | 135<br>125<br>-7.7% | 135<br>122<br>-9.9% | 74<br>118<br>59.2% | 154<br>144<br>-6.7% | 104<br>104<br>-0.1% | 98<br>102<br>3.8% | 74<br>69<br>-6.9% |
| 10 | 68<br>52<br>-23.7% | 111<br>97<br>-12.7% | 98<br>106<br>7.8% | 166<br>160<br>-3.9% | 215<br>180<br>-16.2% | 147<br>131<br>-11.0% | 80<br>87<br>9.1% | 74<br>56<br>-24.3% |
| 8 | 61<br>64<br>4.6% | 80<br>86<br>7.9% | 104<br>114<br>9.8% | 92<br>122<br>32.5% | 166<br>150<br>-9.6% | 135<br>131<br>-2.9% | 135<br>126<br>-6.5% | 49<br>52<br>5.4% |
| 6 | 74<br>78<br>5.7% | 111<br>117<br>5.7% | 86<br>106<br>23.1% | 135<br>125<br>-7.2% | 117<br>134<br>14.4% | 154<br>185<br>20.2% | 147<br>149<br>1.7% | 55<br>62<br>13.3% |
| 4 | | 111<br>124<br>11.8% | 117<br>123<br>5.0% | 86<br>99<br>15.7% | 160<br>138<br>-13.6% | 154<br>157<br>1.6% | 104<br>98<br>-5.9% | |
| 2 | | 68<br>74<br>9.3% | 86<br>87<br>1.6% | 74<br>70<br>-5.7% | 61<br>60<br>-2.2% | 49<br>68<br>39.6% | 43<br>37<br>-14.7% | - Measured<br>- Calculated<br>- Discrepancy |
| | 2 | 4 | 6 | 8 | 10 | 12 | 14 | 16 |

**Table 4.12** Comparison of radial neutron flux distribution with measured, EFC Experiment 2. Transient of control rods *T*=33 sec

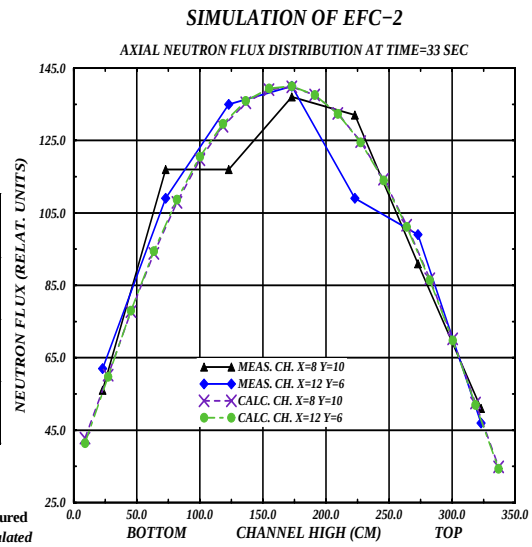


**Fig. 4.20** Comparison of axial neutron flux profiles with measured, EFC Experiment 2. Transient of control rods *T=33* sec

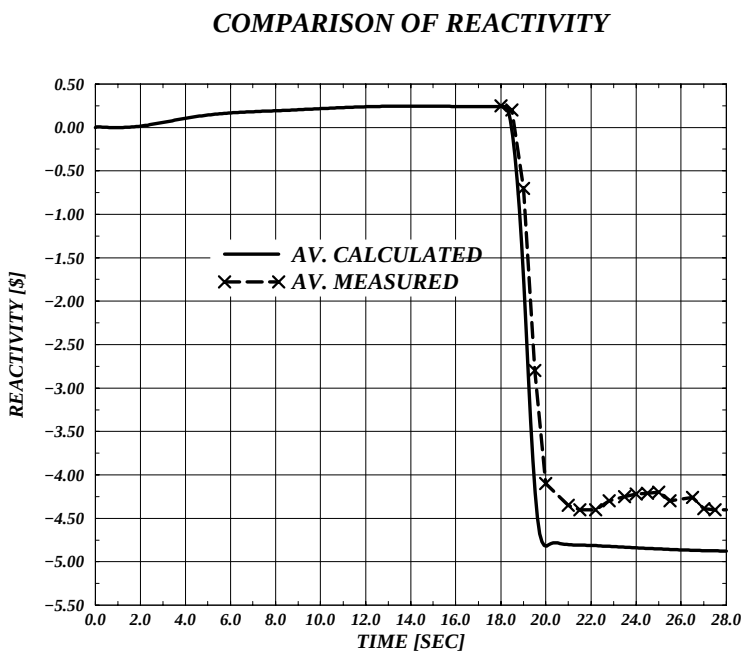


**Fig. 4.21** Reactivity comparison with measured, EFC Experiment 2. Reactivity is estimated by sum of signals from 68 KNK-5 detectors.

### 4.7.3 Analysis of the EFC Experiment 3

The EFC-3 experiment began by measuring the radial and axial neutron fluxes at the critical core condition. The criticality was reached by moving 13 control rods to the half depth of the core. Therefore, the neutron flux is shifted slightly to the bottom of the active core as indicated in fig. 4.22. This figure also indicates very good agreement between measured and calculated axial neutron flux distributions. The comparison of calculated radial neutron flux with measured is shown in Table 4.13. The average discrepancy is 4.3% in this experiment.

*CRITICAL CONDITION TIME=0 SEC*

| | 2 | 4 | 6 | 8 | 10 | 12 | 14 | 16 |
|---|---|---|---|---|---|---|---|---|
| 16 | | 41<br>47<br>14.8% | 64<br>64<br>0.1% | 64<br>67<br>5.2% | 75<br>77<br>2.9% | 68<br>72<br>6.0% | 55<br>58<br>5.2% | |
| 14 | | 86<br>88<br>2.4% | 107<br>104<br>-3.0% | 112<br>106<br>-5.0% | 125<br>122<br>-2.3% | 109<br>106<br>-2.9% | 99<br>103<br>3.9% | |
| 12 | 58<br>58<br>-0.1% | 99<br>97<br>-1.7% | 107<br>99<br>-7.8% | 103<br>111<br>7.4% | 148<br>139<br>-6.1% | 101<br>110<br>8.8% | 119<br>122<br>2.9% | 76<br>79<br>3.8% |
| 10 | 51<br>54<br>6.7% | 93<br>87<br>-6.0% | 97<br>103<br>5.7% | 167<br>165<br>-1.4% | 183<br>171<br>-6.3% | 145<br>140<br>-3.3% | 135<br>138<br>2.1% | 75<br>77<br>2.7% |
| 8 | 59<br>57<br>-3.9% | 97<br>91<br>-5.8% | 131<br>123<br>-5.9% | 160<br>163<br>1.9% | 145<br>136<br>-6.5% | 111<br>121<br>8.7% | 140<br>136<br>-2.6% | 78<br>80<br>2.6% |
| 6 | 56<br>56<br>0.3% | 90<br>85<br>-5.2% | 86<br>94<br>9.2% | 133<br>124<br>-6.5% | 107<br>116<br>8.3% | 153<br>158<br>3.4% | 145<br>147<br>1.1% | 72<br>75<br>3.7% |
| 4 | | 84<br>85<br>1.5% | 99<br>102<br>2.6% | 105<br>115<br>9.3% | 134<br>129<br>-4.0% | 149<br>144<br>-3.3% | 111<br>108<br>-2.5% | |
| 2 | | 48<br>49<br>2.5% | 68<br>67<br>-1.4% | 69<br>68<br>-1.6% | 74<br>75<br>1.5% | 77<br>73<br>-5.6% | 59<br>59<br>-0.7% | |

- Measured
- Calculated
- Discrepancy

**Table 4.13** Comparison of radial neutron flux distribution against measured, EFC Experiment 3. Critical

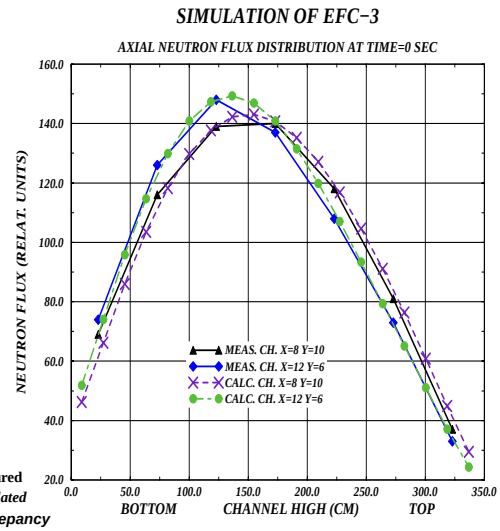


**Fig. 4.22** Comparison of axial neutron flux profiles against measured, EFC Experiment 3. Critical Condition *T=0* sec

The effective multiplication factor calculated by modeling criticality conditions is 1.00142.

15 KO and MR control rods were dropped at the velocity of 180cm/sec and neutron flux was measured after 3 and 15 sec from the beginning of transient. The transient calculations were performed by ARROTTA code and results are compared with those measured. Fig. 4.23 and Table 4.14 show comparisons of neutron flux distributions at 3 second. The radial neutron flux discrepancy with respect to the calculated increased to 6.8% at that time. The average discrepancy becomes 7.9% after 15 sec, and discrepancy for each location is shown in Table 4.15 and Fig. 4.24 at that time.

*TIME=3 SEC*

| | 2 | 4 | 6 | 8 | 10 | 12 | 14 | 16 |
|---|---|---|---|---|---|---|---|---|
| 16 | | 41<br>47<br>14.7% | 69<br>68<br>-1.2% | 48<br>52<br>7.8% | 69<br>64<br>-7.7% | 76<br>78<br>2.2% | 63<br>67<br>6.7% | |
| 14 | | 114<br>108<br>-4.9% | 130<br>123<br>-5.1% | 114<br>101<br>-11.2% | 94<br>94<br>0.3% | 122<br>118<br>-3.4% | 117<br>121<br>3.7% | |
| 12 | 67<br>63<br>-5.9% | 122<br>117<br>-4.3% | 130<br>118<br>-9.5% | 115<br>123<br>6.8% | 169<br>156<br>-7.8% | 104<br>118<br>13.5% | 118<br>119<br>1.1% | 74<br>84<br>13.4% |
| 10 | 43<br>44<br>1.9% | 94<br>84<br>-10.5% | 97<br>99<br>1.8% | 168<br>160<br>-5.0% | 207<br>192<br>-7.4% | 153<br>142<br>-7.1% | 90<br>100<br>11.0% | 67<br>66<br>-1.2% |
| 8 | 53<br>49<br>-6.8% | 71<br>71<br>-0.7% | 107<br>99<br>-7.3% | 104<br>116<br>11.7% | 165<br>151<br>-8.4% | 125<br>141<br>12.6% | 138<br>141<br>2.3% | 56<br>60<br>7.9% |
| 6 | 56<br>60<br>7.1% | 100<br>90<br>-9.8% | 84<br>87<br>3.5% | 125<br>111<br>-11.2% | 117<br>132<br>12.8% | 186<br>195<br>4.9% | 161<br>168<br>4.5% | 67<br>72<br>7.6% |
| 4 | | 92<br>95<br>3.7% | 94<br>95<br>1.5% | 67<br>85<br>27.3% | 135<br>132<br>-1.9% | 161<br>165<br>2.5% | 104<br>108<br>3.5% | |
| 2 | | 58<br>56<br>-3.7% | 63<br>69<br>8.9% | 64<br>57<br>-10.9% | 53<br>57<br>6.6% | 81<br>70<br>-13.8% | 41<br>41<br>0.0% | |

- Measured
- Calculated
- Discrepancy

**Table 4.14** Comparison of radial neutron flux distribution with measured, EFC Experiment 3. Transient of control rods *T=3* sec

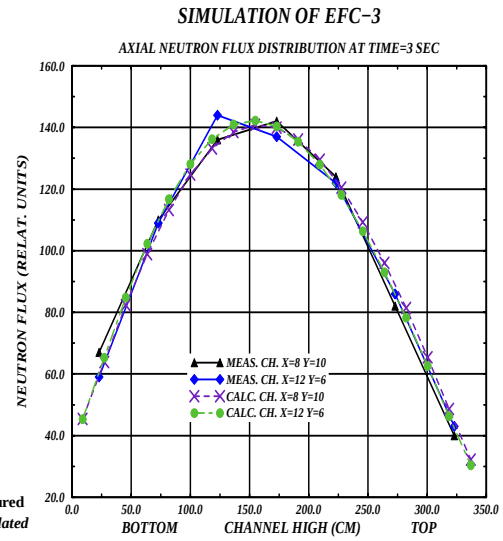


**Fig. 4.23** Comparison of axial neutron flux profiles with measured, EFC Experiment 3. Transient of control rods *T=3* sec

*TIME=15 SEC*

| | 2 | 4 | 6 | 8 | 10 | 12 | 14 | 16 |
|---|---|---|---|---|---|---|---|---|
| 16 | | 41<br>47<br>14.8% | 70<br>68<br>-2.7% | 61<br>52<br>-15.5% | 66<br>63<br>-4.0% | 70<br>78<br>10.7% | 66<br>67<br>1.9% | |
| 14 | | 115<br>109<br>-5.6% | 131<br>123<br>-5.9% | 98<br>101<br>3.0% | 90<br>94<br>4.4% | 131<br>118<br>-10.1% | 119<br>121<br>2.0% | |
| 12 | 61<br>63<br>3.4% | 119<br>117<br>-1.8% | 123<br>118<br>-4.4% | 115<br>123<br>6.6% | 164<br>156<br>-5.2% | 123<br>118<br>-4.1% | 123<br>119<br>-3.0% | 90<br>84<br>-6.7% |
| 10 | 45<br>44<br>-2.8% | 82<br>84<br>2.3% | 98<br>98<br>0.4% | 164<br>159<br>-2.9% | 213<br>191<br>-10.2% | 160<br>142<br>-11.2% | 94<br>100<br>6.4% | 70<br>66<br>-5.4% |
| 8 | 66<br>49<br>-25.4% | 61<br>70<br>15.2% | 111<br>99<br>-11.1% | 102<br>116<br>13.5% | 164<br>151<br>-7.8% | 119<br>141<br>18.7% | 139<br>142<br>1.9% | 66<br>61<br>-8.2% |
| 6 | 66<br>60<br>-9.2% | 94<br>90<br>-4.2% | 86<br>87<br>0.8% | 115<br>111<br>-3.7% | 119<br>132<br>11.2% | 193<br>196<br>1.5% | 156<br>169<br>8.4% | 61<br>72<br>18.6% |
| 4 | | 90<br>95<br>6.0% | 86<br>95<br>10.8% | 57<br>85<br>49.6% | 127<br>133<br>4.6% | 168<br>166<br>-1.3% | 115<br>108<br>-6.0% | |
| 2 | | 53<br>56<br>5.5% | 70<br>69<br>-2.0% | 53<br>57<br>7.5% | 49<br>57<br>15.6% | 78<br>70<br>-10.2% | 37<br>41<br>11.2% | |

- Measured
- Calculated
- Discrepancy

**Table 4.15** Comparison of radial neutron flux distribution with measured, EFC Experiment 3. Transient of control rods *T=15* sec

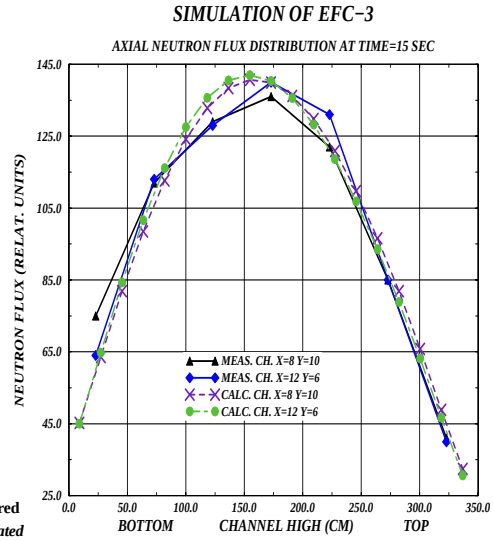


**Fig. 4.24** Comparison of axial neutron flux profiles with measured, EFC Experiment 3. Transient of control rods *T=15* sec

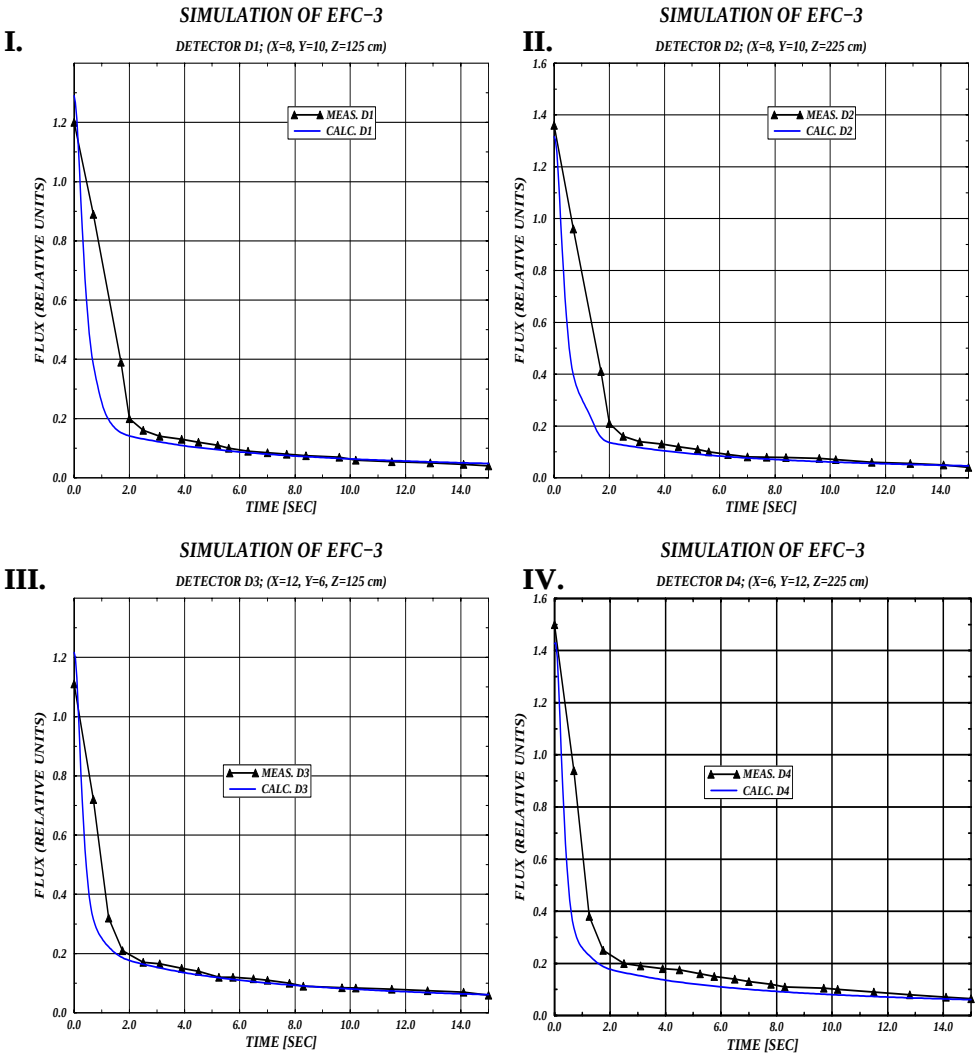


**Fig. 4.25** Comparison of neutron flux changes during and after insertion of control rods, EFC Experiment 3.

Four KNK-5 chambers were used for recording of neutron flux variation versus time. Two chambers were positioned in the instrumentation channel 10-08 and axially located 125 and 225cm below the top of graphite stack. Other two were in the channel 06-12 at the same axial location (see Figs.4.1 and 4.13). The neutron fluxes were normalized with the respect to the averaged neutron flux at critical condition in the respective channels. The neutron flux calculated by the ARROTTA code is normalized in the same way and compared against measured in Figs.4.25-I, II, III, and IV. The figures indicate that ARROTTA predicts considerably faster neutron flux decrease than measured.

The reactivity, measured during the drop of 15 control rods, reached –5.2$\beta$ [18]. The calculated reactivity, using neutron fluxes by ARROTTA as signals, is –5.25$\beta$ (see Fig.4.26). The reactivity calculation was performed with neutron fluxes summarized over those at the locations of the 68 KNK-5 detectors.

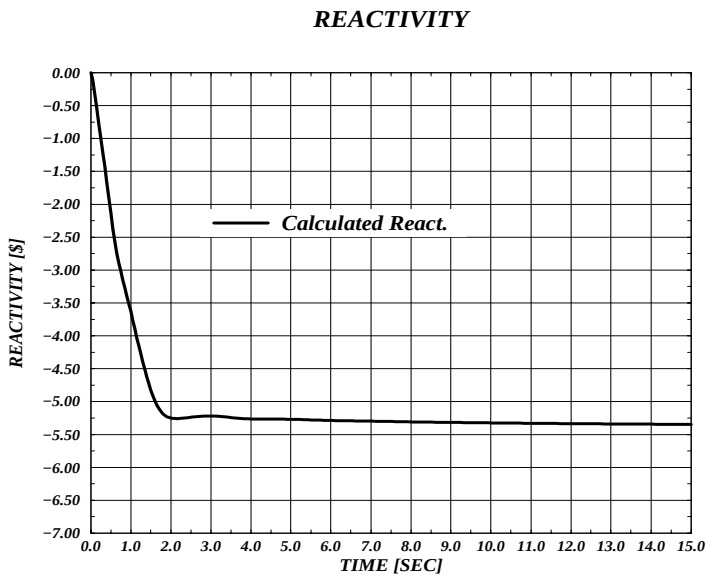


**Fig. 4.26** Reactivity estimated from ARROTTA results, EFC Experiment 3. Reactivity is calculated by sum of signals from 68 KNK-5 detectors

## 4.8 Conclusions

The results calculated by the ARROTTA code are in good agreement with those measured for all the ECF and EFC experiments. Table 4.16 summarizes the general results of the comparisons. It is seen that the effective multiplication factors, calculated for critical core configurations, are close to unity. For the comparisons of calculated radial fluxes with the measured, the discrepancy varies between 1 and 5% at critical configurations. However, the discrepancy increases up to 11% for the transients.

Table 4.16 gives the calculated and measured reactivity. It is seen that they are in good agreement as well. The larger discrepancy in control rod worth was found for the EFC-2 experiment.

We expect that ARROTTA results will be improved by employing cross sections of the non-fuel regions produced by HELIOS code. That code is capable of generating cross sections for all assembly types. Furthermore, assembly discontinuity factors would be available.

| Experiments | Calculated keff | Av. Discrepancy of Radial Flux (%) | Measured Reactivity ($\beta$) | Calculated Reactivity ($\beta$) |
|---|---|---|---|---|
| ECF Experiment 1 | 1.00410 | 4.05 | - | - |
| ECF Experiment 2 | 1.00293 | 5.35 | - | - |
| ECF Experiment 3 | 1.00623 | 0.89 | - | - |
| ECF Experiment 4 | 1.00478 | 1.08 | - | - |
| ECF Experiment 5 | 1.00019 | 1.66 | - | - |
| EFC Experiment 1 | 1.00290 | 3.91 | -0.76 | -0.78 |
| T=03 sec | - | 5.55 | | |
| T=15 sec | - | 5.11 | | |
| EFC Experiment 2 | 1.00306 | 4.07 | I. +0.25 | I. +0.25 |
| T=21 sec | - | 7.27 | II. -4.30 | II. -4.75 |
| T=33 sec | - | 11.49 | | |
| EFC Experiment 3 | 1.00142 | 4.26 | -5.20 | -5.25 |
| T=03 sec | - | 6.80 | | |
| T=15 sec | - | 7.98 | | |

**Table 4.16** Summary of comparison of ARROTTA results with experimental data of RBMK-type critical facility.

# 5 Application of Reactor Physics Calculation Capabilities at KTH for RBMK Analysis

## 5.1 Analysis of RBMK-1500 Fuel Characteristics by CASMO-4 Code and Investigation of Positive Void Reactivity Causes

### 5.1.1 Introduction

It is well known and confirmed by experiments that RBMK-type reactor has a positive void reactivity coefficient. The experiments also indicate that the void reactivity coefficient is reduced by introducing the new fuel, which has 2.4% enrichment and contains 0.41 w/% $Er_2O_3$ burnable poison. While, the previous fuel is enriched by 2.0%, and needed the insertion of additional absorbers to reduce the magnitude of the positive void coefficient. When the core is fully loaded with the new fuel, it is expected that the additional absorbers could be removed which keeping the magnitude of the positive void coefficient to low value. The removal of the additional absorbers would improve the neutron economy considerably thereby increasing the burnup that the new fuel could be taken to before removal.

A neutronics analysis of the RBMK-type fuel assembly was carried out by employing CASMO-4 lattice code at the Div. of Nuclear Power Safety, Royal Institute of Technology, Stockholm. This chapter presents calculated reactivity effects caused by variation of different fuel lattice parameters, such as fuel and graphite temperature, and coolant void. The causes of positive void reactivity have been identified.

For this study, a hypothetical-infinite reactor that contains only fuel assemblies has been modeled. Such model can not represent behavior of the prototypical reactor.

The fuel analysis by CASMO-4 provides neutron flux in 70 energy groups. In addition, concentration of different isotopes and their influence may be understood by analyzing reactivity variation with fuel burnup.

### 5.1.2 Model for the CASMO-4 Computations

The geometry of the fuel lattice is shown in Fig.5.1. The fuel channel is a zirconium-niobium alloy (Zr+2.5%Nb) tube of 88mm outer and 80mm inner diameter. The tube is placed in a cylindrical opening of 114mm diameter in a graphite block. The graphite brick base dimensions are 250×250mm. For the

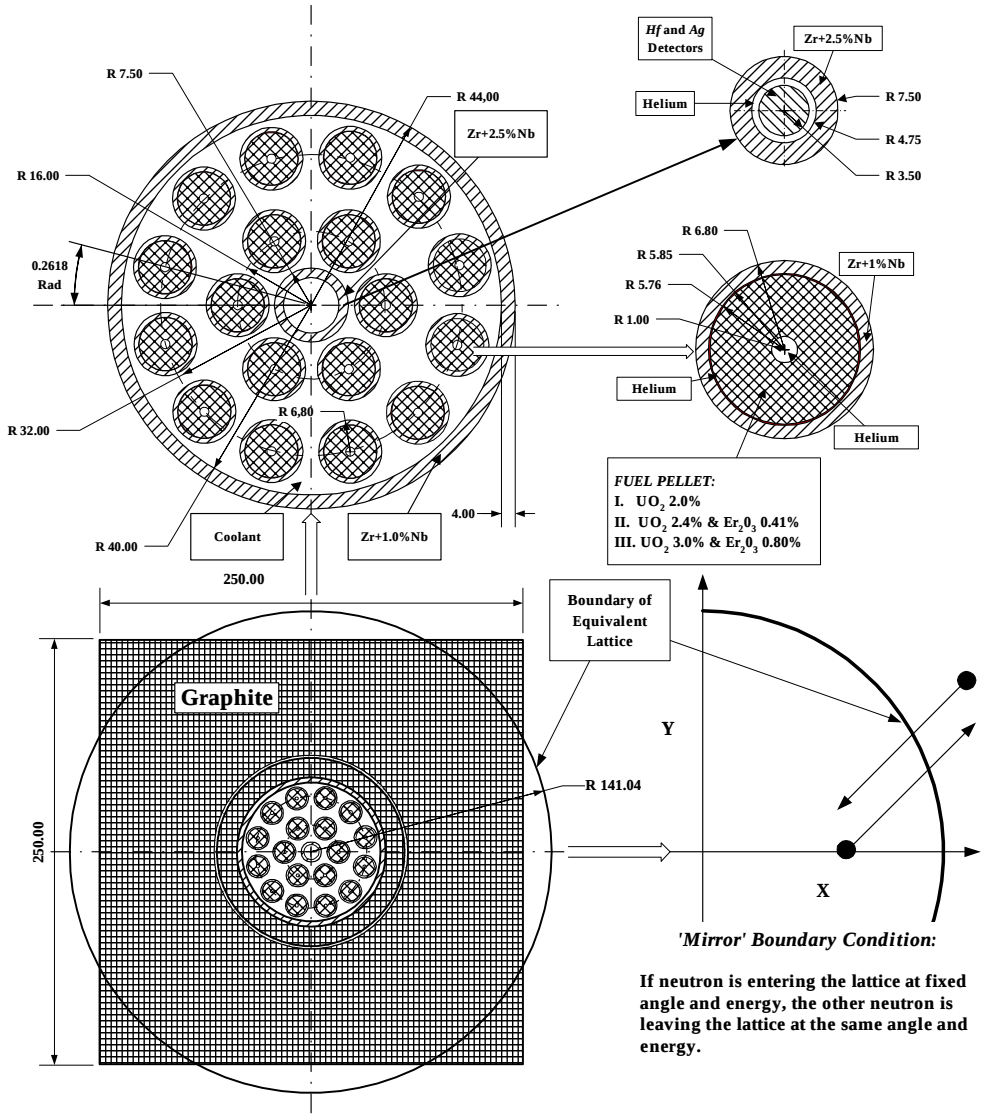


**Fig.5.1** Schematic of RBMK fuel lattice geometry used for the CASMO-4 modeling

CASMO-4 calculations, the square geometry is transferred into the equivalent cylinder of 282mm diameter (see Fig.5.1).

Rings made from graphite are mounted on the fuel channel. Their function is to keep the fuel channel in the center of graphite block. The graphite spacer rings are of two types, namely, rings of 88mm inner and 111mm outer diameter, and rings of 91mm inner and 140mm outer diameters. These rings are arranged one next to

another in such a manner that one is in contact with the channel, and the other touches the graphite block.

Fuel assembly is placed inside the fuel channel. The geometry and major parameters are shown in Fig.5.1. The fuel assembly is of cluster-type; i.e., fuel rods are concentrically allocated in two rings that are of 32mm and 74mm diameter. The central rod of 15mm outer diameter is a supporting rod that joins spacers and fuel rods. The opening in this rod is used for PDMS-R detectors. The other 18 rods are fuel rods. Six rods are located in the first concentric ring and other twelve are in the second one. Fuel pellet is 11.5mm diameter and 15mm long, and includes an axial hole of 2mm diameter at the center. This opening helps to reduce fuel temperature in the center.

The study considers three fuel types. The geometry of all these fuel assemblies is the same; the only difference is in fuel composition. The first fuel type is the fuel that was loaded in the Ignalina NPP originally and is 2.0% $U^{235}$ enriched. The second fuel contains fuel pellets that are 2.4% $U^{235}$ enriched and homogeneously mixed with 0.41w/% $Er_2O_3$ burnable absorber. This fuel type has been loaded recently in the INPP reactor core. The third fuel is assumed to have 3.0% enrichment and contain 0.80w/% erbium oxide.

The fuel lattice compositions and major parameters, which were used in the study, are presented in Table 5.1.

| **Construction** | **Material** | **Temperature [K]** | **Density [g/cm$^3$]** |
|---|---|---|---|
| Moderator | Graphite | 750 | 1,68 |
| Pressure tube | Zr+2,5% Nb | 557 | 6,55 |
| Cladding | Zr+1,0% Nb | 557 | 6,55 |
| Fuel | $UO_2$ | 1000 | 9,40 |
| Coolant | $H_2O$ | 557 | 0,7436 (~35% Void) |
| Central carrying tube | Zr+2,5% Nb | 557 | 6,55 |
| Gas | He | 557 | 1,79E -4 |
| Reactor cavity gas | He+10%$N_2$ | 750 | 2,86E -4 |

**Table 5.1** Fuel lattice compositions

Three reactivity parameters of fuel lattice are important, namely, coolant void, fuel temperature, and graphite temperature. The normal operation conditions of fuel lattice in the CASMO-4 calculations are as follows: coolant void 35%, fuel temperature 1000K, graphite temperature 750K and coolant temperature 557K. Reactivity effects are calculated by changing one of the parameters while the others are held constant. Table 5.2 summarizes the normal operating conditions.

| Parameter | Magnitude |
|---|---|
| Average Void [%] | 35 |
| Average Fuel Temp. [K] | 1000 |
| Average Coolant Temp. [K] | 557 |
| Average Graphite Temp. [K] | 750 |
| Power Density [W/g $_{\text{Metal U}}$] | 22.9 |
| Boundary Condition [-] | "Mirror" |

**Table 5.2** Summary of normal operating or "historical" conditions

The "historical" conditions are assumed as shown in Table 5.2. The "historical conditions" mean the averaged temperatures and coolant void used for fuel depletion calculations. The computations indicate slightly different results if different "historical" conditions are assumed. These differences are caused by the slightly different concentration of isotopes generated during the fuel burnup due to the changes in he neutron spectrum. Fortunately, the differences are small and general characteristics are only slightly different. Therefore, the results obtained assuming the "historical conditions" defined in Table 5.2 may provide a representative behavior of fuel.

The "mirror" boundary condition is assumed, i.e., it was assumed that if a neutron is entering the lattice at a fixed angle and energy, an another neutron is leaving the lattice at the same angle and energy. This boundary condition is shown schematically in Fig.5.1. The "mirror" condition is equivalent to the infinite reactor assumption.

### 5.1.3 Reactivity Effects and Coefficients

#### 5.1.3.1 The Infinite Multiplication Factor

Multiplication factor is of major importance in the reactor physics analysis. Therefore, this study is focused first on infinite multiplication factor $k_{inf}$. Fig.5.2 shows $k_{inf}$ variation versus fuel burnup for the three fuel types at normal operating conditions. $k_{inf}$ decreases almost linearly for 2.0% enriched fuel, but it varies in a different manner for the other two fuel types. There is a slight increase in $k_{inf}$ up to 5-7 MWd/kg of fuel burnup and only at greater fuel exposure, the $k_{inf}$ starts to decrease. Thus, the $k_{inf}$ variation is not linear for the fuel that is mixed with erbium burnable absorber. This is primarily due to the absorption of neutrons in the erbium when the fuel is fresh. As the fuel burns the erbium also burns, whereby the total absorption in the fuel decreases and the $k_{inf}$ increases. Later, as the fuel burns further, the fission neutrons decrease and the $k_{inf}$ decreases in value.

Analysis of the RBMK cores with the STEPAN and WIMS-$D_4$ codes at the Kurchatov Institute showed that fuel lattice calculations resulting 1.08 in $k_{inf}$ correspond to effective multiplication factor $k_{eff}$ of 1.0. Hence, examination of

Fig.5.2 indicates that 2.0% enriched fuel assembly reaches $k_{inf}$ value of 1.08 at 12 MWd/kg fuel burnup. The fuel that has 2.4% enrichment reaches $k_{inf}$=1.08 at 15MWd/kg, and 3.0% enriched fuel reaches at 19MWd/kg burnup.

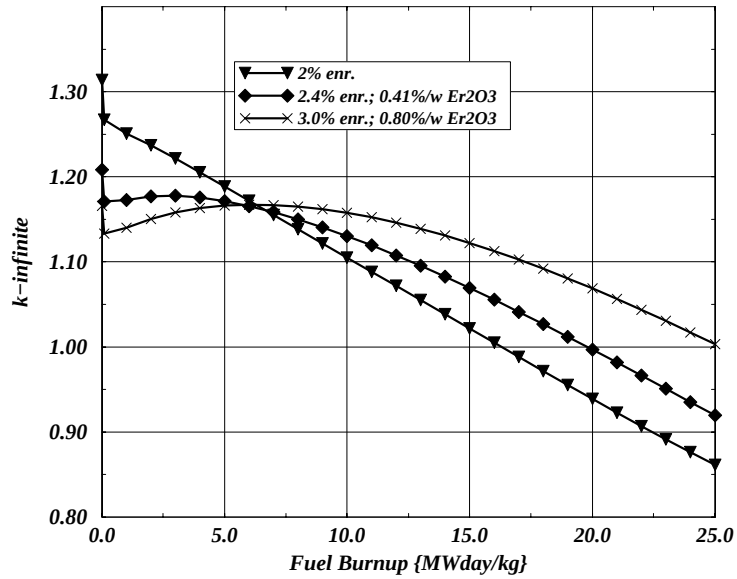


**Fig.5.2** The $k_{inf}$ versus fuel burnup

### 5.1.3.2 The Void Reactivity Effect

The void reactivity for all fuel types considered becomes increasingly positive with fuel burnup increase as shown in Fig.5.3. The reasons for this are quit clear for the erbium-poisoned fuel in which the burnup of the erbium reduces the total absorption in the core, leading to more positive void coefficient. The absorption in the 2% fuel also decreases with fuel burnup.

Fig.5.3 shows reactivity effects versus fuel depletion for all fuel types analyzed. The void reactivity effect is defined by equation 5.1:

$$\Delta\rho_{\gamma} = \frac{(k_{inf}^{100\%} - k_{inf}^{35\%}) \cdot 100}{k_{inf}^{100\%} \cdot k_{inf}^{35\%}} \qquad \textbf{Eq.5.1}$$

Here, $\Delta\rho_{\gamma}$ is the reactivity change considering 100% and 35% coolant voiding in the fuel channel. The variable $k_{inf}$ stands for the infinite multiplication factor. The superscripts *100%* and *35%* indicate coolant void in percents. The other thermal-physical parameters for fuel lattice are kept constant (see Table 5.2).

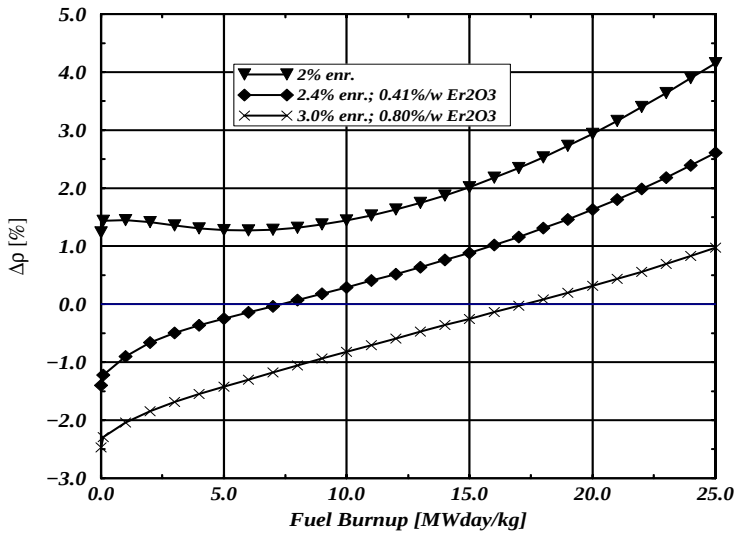


**Fig.5.3** Coolant void reactivity effect $\Delta\rho_\gamma$ induced by coolant void change from 35% to 100%

The calculation of void reactivity indicates that reactivity effect is positive for 2.0% enrichment fuel. The $\Delta\rho_\gamma$ slightly decreases up to 8MWd/kg burnup and increases rapidly with larger fuel burnup. Similar analysis of the other two fuel types indicates that $\Delta\rho_\gamma$ is negative at the beginning of fuel depletion. This effect has a tendency to be more negative as higher the fuel enrichment and higher burnable absorber concentration is incorporated. Fig.5.3 indicates negative $\Delta\rho_\gamma$ until 7 MWd/kg for 2.4% enriched fuel that contains 0.41w/% $Er_2O_3$, and until 18 MWd/kg for 3.0% enriched and 0.80w/% $Er_2O_3$ fuel.

Variation of $k_{inf}/k_{inf}^{0\%}$ as a function of coolant void and fuel burnup is shown in Fig.5.4, where I, II and III distinguish fuel of 2.0%, 2.4% and 3.0% enrichment, respectively. The figure shows ratio between $k_{inf}$ (numerator), which is calculated at different coolant voids, and $k_{inf}^{0\%}$ (denominator) as a fixed reference value that is multiplication factor at 0% voiding.

Fig.5.4-I shows variation of $k_{inf}$ for 2.0% enriched fuel versus coolant void. The infinite multiplication factor increases with the higher voiding and that increase is non-linear up to 15 MWd/kg of fuel burnup. It becomes highly non-linear with greater fuel burnup.

Different shapes, which represent the multiplication factor variation for 2.4% enrichment fuel with erbium poison, are indicated in Fig.5.4-II. The variation of $k_{inf}$

versus coolant void is highly non-linear at the beginning of fuel burnup up to 2MWd/kg, but then is practically linear up to 15MWd/kg.

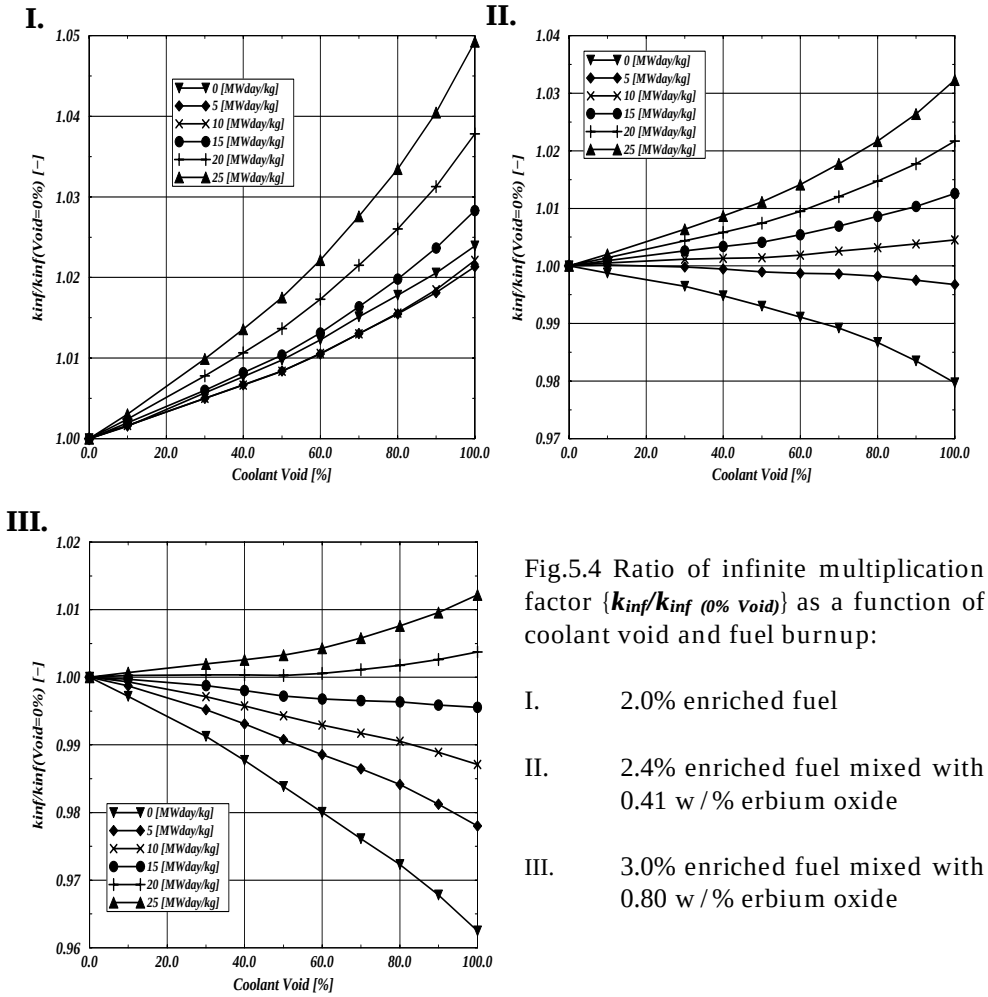


Fig.5.4 Ratio of infinite multiplication factor {$k_{inf}/k_{inf\ (0\%\ Void)}$} as a function of coolant void and fuel burnup:

I. 2.0% enriched fuel

II. 2.4% enriched fuel mixed with 0.41 w/% erbium oxide

III. 3.0% enriched fuel mixed with 0.80 w/% erbium oxide

The variation of infinite multiplication factor, calculated for 3.0% enrichment fuel, is presented in the Fig.5.4-III. This figure indicates non-linear variation up to 5MWd/kg and above 20 MWd/kg of fuel burnup. The $k_{inf}$ variation may be approximated as linear for the burnup values between 5 and 20 MWd/kg.

It is sometimes more convenient to use coolant void reactivity coefficient $\alpha_\gamma$, i.e. reactivity change /% void in the channel and use that for prediction of reactivity change that may result in different voiding schemes. Fig.5.5 shows the $\overline{\alpha_\gamma}$ function versus fuel burnup for the fuel types considered. Here, the void reactivity

coefficient is calculated by assuming linear reactivity variation versus void and defined by equation 5.2:

$$\overline{\alpha}_{\gamma} = \frac{\int_{\gamma_1}^{\gamma_2} \alpha_{\gamma} d\gamma}{\int_{\gamma_1}^{\gamma_2} d\gamma} \cong \frac{\Delta\rho_{\gamma}}{\Delta\gamma} \qquad \textbf{Eq.5.2}$$

Here, $\Delta\rho_{\gamma}$ represents reactivity difference as defined by Eq.5.2, and $\Delta\gamma$ is coolant void change. Eq.5.2 and the results shown in Fig.5.5 should be interpreted with care, since there is a slight non-linear dependence of reactivity effects versus voiding as Fig.5.4 indicates. In spite of this, Fig.5.5 provides relatively accurate values for the void reactivity coefficient versus fuel burnup.

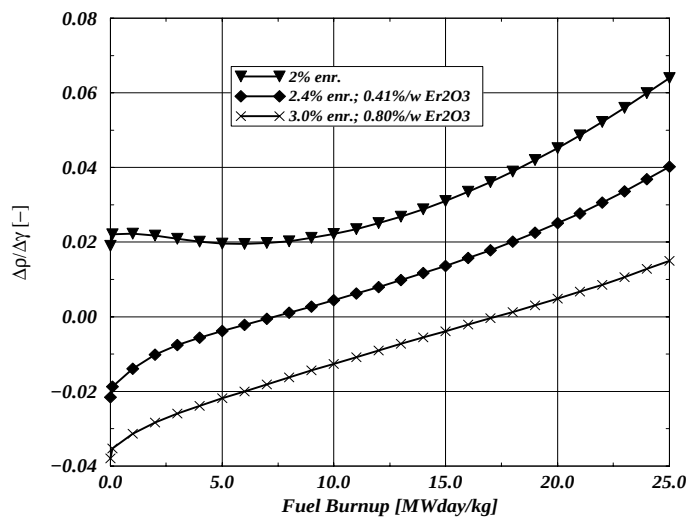


**Fig.5.5** Coolant void reactivity coefficient $\overline{\alpha}_{\gamma}$ versus fuel burnup

### 5.1.3.3 The Doppler Effect

The reactivity feedback that is induced by the change in fuel temperature is a very important negative reactivity feedback since it is prompt and does not depend on the time to transfer heat from the fuel elements to the coolant to generate the vapor. The fuel temperature reactivity effect is studied by considering initial 1000K and final 1200K average fuel temperature. The reactivity effects caused by fuel temperature changes are shown in Fig.5.6-I. The Doppler effect is calculated by employing relation that is defined by eq.5.3:

$$\Delta\rho_{T_F} = \frac{(k_{inf}^{1200K} - k_{inf}^{1000K}) \cdot 100}{k_{inf}^{1200K} \cdot k_{inf}^{1000K}} \qquad \textbf{Eq.5.3}$$

Here, $k_{inf}$ stands for infinite multiplication factor at the fuel temperatures of 1200K and 1000K. The other thermal-physical parameters of a fuel lattice are invariant, as presented in Table 5.2. Fig.5.6-I indicates negative reactivity insertion when the temperature of the fuel increases for the three fuel types considered.

The fuel temperature reactivity temperature was calculated by assuming linear reactivity variation versus fuel temperature. This assumption should be considered with care, because reactivity versus fuel temperature is not strictly linear. The computation of the Doppler coefficient was performed according to equation 5.4:

$$\overline{\alpha}_{T_F} = \frac{\int_{T_{F1}}^{T_{F2}} \alpha_{T_F} dT_F}{\int_{T_{F1}}^{T_{F2}} dT_F} \cong \frac{\Delta\rho_{T_F}}{\Delta T_F} \qquad \textbf{Eq.5.4}$$

Here, $\Delta\rho_{TF}$ is the reactivity effect calculated by Eq.5.3, and $\Delta T_F$ stands for the fuel temperature difference. The Doppler coefficient versus fuel burnup is shown in Fig.5.6-II.

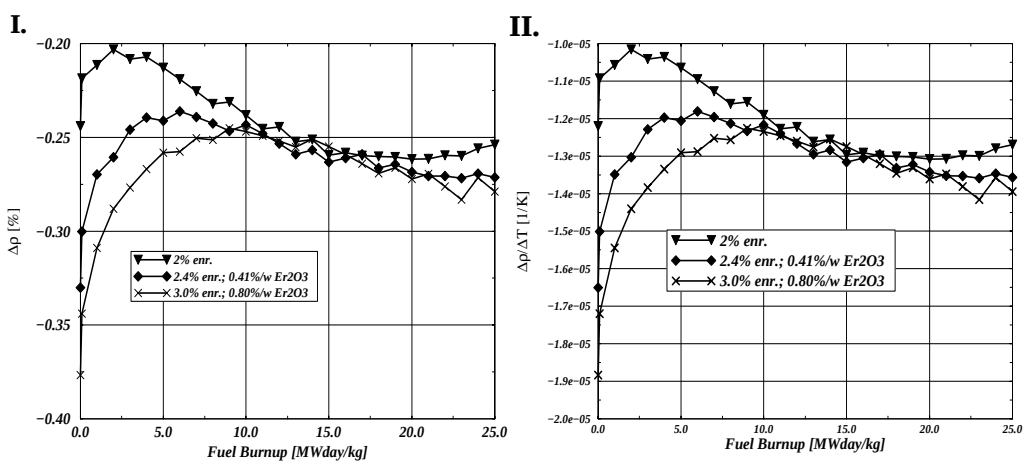


**Fig.5.6**

I. The fuel temperature reactivity effect $\Delta\rho_{TF}$ in the case of fuel temperature change from 1000K to 1200K

II. The Doppler coefficient $\overline{\alpha}_{TF}$ versus fuel burnup

#### 5.1.3.4 The Reactivity Effects Caused by Graphite Temperature Changes

The RBMK-1500 reactor contains graphite for the neutron moderation, therefore, it is important to know the characteristics of the reactivity effects caused by the graphite temperature changes. The calculated results for reactivity effect versus fuel burnup are presented in Fig.5.7-I and reactivity coefficients of graphite temperature are shown in Fig.5.7-II. The reactivity effect and the reactivity coefficient are calculated in the same manner as those were calculated for the fuel temperature changes. Therefore, the graphite temperature is considered as variable in this case and the other fuel lattice thermal-physical parameters kept constants as in Table 5.2.

The Fig.5.7-I indicates that graphite reactivity coefficient of 2.0% enriched fuel is slightly positive for all burnup levels; on the contrary, this coefficient is negative up to 5-7MWd/kg fuel burnup in for the fuels considered with erbium burnable poison. The reactivity coefficients become positive and similar in amplitude at larger fuel burnup for the three fuel types.

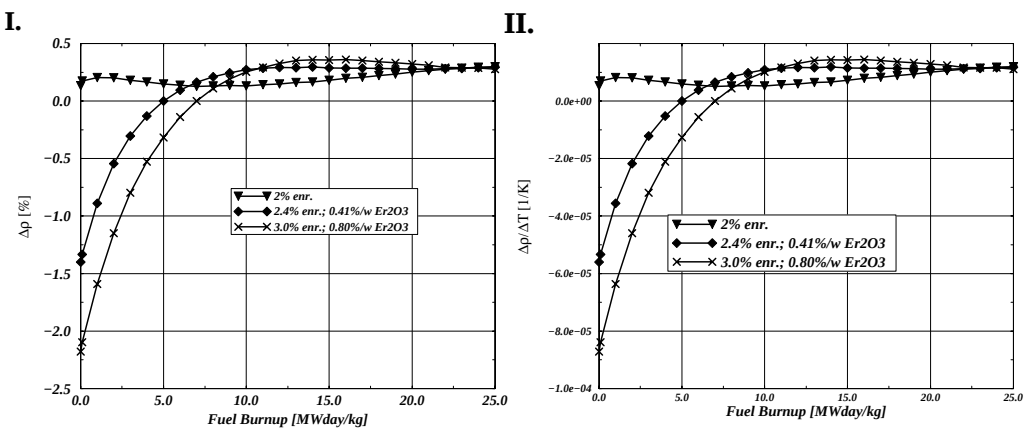


**Fig.5.7**

I. The reactivity effect $\Delta\rho_{TM}$ of moderator temperature in the case of graphite temperature change from 750K to 1000K

II. The average graphite reactivity coefficient $\overline{\alpha}_{TM}$ versus fuel burnup

### 5.1.4 Causes of Positive Coolant Void Reactivity

The fuel lattice studies indicate that fuel enriched to 2.0% has positive void reactivity at all fuel burnup levels. Whereas, higher enrichment fuel that contain burnable absorber have somewhat different void reactivity characteristics. As shown in Fig.5.3, the reactivity, introduced by increasing void, is negative for 2.4%

and 3.0% enriched fuel at the beginning of fuel depletion. The positive reactivity occurs at greater fuel exposure.

### 5.1.4.1 Four-Factor Formula

In order to understand the causes of the positive void reactivity change, each term of the four-factor formula is analyzed versus coolant void change. The general idea of this study is to point out the terms of the four-factor formula that are most sensitive to the coolant void changes. The four-factor formula is defined by Eq.5.5:

$$k_{inf} = \eta \cdot f \cdot p \cdot \varepsilon \qquad \textbf{Eq.5.5}$$

Here, $\eta$ represents the average number of neutron emitted per thermal neutron absorbed in fuel. $f$ stands for thermal utilization. $p$ is the resonance escape probability, i.e., the probability that a fission neutron will escape capture in the resonances as it slows down to thermal energies. $\varepsilon$ is fast fission factor that represents the ratio of the total number of neutrons emitted from both thermal and fast fission to the number emitted in the thermal fission alone.

The sensitivity of a term in the four-factor formula is defined as the relative difference between its magnitude calculated at 0% void and at higher coolant voiding. This is expressed by Eq.5.6:

$$\Delta x = \frac{x_{0\%} - x_{0 \div 100\%}}{x_{0\%}} \cdot 100 \qquad \textbf{Eq.5.6}$$

Here, $\Delta x$ stands for relative difference or "sensitivity", as that is named in this study, expressed in percent. The $x_{0\%}$ represents a variable of the four-factor formula calculated at zero percent coolant voiding and $x_{0\% \div 100\%}$ indicates a variable computed by changing coolant void between 0% and 100%.

| Fuel Type | Fuel Burnup MWd/kg | $\eta$ | $p$ | $f$ | $\varepsilon$ |
|---|---|---|---|---|---|
| 2.0% enr. fuel | 0 | 1.4746 | 0.8236 | 0.8742 | 1.0849 |
| 2.0% enr. fuel | 20 | 1.0564 | 0.8242 | 0.8716 | 1.0669 |
| 2.4% enr. & 0.41w / % $Er_2O_3$ fuel | 0 | 1.3748 | 0.8109 | 0.8961 | 1.0961 |
| 2.4% enr. & 0.41w / % $Er_2O_3$ fuel | 20 | 1.1300 | 0.8182 | 0.8837 | 1.0726 |
| 3.0% enr. & 0.80w / % $Er_2O_3$ fuel | 0 | 1.3385 | 0.7974 | 0.9131 | 1.1110 |
| 3.0% enr. & 0.80w / % $Er_2O_3$ fuel | 20 | 1.2212 | 0.8094 | 0.8985 | 1.0825 |

**Table 5.3.** Reference values of the various terms in the four-factor formula terms calculated at 0% void

### 5.1.4.2 Sensitivity Analysis

The sensitivity analysis was performed for each term of the four-factor formula by considering different fuel burnup and fuel types. Results of this study are presented in Fig.5.8-I, II and III. In addition, the absolute values of four-factor formula terms calculated at 0% voiding are introduced in Table 5.3, which are reference values for the sensitivity analysis.

Fig.5.8-I shows results of sensitivity studies for 2.0% enriched fuel. The analysis indicates that the fast fission factor $\varepsilon$ and the resonance escape probability $p$ variations are only slightly dependent on fuel burnup. Therefore, the $\varepsilon$ and $p$ are plotted only for zero fuel burnup and may represent all fuel depletion points. However, variations of the other two parameters $\eta$ and $f$ versus coolant void are strongly dependent on fuel burnup, and are shown at zero and 20MWd/kg burnup. The same regularity is observed for the other two fuel types; therefore, the Fig.5.8-II and III are plotted in the same manner.

Examination of Fig.5.8-I indicates that resonance escape probability decreases about 5% in the case of 100% voiding, while, the other three parameters increase. The decrease of the escape probability is not sufficient to compensate the increase of the other three four-factor formula terms. Hence, increase of $\eta$, $\varepsilon$ and $f$ cause an increase of the infinite multiplication factor.

Fig.5.5 indicates that positive void reactivity rapidly increases when 2.0% enrichment fuel is depleted more than 10 MWd/kg. Examination of Fig.5.8-I shows that $\eta$ and $f$ versus void increase faster at 20MWd/kg burnup in comparison to the same changes for the fresh fuel. The sensitivities of these two terms are considerable and most likely indicate reasons for the increase of positive void reactivity at higher fuel burnup. The increase of the void reactivity coefficient may be caused by the decrease of absorption in fuel lattice and increase of the average number of neutrons emitted per thermal neutron absorbed in fuel.

The analysis of the four-factor formula sensitivity for the fuel having higher enrichment and containing erbium indicates different results. As it was discussed before, the fuel having 2.4% enrichment and containing 0.41w/% erbium has negative void reactivity coefficient at the beginning of fuel burnup (see Fig.5.5). This coefficient becomes positive at 7 MWd/kg. Causes of this effect may be explained by the results introduced in Fig.5.8-II. The figure indicates that the thermal utilization changes versus void is less sensitive in comparison to the ordinary 2.0% enrichment fuel at zero and even at 20MWd/kg fuel burnup.

The second variable having considerable influence on the reactivity changes is $\eta$. Calculation by CASMO-4 shows that $\eta$ sensitivity versus void is strongly

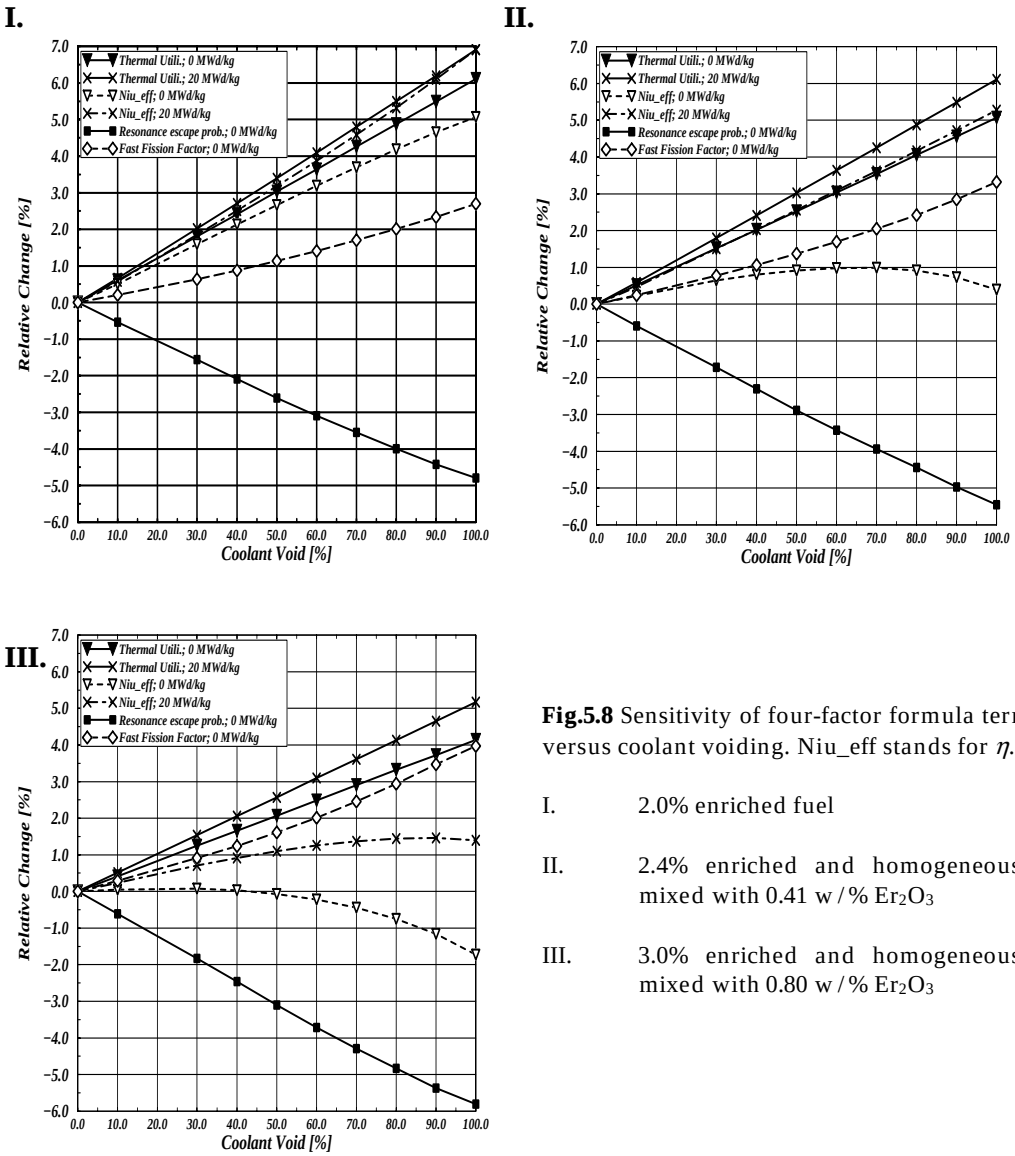


**Fig.5.8** Sensitivity of four-factor formula terms versus coolant voiding. Niu_eff stands for $\eta$.

I. 2.0% enriched fuel

II. 2.4% enriched and homogeneously mixed with 0.41 w / % $Er_2O_3$

III. 3.0% enriched and homogeneously mixed with 0.80 w / % $Er_2O_3$

dependent on fuel burnup in for higher enrichment fuel. This phenomenon is observed by comparing Fig.5.8-I and Fig.5.8-II. Figures indicate different $\eta$ shapes versus void. The $\eta$ slightly increases for 2.4% enriched fuel at zero burnup and that increase is even less for higher voiding. The $\eta$ approximately increases by 0.5% at full voiding, whereas, this parameter increases by up to 5.0% in the case of ordinary fuel at the same conditions.

The $\eta$, $\varepsilon$ and $f$ increase for the 2.4% enriched fuel even at zero burnup, but it should be noted that changes are smaller in comparison to the 2% fuel. Furthermore, the resonance-escape probability decreases even with higher slope for the fuel of higher enrichment. These changes are responsible for the negative void reactivity coefficient calculated for the fresh 2.4% enriched fuel.

However, positive void reactivity coefficient appears at higher fuel burnup. That is caused most probably by the increased sensitivity of the thermal utilization and $\eta$ as shown in Fig.5.8-II at 20MWd/kg fuel burnup. In this case, the gradients of the thermal utilization and $\eta$ increase and are almost the same as for fresh 2% fuel.

Results of the sensitivity analysis for fuel enriched to 3.0% with 0.8w/% erbium are shown in Fig.5.8-III. The figure indicates decrease of two variables of the four-factor formula, namely, $p$ and $\eta$ as coolant void increases at low burnup. The $\eta$ decreases down to –2% in the case of 100% voiding. The figure also shows that thermal utilization is less sensitive and increases only by 4% for fresh and by 5% for depleted fuel at 100% voiding.

The negative void reactivity coefficient for fresh 3.0% enriched fuel is caused by decrease of $\eta$ and $p$, which are not compensated by the increase of $f$ and $\varepsilon$ in the case of coolant voiding. The reactivity becomes slightly positive at higher burnup, since $\eta$ becomes positive and $f$ sensitivity increases as shown in Fig.5.8-III.

Figs.5.8 leads to the conclusion that terms $f$ and $\eta$ of the four-factor formula are affecting the void reactivity coefficient the most. Therefore, the following study is concentrated on more detailed analysis of these two parameters.

### 5.1.4.3 Analysis of Thermal Utilization

The thermal utilization is defined as ratio of number of neutrons absorbed in the fuel per second, to the number absorbed in both fuel and other fuel lattice components per second

$$f = \frac{\sum_{i=1}^{NI_1} \int_{V_1} \int_0^{4eV} \Sigma_{a1,i}(E) \cdot \Phi(\mathbf{r},E) \cdot dE \cdot d\mathbf{r}}{\sum_{i=1}^{NI_1} \int_{V_1} \int_0^{4eV} \Sigma_{a1,i}(E) \cdot \Phi(\mathbf{r},E) \cdot dE \cdot d\mathbf{r} + \sum_{i=1}^{NI_2} \int_{V_2} \int_0^{4eV} \Sigma_{a2,i}(E) \cdot \Phi(\mathbf{r},E) \cdot dE \cdot d\mathbf{r}} \qquad \textbf{Eq.5.7}$$

Here, $\mathbf{r}$ is three-dimensional position vector; $V_1$ and $V_2$ are fuel and non-fuel volumes, respectively. $NI_1$ and $NI_2$ stand for number of isotopes in the fuel and in the non-fuel volumes, respectively. $i$ stands for isotope. $E$ is energy and is integrated from 0 to 4eV. $\Sigma_{a1,i}$ and $\Sigma_{a2,i}$ are macroscopic absorption cross sections for individual isotopes $i$ located in the fuel and in the non-fuel volumes, respectively. $\Phi(\mathbf{r}, E)$ is energy and space dependent neutron flux.

Absorption rate in the fuel and absorption rate in the whole fuel lattice decreases in the case of coolant voiding since the spectrum becomes harder. However, the absorption rate in the whole lattice decreases faster (denominator in Eq.5.7) than in the fuel (numerator in Eq.5.7). Consequently, *f* increases with voiding.

The increase of void induces two effects. First, water is a considerable absorber that disappears when density decreases and absorption reaction rate in the lattice decreases. Second important effect is the hardening of the thermal neutron spectrum. This decreases the macroscopic absorption cross sections for the isotopes that have *1/v* dependent microscopic cross sections. The macroscopic absorption cross section of each isotope is calculated as follows in Eq.5.8:

$$\Sigma_{a,i} = \frac{\int_V \int_0^{4eV} \Phi(\mathbf{r},E) \cdot \Sigma_{a,i}(E) \cdot dE \cdot d\mathbf{r}}{\int_V \int_0^{4eV} \Phi(\mathbf{r},E) \cdot dE \cdot d\mathbf{r}} \qquad \textbf{Eq.5.8}$$

Here, i stands for an isotope and $\Sigma_{a,i}(E)$ is energy dependent macroscopic absorption cross section for isotope i. The other variables are the same as in Eq.5.7.

The neutron flux hardening is caused by water disappearance. In RBMK-type reactor, water is used as coolant, but it also moderates neutrons slightly. Therefore, the neutron spectrum in fuel pins is softer than in graphite blocks. In general, the thermal neutron spectrum is defined by the graphite (750K). In addition neutrons are moderated by water (557K) while they reach fuel pins (see Fig.5.1). High coolant voiding eliminates the additional moderation by water, and the thermal neutron spectrum is defined only by graphite.

The neutron flux spectrum shift to the higher energies is shown in Fig.5.9. Two cases are shown, namely, spectrum at 35% and 100% voiding. The spectrum is condensed into the 70 energy groups and introduced as discrete function. The curves are presented in relative units and scale is indicated on the right hand axis. The shift of spectrum is into the Pu and Er resonance below 0.4 eV. Thus, the absorption in fuel should increase.

Examination of Eq.5.7 indicates that the increase of absorption cross section in the fuel region may decrease the sensitivity of the thermal utilization. That is, if absorption in fuel would be considerably higher than absorption in the graphite and coolant, the loss of coolant would introduce only small changes in thermal utilization values. This conclusion is confirmed by the fact that the sensitivity of thermal utilization is decreased by introducing fuel of higher enrichment and mixed with erbium burnable absorber as shown in Fig.5.8-II and III. In addition, these figures indicate a sensitivity increase at higher fuel burnup; i.e., *f* sensitivity increases as erbium burns out, and absorption in the fuel region decreases.

The erbium was chosen, since natural erbium contains 22.9 w/% $Er^{167}$ isotope. This isotope has high microscopic absorption cross-sections in the thermal energy interval as shown in Fig.5.9. The plot also shows wide absorption resonance peak in the energy interval between 0.3 and 0.8eV. This resonance peak functions as a "neutron trap" when neutron spectrum is hardened. Thus, presence of erbium in the fuel composition increases absorption in fuel if spectrum is shifted to the higher energies and that is the reason for having a negative void coefficient for fresh fuel and positive void coefficient when the erbium has been depleted.

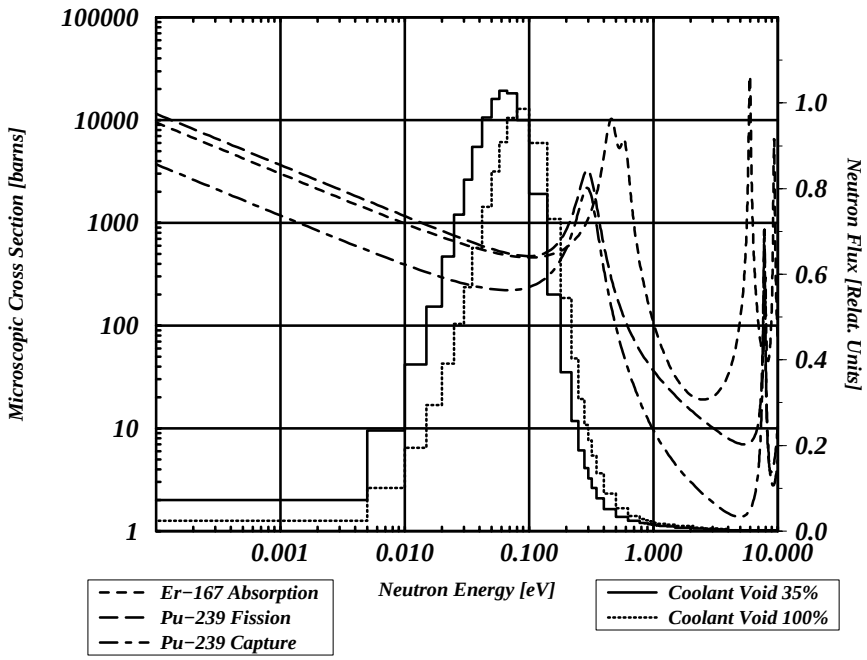


**Fig.5.9** Thermal neutron flux spectrum (right) and microscopic cross sections of $Pu^{239}$ and $Er^{167}$ (left)

## 5.1.4.4 Analysis of η Effective

The second four-factor formula term sensitive to the voiding is the average number of neutron emitted per thermal neutron absorbed in fuel $\eta$. This term is strongly dependent on fuel type and fuel burnup. The $\eta$ is calculated by CASMO-4 code as follows in Eq.5.9:

$$\eta = \frac{\sum_{i=1}^{NI_1} \int_{V_1} dr \int_0^{4eV} \nu_{f,i}(E) \cdot \Sigma_{f,i}(E) \cdot \Phi(\mathbf{r},E) \cdot dE \cdot d\mathbf{r}}{\sum_{i=1}^{NI_1} \int_{V_1} \int_0^{4eV} \Sigma_{a,i}(E) \cdot \Phi(\mathbf{r},E) \cdot dE \cdot d\mathbf{r}} \qquad \textbf{Eq.5.9}$$

Here, $\Sigma_{f,i}(E)$ is energy dependent macroscopic fission cross section for isotope i. $\nu_{f,i}$ is a number of neutrons generated by fission of isotope *i*. The other variables are the same as in Eq.5.7.

Eq.5.9 shows, that $\eta$ is dependent on neutron flux weighted integrals. These integrals are also dependent on the variation of the microscopic absorption and fission cross sections with energy. Studies of $U^{235}$ cross sections indicate that $|d\sigma_a/dE| > |d\sigma_f/dE|$. Therefore, for 2.0% enriched fuel, the ratio between integrals in numerator and denominator of Eq.5.9 increases as the neutron spectrum is hardened.

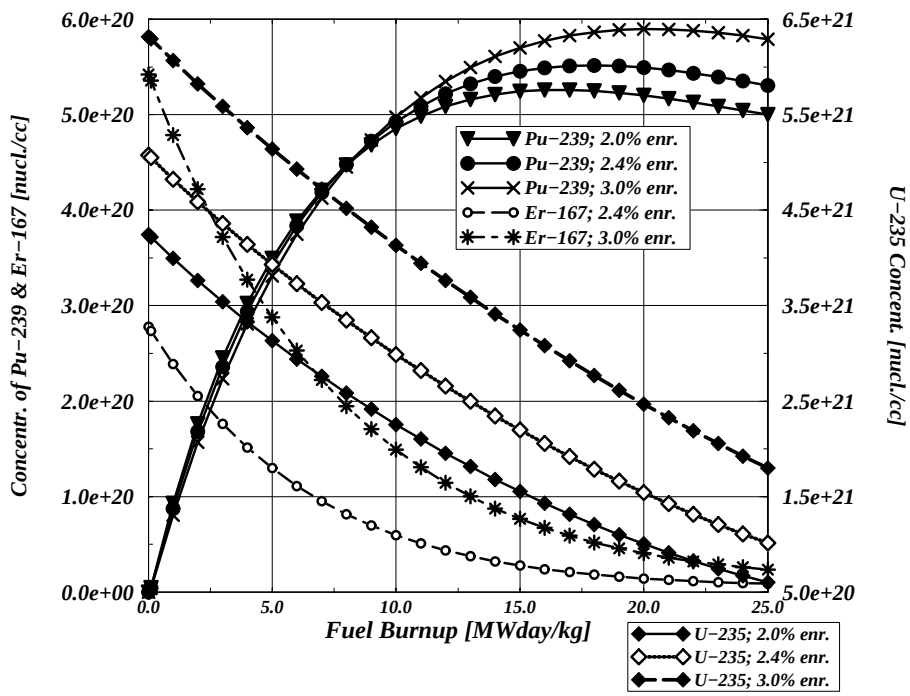


**Fig.5.10** $U^{235}$ (right), $Pu^{239}$ and $Er^{167}$ (left) concentration changes versus fuel burnup. CASMO-4 calculation results

The effect is different in the case of fuel with erbium. Then, the integral in the denominator increases almost at the same rate as the integral in the numerator for 2.4% enriched fuel with 0.41w/% erbium, and $\eta$ increases just slightly. If the fuel

enrichment and the concentration of erbium are increased, the denominator increases at a higher rate than the numerator does. This leads to the decrease of $\eta$ at large voiding, as seen in Fig.5.8-III. The increase of absorption in fuel is caused by $Er^{167}$ absorption resonance peak, as shown in Fig.5.9.

Calculations indicate that the sensitivity of $\eta$ increases for all of the fuel types at higher fuel burnup. The cause is that some of isotopes such as $U^{235}$ and $Er^{167}$ burn out, and at the same time, many fission products are produced. The isotopes, such as $Pu^{239}$, $Pu^{240}$, $Pu^{241}$, $Np^{237}$ and many other fission products, influence the void reactivity. The burnup calculations by the CASMO-4 code indicate that the characteristics of the fuel are largely defined by the properties of $Pu^{239}$, whose concentration increases faster than concentration of other isotopes at higher fuel burnup.

Fig.5.10 shows the concentrations of $U^{235}$, $Pu^{239}$ and $Er^{167}$ isotopes versus fuel burnup for all the fuel types. The concentration of $Pu^{239}$ reaches a maximum value at 15MWd/kg. The concentrations decreases slightly for fuel that has 2.0% and 2.4% initial enrichment at deeper burnup, while it reaches saturation for 3.0% enriched fuel.

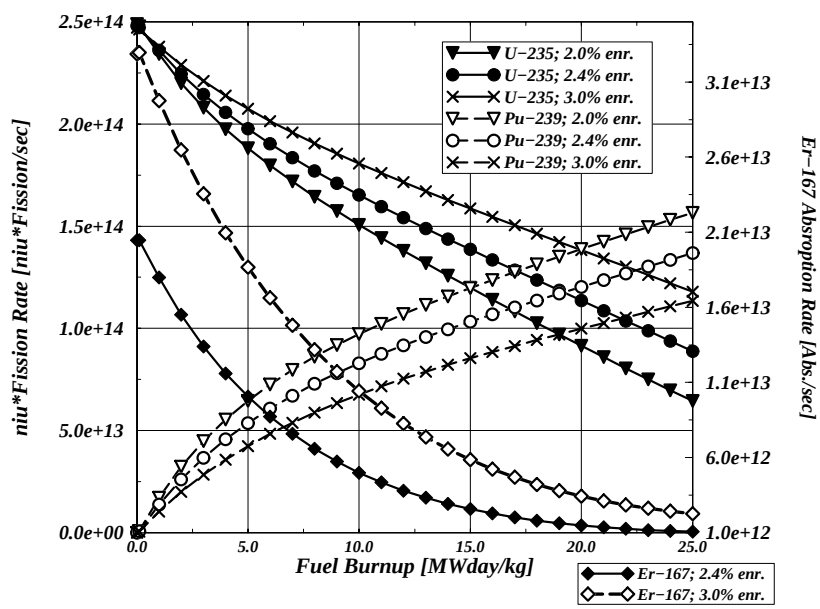


**Fig.5.11** $\nu$·fission reaction rate versus fuel burnup for $U^{235}$ and $Pu^{239}$ (left) and absorption reaction rate of $Er^{167}$ (right) ($\nu$ = niu number of neutrons produced per fission)

The calculations show that void reactivity is more sensitive at higher fuel burnup. Fig.5.10 shows that concentrations of $Er^{167}$ and $U^{235}$ are much lower for burned

fuel in comparison to ones in the fresh fuel. However, changes in concentration of isotopes can not clearly indicate magnitude of influence on the properties of fuel lattice. Therefore, calculations of reaction rates due to $U^{235}$, $Pu^{239}$ and $Er^{167}$ isotopes were performed for all the three fuel-types. The results are presented in Fig.5.11.

The figure shows the number of neutrons generated by $U^{235}$ and $Pu^{239}$ isotopes per second and absorption rate of $Er^{167}$. It is seen that $Pu^{239}$ influences the fission rate at higher fuel burnup considerably and the influence is higher for fuel that has lower initial $U^{235}$enrichment. In addition, the absorption rate of erbium is less significant at higher fuel burnup.

The $Pu^{239}$ isotope has high absorption and fission cross-sections that have a wide resonance peak in the energy interval between 0.1 and 0.4eV, as shown in Fig.5.9. That means, the fission rate increases when neutron spectrum is shifted towards higher energies. In addition, this isotope releases more neutrons per fission in comparison with uranium.

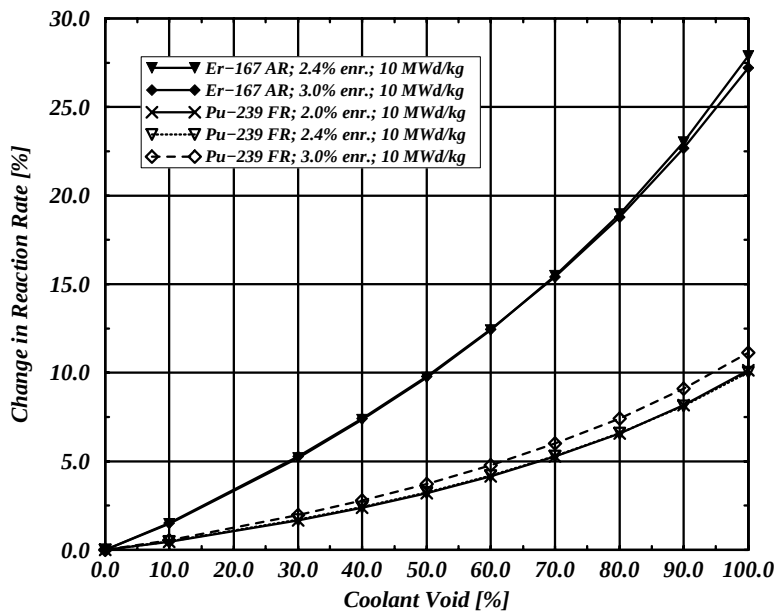


**Fig.5.12** ν·fission reaction rate sensitivity of $Pu^{239}$ (**FR**) and absorption reaction rate sensitivity of $Er^{167}$ (**AR**)

CASMO-4 results confirmed that the fission reaction rate of $Pu^{239}$ increases in the case of voiding. Fig.5.12 shows that $Pu^{239}$ fission rate increases by up to 10% at full coolant void for 10MWd/kg burnup. This effect becomes important at high fuel burnup, when concentration of plutonium increases. The same figure shows that the absorption rate of $Er^{167}$ increases up to 30% at 100% coolant void. However,

concentration of erbium is low at high fuel depletion and absorption rate may be increased only by other fission products that have similar properties as $Er^{167}$.

Several isotopes, namely, $Pu^{240}$ and $Np^{237}$ have absorption pecks similar to erbium. However, concentration of these isotopes is not sufficient to compete with an increase of fission rate induced by $Pu^{239}$. Consequently, ratio of integrals in Eq.5.9 increases faster with the voiding at higher burnup, and $\eta$ increases more rapidly as shown in Fig.5.8. It should be noted that this effect is less sensitive for fuel of higher enrichment and increased erbium concentration, since the $U^{235}$ is the isotope that defines the fuel lattice fission properties even at high burnup.

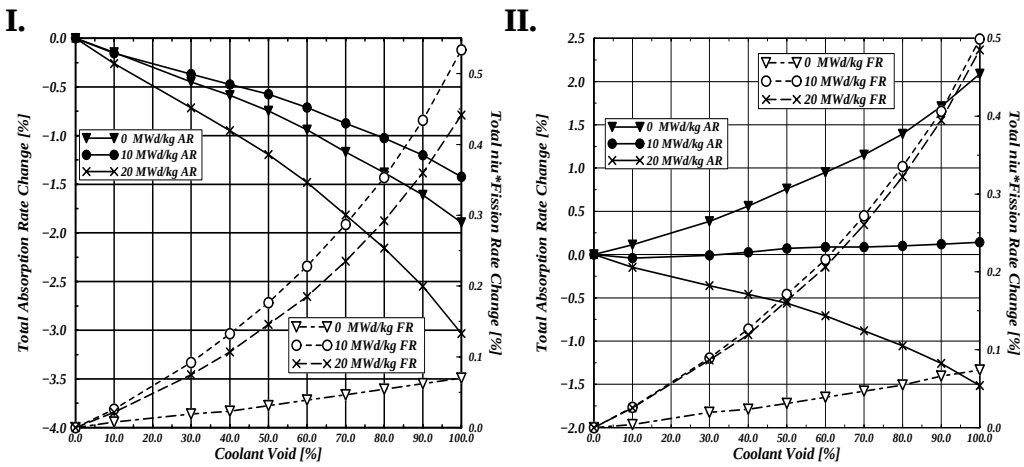


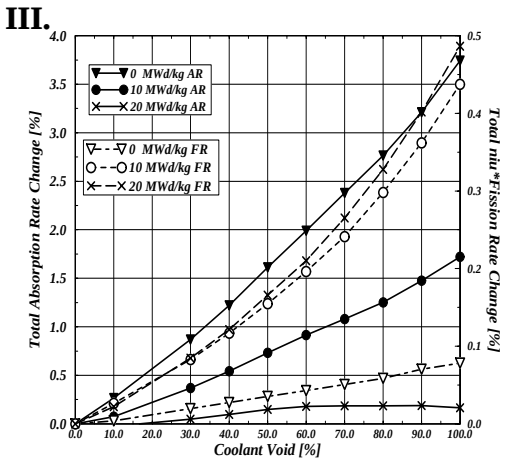


**Fig.5.13** ν·fission reaction rate and absorption reaction rate sensitivity versus coolant void. The right-hand axis indicates variation of fission reaction rate (**FR**) and the left-hand axis indicates values of absorption reaction rate changes (**AR**).

I. 2.0% enriched fuel,

II. 2.4% enriched fuel and uniformly mixed with 0.41 w/% $Er_2O_3$,

III. 3.0% enriched fuel and uniformly mixed with 0.80 w/% $Er_2O_3$.

Fig.5.13-I shows reaction rate sensitivities for the 2.0% enriched fuel. The figure indicates that absorption reaction rate versus void decreases for the fresh and for

the depleted fuel. In addition, absorption has lower gradient at 10 MWd/kg in comparison to the fresh fuel. This phenomenon is caused by generation of fission products, which increase absorption. Consequently, the void reactivity coefficient of the original fuel even decreases up to 7MWd/kg.

The plots of fission reaction rate changes indicate an increase at all fuel burnup points. A much large increase is observed for the depleted fuel. Explanation is that the concentration of plutonium is high at 10MWd/kg burnup and fission increase because of the fission resonance peak in the case of neutron flux hardening.

The Fig.5.13-II shows the reaction rate sensitivities for fuel 2.4% enriched with 0.41w/% erbium. The sensitivity of fission rate is similar to that of original fuel, i.e. a slight increase for fresh fuel and a rapid increase for the depleted fuel. The change of absorption rate versus void is different from that for fuel without erbium. The figure indicates that the absorption rate increases by up to 2% for fresh fuel at full voiding. It is almost independent of void at burnup of 10MWd/kg and decreases by up to –1.5% at 20MWd/kg depletion.

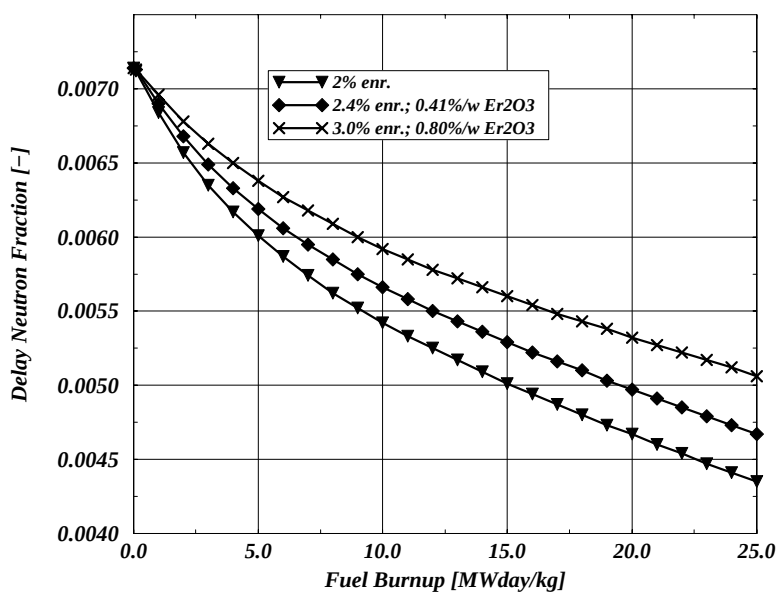


**Fig.5.14** Delayed neutron fraction $\beta$

The Fig.5.13-III shows reaction rate sensitivities for fuel 3.0% enriched with 0.80 w/% erbium. The concentration of erbium was increased by a factor of two and that caused higher sensitivity of absorption rate, which also increased by a factor of two in comparison to the 2.4% enriched fuel at zero burnup. The increase of absorption versus void was observed even for highly depleted fuel.

The fission reaction rate varies in a similar way as for other two fuel types; i.e. there is a slight positive increase for fresh fuel, and reaction rate sensitivity increases with higher burnup. Such conditions induce negative void reactivity coefficient for fresh fuel. This coefficient increases almost linearly versus burnup, as shown in Fig.5.5. This figure also indicates that the reactivity coefficient of fuel 2.4% enriched at 10MWd/kg is almost the same as the one of 3.0% enriched fuel at 20MWd/kg burnup.

Fuel that has higher initial enrichment has higher delayed neutron fraction versus fuel burnup in comparison with the fuel of less enrichment, as shown in Fig.5.14. The delayed neutron fraction ($\beta$) magnitude defines the reactor prompt criticality condition. In case reactivity is higher than $\beta$, reactor becomes prompt critical. In other words, the core would be critical on prompt neutrons, and control of chain reaction would not be possible.

Fig.5.14 indicates that fuel initially enriched to 2.0% of $U^{235}$, has a 36% smaller delay neutron fraction at 20MWd/kg burnup, whereas, 3% enriched fuel has $\beta$ that is only 25% less as initial.

### 5.1.5 **Conclusion**

One of the purposes of the fuel lattice analysis by the CASMO-4 code was to investigate the possible reactivity variation induced by coolant void, fuel and graphite temperature changes. The analysis showed that fuel temperature coefficient is negative for all fuel types, whereas, the void and graphite reactivity coefficients may be negative or positive depending on fuel type and burnup level.

The calculations indicate positive coolant void and graphite temperature reactivity coefficients in the case of 2% enriched fuel. It has to be noted that value of positive void reactivity coefficient increases considerably at higher fuel burnup.

The study of higher enriched fuel homogeneously mixed with erbium burnable poison indicates that void reactivity coefficient initially is negative and becomes positive at higher burnup. The same tendency is observed for graphite reactivity coefficient.

The second aim of this study is to point out the causes for an increase of the void reactivity coefficient. Therefore, the sensitivity analysis of the terms in the four-factor formula versus coolant void was performed. The sensitivity studies show that void reactivity is mainly defined by variation of thermal utilization $f$ and average number of neutron emitted per thermal neutron absorbed in fuel $\eta$. These two terms are most sensitive to the coolant void changes and are fuel-burnup

dependent. The sensitivity of these terms is reduced by increasing enrichment and mixing uranium with erbium burnable poison.

The decrease of coolant density induces two effects. First, absorption is reduced in fuel lattice, since water as absorber disappears. Second, neutron flux spectrum is hardened since water, as a moderator, is lost. The neutron spectrum is defined by graphite temperature and is shifted to higher energies. Because of these effects, the macroscopic absorption cross-sections decrease. Unfortunately, the absorption decrease in whole lattice is faster than in fuel and therefore the thermal utilization increases (see Eq.5.7). The sensitivity of $f$ is reduced by increasing fuel enrichment and adding erbium.

The shift of neutron flux spectrum to higher energy influences $\eta$ also. This term is strongly dependent on fuel type and burnup. In the case of 2% enriched fuel, this term increases considerably with coolant voiding. The decrease of $U^{235}$ and the increase of $Pu^{239}$ concentrations cause an increase in the sensitivity of $\eta$ at higher fuel burnup. Plutonium has a wide fission cross section resonance, which acts as a fission trap and an increase of fission rate occurs when neutron flux is hardened. The sensitivity of $\eta$ is decreased by using higher enrichment fuel mixed with erbium. This is caused by the fact that $Er^{167}$ isotope has a very high absorption cross section resonance in the energy interval between 0.2 and 0.8eV, which increases the fuel absorption during the voiding process.

## 5.2 Modeling of a Hypothetical Fuel Drop Event

### 5.2.1 Introduction

The RBMK reactors are designed to perform on-line refueling capability. The fuel assemblies are changed while the reactor is operating at full power. The refueling is performed every day, and knowledge of the consequences of a fresh fuel bundle, which being loaded by the fuel machine, dropping in the reactor, instead of being lowered in position is the subject of this study.

A hypothetical event of fuel assembly drop was assumed coupled with the assumption that the local Automatic Control System (ACS) does not operate, and a mechanical-hydraulic study in combination with reactor physics analysis was performed. The mechanical-hydraulic model was developed for the estimation of velocity of fuel bundle drop used for the neutron transient analysis. The reactor physics study was conducted by employing ARROTTA code and the data preprocessing system developed at the KTH.

### 5.2.2 Refueling Procedure

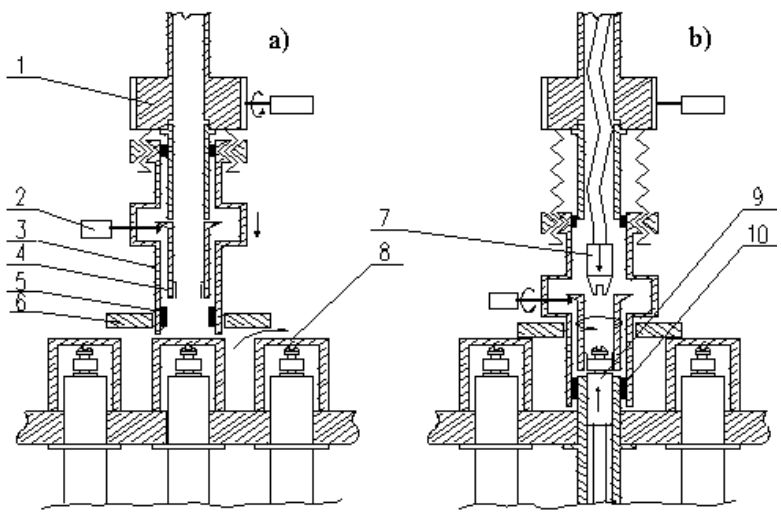


1 - standpipe control mechanism, 2 - special sealing key control mechanism, 3 - standpipe, 4 - special key, 5 - inflatable rubber sealing gaskets, 6 - bottom biological shield, 7 - grabber, 8 - enclosing clock, 9 - fuel channel seal plug, 10 - fuel channel body

**Fig. 5.15** Refueling machine operation a) refueling machine positioning over the fuel channel, b) unsealing of the fuel channel [1]

The fuel change procedure begins by adjusting local reactor conditions according to regulations. Thus, before the fuel refueling procedure starts, water flow is increased up to 45 $m^3$/sec in the fuel channel.

The axial positions of surrounding control rods are constantly changed during refueling by Automatic Control System (ACS). The ACS detectors located close to the refueled channel register neutron flux changes and control rods are relocated according to these signals.

A refueling procedure schematic is shown in Fig. 5.15. The operation starts by positioning the refueling machine on the top of fuel channel. That can be done by using closed-circuit television or by employing optical instruments.

After the refueling machine is positioned, sealing of the machine and the channel begins. The standpipe control mechanism (1) lowers the standpipe (3), which encloses the upper portion of the fuel channel (10) as indicated in the Fig. 5.15-b. The joint is sealed by rubber gasket (5), and the standpipe is filled with water of $30^0$C from the tank. Next, the closing mechanism dampers are opened, and the feedwater pump, included in the refueling machine, pressurizes the fuel casket. The pressure is increased until it matches the pressure in the fuel channel. Then, the grabber (7) is lowered and the sealing mechanism (2) unseals the channel. The seal plug (9) of the fuel channel is disengaged by a special key (4) and volumes of standpipe and fuel channel are joined.

Water is pumped from the machine into the fuel channel by feedwater pump, and cold water prevents steam and hot water from entering the refueling machine from the fuel channel.

The depleted fuel assembly is lifted 7.5 m into the cooling zone, where it is kept for about 10 minutes. Afterwards, the fuel assembly is pulled into the refueling machine. Next, the empty fuel channel is inspected by using a movable gauge, and a new fuel assembly is lowered. The resealing of fuel channel is performed after the sealing plug (9) reaches the nest. Then the refueling machine is disconnected and old fuel is transported to the fuel storage. More detailed description of refueling procedure is provided by reference [1].

### 5.2.3 Mechanical-Hydraulic Model of the Fuel Drop Event

A hypothetical event was studied, where a fresh fuel bundle disengages from the grabber and falls into the fuel channel. In addition, it was assumed that the automatic control system was disabled. Therefore, only the Doppler feedback controls the positive reactivity introduced by the rapid insertion of fresh fuel in the core.

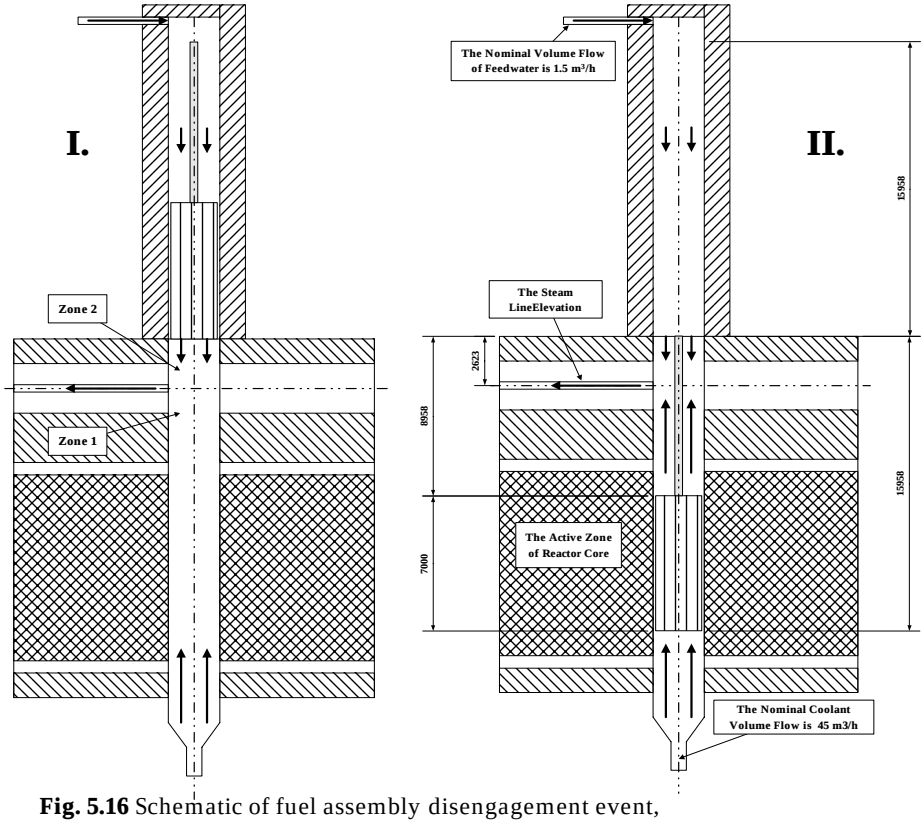


**Fig. 5.16** Schematic of fuel assembly disengagement event,
I. Initial position of fuel bundle
II. Final position of fuel cluster

The velocity of the travel of the fuel bundle into the fuel channel is required for the reactor physics calculations. Therefore, a mechanical-hydraulic model was developed to calculate the fuel-bundle velocity. The model is based on the balance of four forces, namely gravity, friction, local resistance and buoyancy. This balance ignores the friction between the fuel channel and the fuel cluster rods.

The above forces are not balanced at the beginning of the fuel drop and the fuel bundle is accelerated. The acceleration is determined by balance of four forces

$$F_A = F_G - F_B - F_{FR} - F_{LR} \qquad \textbf{Eq.5.10}$$

Here, $F_G$ is gravity force that drives the fuel assembly down. $F_B$ stands for buoyancy force. $F_{LR}$ is local resistance force, and $F_{FR}$ is friction between the water and the fuel assembly surface.

By the second law of Newton:

$$F_A = m \cdot \frac{dv}{dt} \approx m \cdot \frac{v_i - v_{i-1}}{t_i - t_{i-1}} \qquad \textbf{Eq.5.11}$$

Here, $m$ is the mass of fuel assembly and $dv/dt$ is the acceleration. The velocity of fuel assembly is calculated by solving the equations 5.11 and 5.10 with respect to $v_i$.

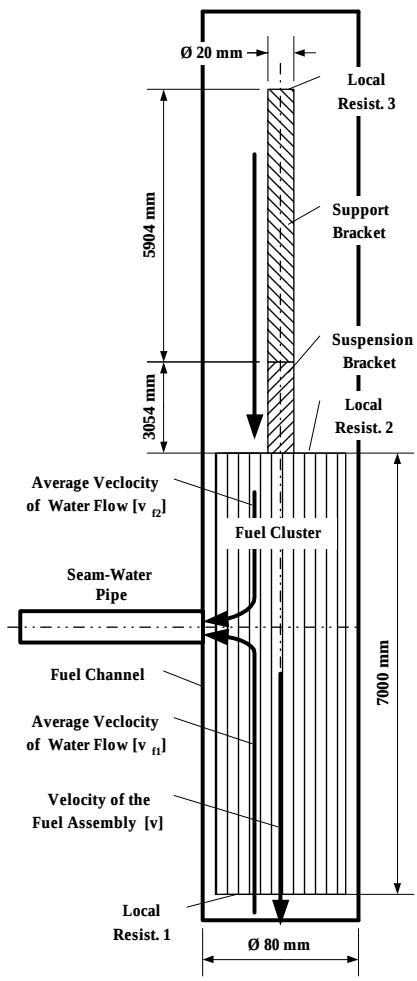


**Fig. 5.17** Fuel assembly model

The fuel bundle is driven down by the gravity force, which is 2744 N. The buoyancy force is dependent on coolant density and acts in the opposite direction. The local resistance and friction forces are opposite to the gravity as well. These depend on the geometry, velocity of the fuel bundle, and properties of water.

The fuel assembly includes fuel cluster, suspension bracket and fuel assembly support bracket shown in Fig. 5.17. The geometry of a fuel bundle is simplified and assumed to be a uniform cluster 7m long. Local resistance because of spacers is neglected. The cross section of the fuel cluster loaded in the fuel channel is shown in Fig. 4.2 and 5.2. The support and suspension brackets are modeled as 20mm diameter and 8.96m length cylinder. Internal diameters of fuel channel and fuel casket are assumed to be 80mm diameter.

The local resistance and friction forces also depend on location of fuel assembly in the channel. That is defined by two water flows shown in Fig.5.16-I and II. The first is 45m$^3$/h flow in the fuel channel. Water is fed into the lower part of the channel and removed through the

steam-water line. The coolant temperature is 263 $^0$C and pressure 70bar. The second stream of 1.5m$^3$/h volume flow is fed into the upper part of the refueling machine. The water is 30$^0$C temperature. This stream is removed throughout the steam-water line as well as the coolant from the fuel channel. The streams meet each other at the elevation of steam-water pipe and form a boundary where water flow direction is reversed. Therefore, the lower part of the fuel cluster passing the steam-water elevation is effected by water flowing up while the upper part is washed by the water streaming downwards.

The mechanical-hydraulic model was developed by considering both streams, and therefore the volumes of fuel channel and casket are simulated as two separate zones (see Fig. 5.16-I). The first zone is the space below the steam-water pipe elevation, and conditions are defined by coolant flowing upwards. The conditions of second zone are defined by feedwater flowing downwards. The mechanical-hydraulic model calculates position of fuel assembly at each time step and identifies parts of the assembly that are in different zones.

The buoyancy force is calculated by taking into account different coolant densities in the zones. The buoyancy force is recalculated, at each time step, when the assembly position is estimated with respect to the steam-water pipe elevation.

The total friction force is calculated as sum of friction forces, which are computed separately for each part of the fuel bundle. The calculations are performed by first identifying the position of the fuel bundle with respect to the steam-water pipe, since different zones have different conditions and geometrical configurations. The friction force of each fuel assembly part is

$$F_{FR} = C_{FR} \cdot \frac{\gamma \cdot \left| v - v_f \right| \cdot (v - v_f)}{2} \cdot S_{FR} \qquad \textbf{Eq.5.12}$$

here, $C_{FR}$ stands for the friction coefficient, $\gamma$ is the coolant density, and $S_{FR}$ is the surface area in contact with water. $v$ stands for velocity of fuel bundle and $v_f$ indicates velocity of fluid. The coolant density and friction surfaces for each part of fuel assembly are defined by considering location of each part with respect to the steam-water line.

The rough friction coefficient is calculated by employing empirical equations, used to estimate friction coefficient for water that flows in a cylindrical channel [10]. This rough friction coefficient is corrected by coefficients, which relate the flow in the cylindrical channel to the flow in the cluster and the annular geometry channels [10].

The local resistance force is calculated as a sum of three local resistance forces, which act on the lower and upper part of the cluster, and on the upper part of the

support bracket (see Fig.5.17). The simulation of local resistance force is performed employing Eq.5.13.

$$F_{LR} = C_{LR} \cdot \frac{\gamma \cdot \left| v - v_f \right| \cdot (v - v_f)}{2} \cdot S_{LR} \qquad \textbf{Eq.5.13}$$

here, $F_{LR}$ stands for the local resistance force, $C_{LR}$ is the local resistance coefficient, and $S_{LR}$ is cross sectional area of water flow. The other parameters are the same as in Eq.5.12. The coefficients of local resistance are calculated by employing standard empirical equations introduced in reference [10]. There are two types of equations. The first equation is used for the calculation of the local resistance coefficient when the cross-area of flow is sharply decreased as seen in Fig.5.17 for the lower part of the cluster. The second equation is used when the water flow cross-area sharply increases, as seen in the Fig.5.17 for the upper part of the cluster and the support bracket.

### 5.2.4 Results of Mechanical-Hydraulic and Reactor Physic Calculations

It was assumed that fuel disengages from the grabber when the lowest point of fuel assembly is at the top of fuel channel as shown in the Fig.5.16-I. The bundle falls while the sealing plug reaches its nest at the top of fuel channel. The final position of assembly is shown in the Fig.5.16-II.

The velocity of fuel assembly varies in time during this transient as shown in Fig.18-I. It increases from 0 m/sec up to 3 m/sec during 1sec, and decreases to 1.7 m/sec after 4.5 sec. The decrease of the velocity is caused by the fact that considerable surface of cluster is submerged in water flow opposite to the fuel drop.

The result shown in the Fig.5.18-I is also supported by Fig.5.19, which shows distribution of forces versus time. The Fig.5.19 indicates that acceleration force decreases rapidly because of increase of friction force. The acceleration force reaches zero at 1.1 sec, which corresponds to the maximum velocity. Later, the acceleration becomes negative because the fuel cluster reaches zone one, where water flows opposite direction to the fuel drop. Thus, the velocity decreases while acceleration force becomes zero. Then velocity stabilizes at 4.5 sec, since the entire cluster is submerged in the zone one at that moment. The Fig. 5.19 indicates that acceleration is zero as well after 4.5sec.

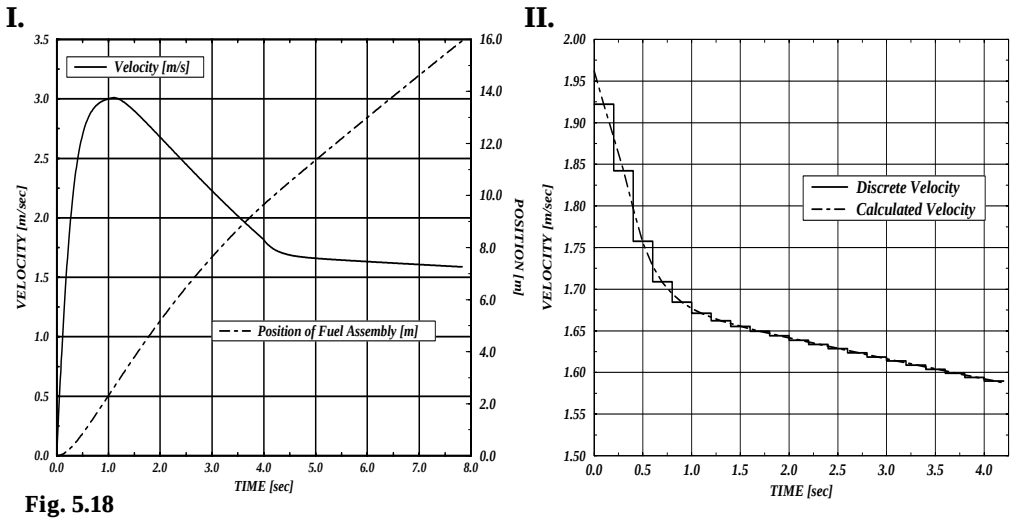


**Fig. 5.18**

I. Fuel bundle velocity (left hand scale) and position (right hand scale) versus time. The fuel cluster reaches active core in 3.63 sec and then the neutron transient starts.

II. Velocity of fuel assembly in the active core versus time. The time scale is made up referring to the beginning of neutron transient. Therefore, in this scale zero corresponds to 3.63 sec of actual assembly drop transient, i.e., 3.68 sec in the left-hand picture.

The neutron transient starts when the lowest point of fuel cluster reaches the top of the active core. That is going to happen after 3.63 sec, according to the results of mechanical-hydraulic model. Fig.5.18-I shows that the lowest point of cluster is located 8.95 m below the top of fuel channel after 3.63 sec, and the falling of the assembly continues up to 7.83sec. Thus, the fuel assembly is fully inserted in the active core in 4.2 sec.

The velocity of fuel assembly in the active core is shown in Fig.5.18-II. The time scale corresponds to zero when assembly reaches the top of the active core. The velocity is defined as a discrete function in the ARROTTA code input; therefore, a continuous velocity function was converted into the discrete values. The conversion was performed calculating average velocity in each 0.2sec interval as shown in Fig.5.18-II.

The neutron transient analysis was performed by employing the ARROTTA code and the data processing system developed at the KTH. The study of the fuel drop event was done by employing the core configuration and burnup database recorded at the first reactor unit of INPP on March 5, 1994. The reactor was operated at 4060 MWth and average burnup of fuel was 7.48 MWd/kg at the time this database was recorded. It was assumed that the hypothetical fuel drop event takes place during refueling of the central channel in the core marked as channel

23/25 in the database. In addition, it was assumed that control rods do not move during this event.

The fresh fuel assembly was introduced in an initially critical core with discrete velocity steps, which are shown in the Fig.5.18-II. The results calculated by the ARROTTA are presented in Fig.5.20-I and II. Fig.5.20-I shows reactivity changes starting with the time when the lowest point of the fuel cluster reaches the top of the active core. The reactivity curve reaches maximum value of 0.35$ between 2.5 and 4.0 sec and later decreases down to the zero in 250 sec.

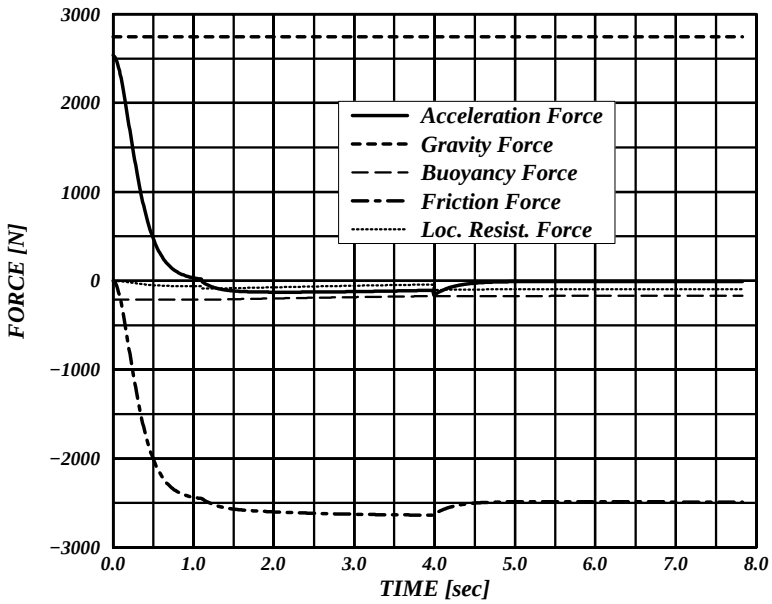


**Fig. 5.19** Forces that effect the fuel assembly

The increase of reactivity is initiated by insertion of fuel, while the decrease is caused by the Doppler feedback. The Doppler feedback becomes considerable with increase of core power. The variation of core power is shown in Fig.5.20-II. The power increases rapidly from 4060 MWth up to 4170 in five seconds and later increases slowly up to 4200 MWth in 100sec. The power increase causes higher fuel temperature and higher coolant void. Fortunately, the negative reactivity induced by the increase of fuel temperature is larger than the positive reactivity induced by coolant voiding. Thus, reactivity increase caused by fuel drop is compensated by the Doppler reactivity feedback.

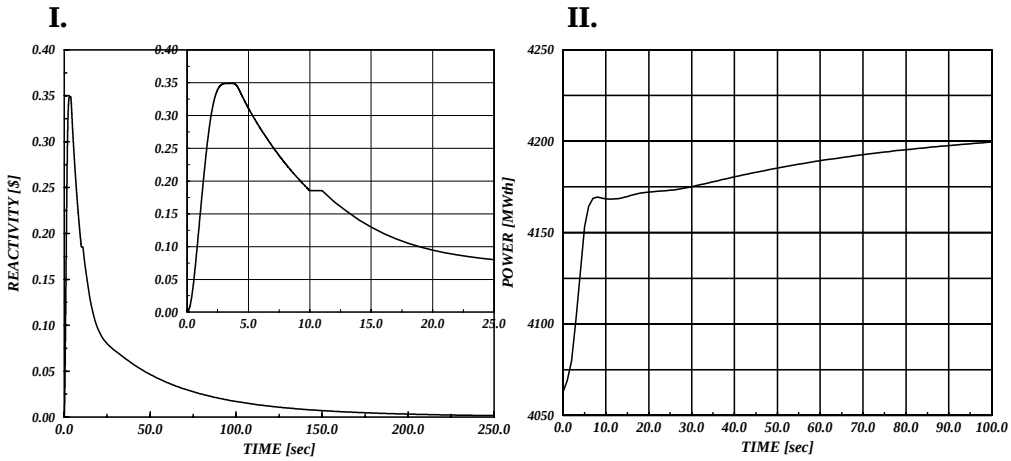


**Fig. 5.20**

I. Reactivity induced by the drop of the fuel bundle without the action of the automatic control system. The inset figure shows reactivity variation in first 25sec

II. Power variation during the hypothetical fuel drop event

## 5.2.5 **Conclusions**

A mechanical-hydraulic model was developed to calculate realistic conditions of fuel drop event; however, some simplifying assumptions are made. First, the geometry of fuel assembly was assumed to be cluster without spacers. Second, the uniform pressure of 70bar was considered in the whole channel. Third, the friction, which may occurs between the fuel channel and the fuel cluster, is neglected. We believe that the drop velocity of fuel assembly would be slightly lower if all real conditions would be considered. Thus, the results presented are conservative.

The mechanical-hydraulic study of the fuel drop event indicates that the fuel cluster would reach the top of the active core in 3.63 sec at which the velocity would be 1.95 m/sec. The fuel bundle reaches the bottom of the core in 7.83 sec at the velocity of 1.57 m/sec.

The reactor physics analysis of this event, by assuming that control rods do not move, indicates that the reactivity increases by 0.3$ and the increase in power is about 3.5%. The reactivity decreases down to zero and power increase is stabilized in approximately 250sec due to the Doppler feedback.

The calculated results indicate that fuel temperature increases to 882K much lower than the maximum allowed temperature of 2373K. Therefore, the fresh fuel drop event without local control action would not cause any fuel damage.

# 6 Summary and Conclusions

The reactor physics capabilities developed and adapted for the INPP reactor core analysis at the Division of Nuclear Power Safety are based on ARROTTA and CASMO-4 codes. The modifications and adaptations of the ARROTTA code included a) developing and modifying processing codes for the construction of the ARROTTA cross section library from CASMO-4 and WIMS-$D_4$ code calculations b) developing processing codes, which would access the Ignalina plant database and convert that to the input file required for the ARROTTA code and c) modifying the ARROTTA code to represent the different control rods in an RBMK plant. In addition, two codes were developed for automatic comparison of ARROTTA results with the measurements made in the plant.

The cross section library for ARROTTA is constructed by employing results calculated by the CASMO-4 (for fuel assemblies) and the WIMS-$D_4$ (for non-fuel assemblies) lattice codes. Future studies will include cross section library generation by employing HELIOS code that is capable of treating all types of assemblies. We believe that HELIOS results may improve ARROTTA results, since all cross sections will be generated by one code and assembly discontinuity factors (ADF) will be available.

The ARROTTA code was validated against data obtained in RBMK-type critical facility experiments. Comparisons were made for the effective multiplication factor, neutron flux distribution and control rod worth. Several critical experiments were analyzed and it was found that the ARROTTA results were in excellent agreement with the measurements as Table 4.16 indicates. The average neutron flux discrepancy at initial core conditions is only 1.0-6.0% and it increases to 11% during the control rod transients. Table 4.16 also indicates that effective multiplication factors calculated by ARROTTA for critical experiments are very close to unity.

In the critical facility experiments, the control rod worth was measured by the reactimeter by summarizing the amplitudes of the signals from several detectors. The sum signal was converted to reactivity by employing Inverse Point Kinetics. For comparison wit measurements, the REAC code was developed to exactly simulate the experimental procedure of reactivity estimation but using the ARROTTA code results as input signals. The comparison of calculated and measured control rod worth was also in excellent agreement as seen in Table 4.16.

The reactor physics capabilities available and developed at the NPS were applied for the INPP analyses. The CASMO-4, two-dimensional lattice code was applied for RBMK fuel studies. It was found that higher fuel enrichment and higher erbium concentration imparts favorable safety characteristics, namely, negative

coolant void and moderator (graphite) temperature reactivity coefficients at low fuel burnup (up to 7MWd/kg).

In order to understand void reactivity behavior, a sensitivity analysis of the terms in the four-factor formula with respect to coolant void was performed. The sensitivity studies showed that void reactivity is mainly defined by the thermal utilization $f$ and the average number of neutrons emitted per thermal neutron absorbed in fuel $\eta$. These two terms of the four-factor formula were effected the most by the coolant void changes and they are also fuel burnup dependent. The sensitivity of these terms is reduced by increasing enrichment and mixing uranium with Erbium burnable poison.

The other application that was considered in this thesis was the study of a hypothetical fuel drop event in the INPP during refueling. For this analysis a mechanical-hydraulic model was developed for the fuel assembly drop velocity computation. The ARROTTA code, with the data preprocessing system developed at the NPS, was employed for the neutronics calculations. The calculations were performed using real core configuration data registered in the database. It was assumed that a fuel assembly drops in the core during refueling and the CPS was inactive.

The mechanical-hydraulic study of the fuel drop event indicates that the fuel cluster would reach the top of the active core in 3.63 sec and velocity would be 1.95 m/sec. The fuel bundle reaches the bottom of the core in 7.83 sec with 1.57 m/sec velocity.

The reactor physics analysis of this event, while assuming that control rods do not move, indicates that the reactivity may increase by 0.3$ leading to an increase in power of approximately 3.5%. The reactivity decreases down to the zero and power increase is stabilized in approximately 250sec due to the Doppler effect. The calculated results indicate that fuel temperature increases to 882K while maximum permitted is 2373K. Therefore, the fuel drop event would not cause any fuel damage.

We believe that the RBMK neutron dynamics (with thermal-hydraulic feedback) analysis capability developed at KTH/NPS will predict accurate core conditions and consequences of actual and/or postulated system upsets that are generally considered for assessment of the safety of a nuclear power plant such as Ignalina Nuclear Power Plant.

# 7 Nomenclature

## 7.1 Abbreviations

| | |
|---|---|
| AA | Additional Absorber |
| ACS | Automatic Control System |
| ADF | Assembly Discontinuity Factor |
| ANM | Analytical Nodalization Method |
| ARROTTA | Advanced Rapid Reactor Operation Transient Analysis |
| BCSL | Basic Cross Section Library |
| BWR | Boiling Water Reactor |
| CF | Critical Facility |
| CPS | Control Protection System |
| CRD | Control Rod |
| CRI | Control Rod Imitators |
| DB | INPP Database |
| DBC | Database Converter |
| ECF | Experiments using Copper Foils |
| EFC | Experiments using Fission Chambers |
| ENDF/B | Evaluated Nuclear Data Files /B |
| FASR | Fast Acting Scram Rod |
| ICS | Information Computing System |
| INPP | Ignalina Nuclear Power Plant |
| KI | Kurchatov Institute |
| KTH | Royal Institute of Technology |
| LWR | Light Water Reactor |
| MCC | Main Circulation Circuit |
| MCP | Main Circulation Pumps |
| MCR | Manual Control Rod |
| NPS | Nuclear Power Safety |
| PDMS-A | Axial Power Density Monitoring System |
| PDMS-R | Radial Power Density Monitoring System |
| PI | Position Indicator |
| PWR | Pressurized Water Reactor |
| RBMK | Channeled Large Power Reactor (Russian acronym) |
| SCR | Shorted Control Rod |
| SIP | Swedish International Project |

## 7.2 Arabic

| | | |
|---|---|---|
| $\Delta h$ | Interpolated length | m |
| $A, B, C$ | Quadratic coefficients | - |
| $A_a$ | Relative activity of the copper foil | barn/(cm$^2$·sec) |

| | | |
|---|---|---|
| $B(z)$ | Axial fuel burnup rate | MWd / m |
| $C_d(\mathbf{r}, t)$ | Delay neutron precursors for delay neutron group d | $cm^{-3}$ |
| $C_{FR}$ | Friction coefficient | - |
| $C_{LR}$ | Local resistance coefficient | - |
| $E$ | Energy | eV |
| $E_T$ | Thermal energy (4eV) | eV |
| $f$ | Thermal utilization | - |
| $F$ | Function of poison isotopes | - |
| $\mathbf{F}_A$ | Acceleration force | N |
| $\mathbf{F}_B$ | Buoyancy force | N |
| $\mathbf{F}_{FR}$ | Friction force | N |
| $\mathbf{F}_G$ | Gravity force | N |
| $\mathbf{F}_{LR}$ | Local resistance force | N |
| $H$ | Core height | m |
| $k_{eff}$ | Effective multiplication factor | - |
| $k_{inf}$ | Infinite multiplication factor | - |
| $L$ | Prompt neutron life time | sec |
| $m$ | Fuel assembly mass | kg |
| $N$ | Concentration | $cm^{-3}$ |
| $N_i$ | Fitting coefficients | - |
| $NI_1$ | Number of isotopes in fuel region | - |
| $NI_2$ | Number of isotopes in non-fuel region | - |
| $p$ | Resonance escape probability | - |
| $\mathbf{r}$ | Three dimensional position vector | $cm^3$ |
| $R$ | Monotonically increasing function of the nodal control fraction | - |
| $S_{FR}$ | Friction surface | $m^2$ |
| $S_{LR}$ | Cross-area of water flow | $m^2$ |
| $t$ | Time | |
| $T(t)$ | Time dependent detector signal | - |
| $T_0$ | Initial detector signal | - |
| $T_F$. | Fuel temperature | F |
| $T_M$ | Moderator temperature | F |
| $V_1$ | Fuel volume | $cm^3$ |
| $V_2$ | 7.2.1.1.1.1 Non- fuel volume | $cm^3$ |
| $\mathbf{v}$ | Fuel bundle velocity | m / sec |
| $v_g$ | Average group g neutron speed | m / sec |
| $x$ | Variable | - |
| $z$ | Axial core coordinate | m |

## 7.3 Greek

| | | |
|---|---|---|
| $\Delta$ | Finite difference | - |
| $\rho$ | Reactivity | -;$; |
| $\gamma$ | Coolant density | $g / cm^3$ |

| | | |
|---|---|---|
| $\alpha$ | Reactivity coefficient | -; 1/K |
| $\eta$ | Average number of neutron emitted per thermal neutron absorbed in fuel | - |
| $\varepsilon$ | Fast fission factor | - |
| $\sigma$ | Microscopic cross section | barn |
| $\delta$ | Small difference | - |
| $\Phi(\mathbf{r}, E)$ | Energy and position dependent neutron flux | $1/(cm^2 \cdot sec)$ |
| $\Phi_g(\mathbf{r}, t)$ | Time-space dependent, g energy group neutron flux | $1/(cm^2 \cdot sec)$ |
| $\mathbf{J}_g(\mathbf{r}, t)$ | Time-space dependent, g energy group current | $1/(cm^2 \cdot sec)$ |
| $\Sigma_{tg}(\mathbf{r}, t)$ | Total macroscopic absorption cross section plus removal cross section in group g | $cm^{-1}$ |
| $\Sigma_{fg}(\mathbf{r}, t)$ | Fission macroscopic cross section in group g | $cm^{-1}$ |
| $\Sigma_R(\mathbf{r}, t)$ | Macroscopic scattering removal cross section for group 1 to 2 transfer | $cm^{-1}$ |
| $\nu_g$ | Mean number of neutrons emitted per fission in group g | - |
| $\lambda_d$, | Decay constant for precursor in group d | $sec^{-1}$ |
| $\bar{\beta}_d(\mathbf{r})$ | Effective fraction of fission neutrons emitted from delay precursor group d | - |
| $\sigma_{ag}$ | Microscopic absorption cross sections in group g | barn |
| $\Phi_D(t)$ | Neutron flux calculated at the location of detector | $1/(cm^2 \cdot sec)$ |
| $\bar{\Phi}_C(t)$ | Average core neutron flux calculated at steady state | $1/(cm^2 \cdot sec)$ |
| $\beta$ | Delay neutron fraction | - |
| $\Sigma_{a0,i}$ | Macroscopic absorption cross section of isotope i in fuel region | $cm^{-1}$ |
| $\Sigma_{a1,i}$ | Macroscopic absorption cross section of isotope i in non-fuel region | $cm^{-1}$ |
| $\Sigma_{f,,i}$ | Macroscopic fission cross section of isotope i in the fuel region | $cm^{-1}$ |
| $\nu_{f,i}$ | The average number of neutrons released per fission for isotope i | - |

## 7.4 Subscripts

| | |
|---|---|
| *1* | Fuel region; Fast energy group |
| *2* | Non-fuel region; Thermal energy group |
| *a* | Absorption |
| *A* | Acceleration |
| *B* | Buoyancy |
| *d* | Delay neutron group |
| *eff* | Effective |
| *f* | Fission |
| *F* | Fuel |
| *FR* | Friction |

| | |
|---|---|
| *FT* | Fuel temperature |
| *g* | Energy group |
| *G* | Gravity |
| *i* | Nuclide index; Delay neutron group; Index of interpolation coef. |
| *inf* | Infinite |
| *LR* | Local resistance |
| *M* | Moderator |

# 8 References


1. **Almenas, K., Kaliatka, A., Ušpuras, E.:** *"Ignalina RBMK-1500 a Source Book"*. Ignalina Safety Analysis Group, Lithuania Energy Institute, Lithuania, 1998.

2. **Batia, G. A.:** *" The Fundamental Theories and Methods of Nuclear Power Reactor Calculations"*. Moscow, Energoizdat, 1982.

3. **Borland, R. S., Cobb, W. R., Darnell, B. L., Rothleder, B. M., Singer, B. S.**: " *ARMP-02 Documentation Part 2, Chapter 13 – NORGEP-P Computer Code Manual Volume 1: Theory and Numerics Manual"*. NP-4574-CCM, Part 2, Chapter 13, Volume 1, Researcher Project 976-3, 1987.

4. **Cobb, W. R., Borland, R. S., Darnell, B. L., Versteegen, P. L.**: " *ARMP-02 Documentation Part 2, Chapter 8 – SIMULATE-E (mod.3) Computer Code Manual"*. NP-4574-CCM, Part 2, Chapter 8, Researcher Project 976-3, 710-1, 1987.

5. **Edenius, M., Ekberg, K., Forssen, B.H., Knott, D.:** *"CASMO-4 a Fuel Assembly Burnup Program. User's Manual"*. Studsvik of America, Inc., Stidsvik Core Analysis AB, 1993.

6. **Eisenhart, L.D.:** "*ARROTTA-01 – An Advanced Rapid Reactor Operation Transient Analysis Computer Code. Volume 1: Theory and Numerics"*. NP-7375, Volume 1 Research Project 1936-6, 1991.

7. **Eisenhart, L.D.:** "*ARROTTA-01 – An Advanced Rapid Reactor Operation Transient Analysis Computer Code. Volume 2: User's Manual"*. NP-7375-CCML, Volume 2 Research Project 1936-6, 1991.

8. **Eisenhart, L.D.:** "*ARROTTA-01 – An Advanced Rapid Reactor Operation Transient Analysis Computer Code. Volume 3: Programmer's Manual"*. NP-7375-CCML, Volume 3 Research Project 1936-6, 1991.

9. **Glasstone, S., Edlund, M. C.***: "The Elements of Nuclear Reactor Theory"*. D. Van Nostrand Company, 1952.

10. **Kirilov, P. L., Jurev, J. S., Bobkov V. P.:** *Handbook of Thermal-Hydraulic Calculations (Nuclear Reactors, Heat Exchanges, Steam Generators)"*. Moscow, Energoizdat, 1984.

11. **Knott, D., Forssen, B.H., Edenius, M.:***"CASMO-4 a Fuel Assembly Burnup Program Methodology"*. Studsvik of America, Inc., Studsvik Core Analysis AB, 1993.

12. **Lamarsh, J. R.**: *"Introduction to Nuclear Engineering 2nd Edition"*. Addison-Wesley Publishing Company, 1983.

13. **Woolley, J. A., Anderson, M. J. Eisenhart, L. D., Rapp, V. B.**: *"REBLEND a Computer Program to Produce ARROTTA Input Using Results From NTPREP and NODE-P2 or SIMULATE-E. Input Description"*. Research Project 1761-1, Task 4, 1986.

14. **Woolley, J. A., Anderson, M. J.**: *" A computer program to produce a Nuclear Data Base for NODETRAN or REBLEND using results from CELL-2, NORGE-P, or NORGE-B2. Input Description and Programmer's Guide"*. Research Project 1761-1, Task 4, 1986.

15. **Balygin, A. A., Sehgal, B. R,**: *"A Comparison of the Effect of Different Cross Sections Libraries on the RBMK Fuel Cell Characteristics"*. Internal rapport: Div. of Nuclear Power Safety, Royal Institute of Technology.

16. **Panushkin, A. K., Krajushkin, A. V., Phedosov, A. M., Nicolaev, A. M., Kupalov-Yaropolk, A. I.**: *"Adding erbium to increase RBMK safety"*. Nuclear Engineering International, November 1995.

17. **Krayushkin, A.V., Afanasieva, A.A., Babytsev, M.N., Davydova, G.B., Glembotsky, A.V., Fedosov, A.M., Tsareva, S.M.**: *"Code Assessment for RBMK Reactor Applications. Assessment of the STEPAN Computer Code for RBMK Neutronic Modeling. Stage 2: The development of the documentation on STEPAN code and on verification and validation existed. The Full-Scale Neutronic Code STEPAN"*, Moscow, 1998

18. **Krayushkin, A. V., Davydova, G. B., Tishkin, Yu. A., Glembotsky, A. V., Tsareva, S.M., Zaharova L. N.**: *"Code Assessment for RBMK Reactor Applications. Assessment of the STEPAN Computer Code for RBMK Neutronic Modeling, Stage 3: The development of the benchmark documentation. Documentation On Benchmarks For 3-D RBMK Neutron Kinetics Validation."*, Moscow, 1998

19. **Davydova, G. B., Kachanov, V. M.**: *"The Experiments on the Critical Assembly of RBMK. Initial Data for Computer Modeling"*, Moscow, 1995